MARINE GEOLOGICAL INSTITUTE

GEOLOGICAL AGENCY
MINISTRY OF ENERGY AND MINERAL RESOURCES
Jalan Dr, Junjunan No. 236, Bandung-40174, Indonesia
http://www.mgi.esdm.go.id, E-mail: ejournal.p3gl@gmail.com

ISSN 1410 - 6175

BULLETIN OF THE MARINE GEOLOGY VOLUME 40, NUMBER 1, JUNE 2025 - ISSN 1410-6175

ISSN 1410-1675

BULLETIN OF THE MARINE GEOLOGY

VOLUME 40 • NUMBER 1 • JUNE 2025

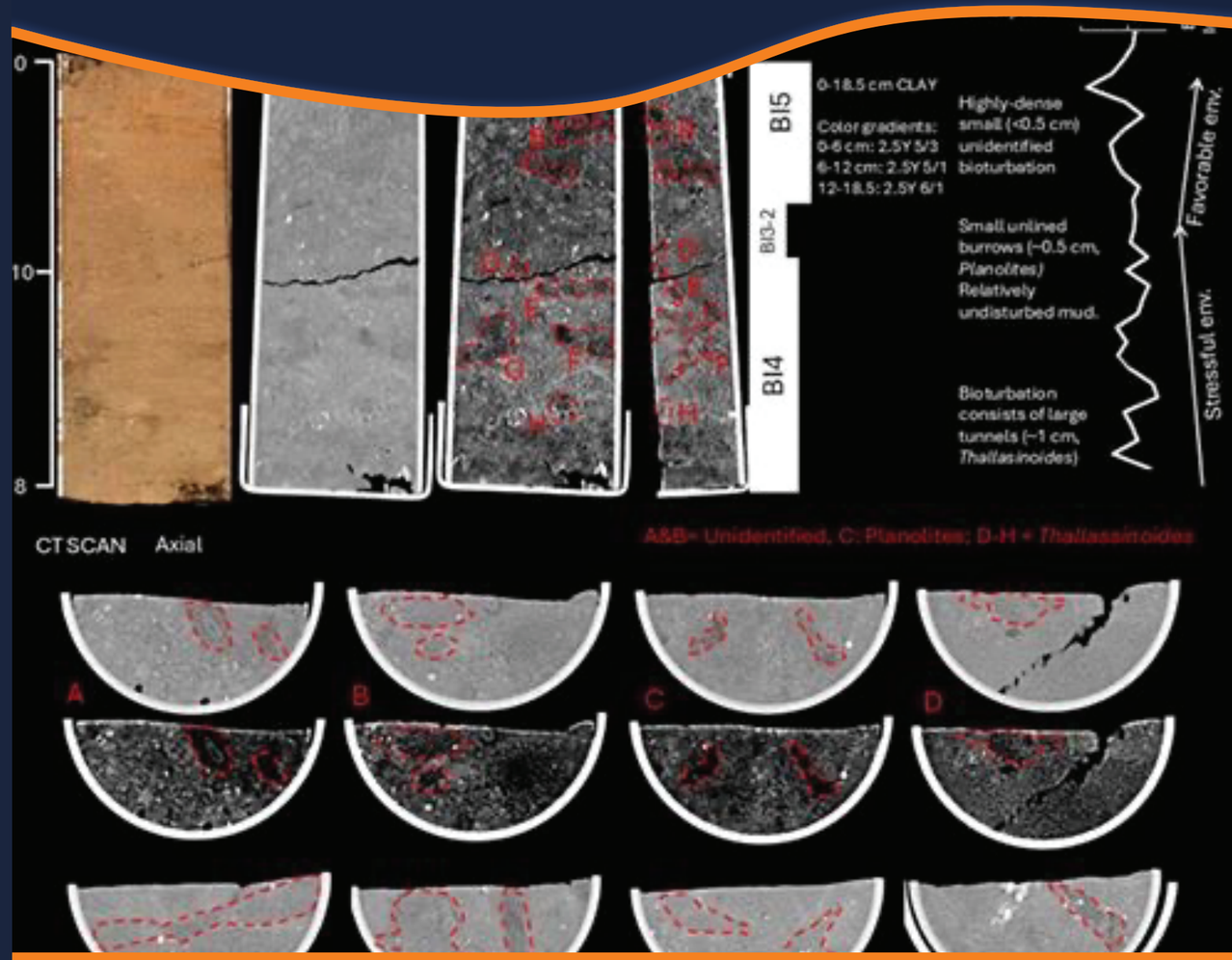

BoMG	VOL. 40	NO. 1	P. 1-75	BANDUNG, JUNE 2025	ISSN 1410-6175

Accredited : RISTEK-BRIN 200/M/KPT/2020

MARINE GEOLOGICAL INSTITUTE
GEOLOGICAL AGENCY
MINISTRY OF ENERGY AND MINERAL RESOURCES

BALAI BESAR SURVEI DAN PEMETAAN GEOLOGI KELAUTAN
BADAN GEOLOGI
KEMENTERIAN ENERGI DAN SUMBER DAYA MINERAL

BULLETIN OF THE MARINE GEOLOGY

Vol. 40, No. 1, JUNE 2025

For communication of this publications, please contact :

MARINE GEOLOGICAL INSTITUTE

Dr. Junjunan 236, Bandung-40174, Indonesia

Telephone : +62-22-6032020, 6032201, Fax : +62-22- 6017887

E-mail : ejournal.p3gl@gmail.com

Cover Figure : Core photo, CT scan, characteristics of sediments, ichnogenus, bioturbation density, and environment interpretation of BUDEE22-57BC. A-H indicates an axial CT scan showing each slice's lateral section. (Source: Wiguna, et al, 2025)

Preface

The first edition of the Bulletin of the Marine Geology (BOMG), published in June 2025, includes five scientific articles. This publication is part of an ongoing effort to disseminate scientific research in marine geology, encompassing oceanography, sediment dynamics, environmental geology, and geotechnical studies within Indonesian waters and surrounding regions.

The first article, study of heavy metal lead (Pb) content in the northern waters of Belitung Regency, examines the distribution of Pb concentrations in sediments and the water column, as well as the influence of seasonal variations (ocean currents) on their spatial distribution.

The second article in this edition discusses the variability of significant wave height, wind speed, and precipitation, and their impact on shipping safety along the Indonesian Archipelagic Sea Lanes (ALKI). The study aims to understand the risks by analyzing patterns of waves, wind, and rainfall in the ALKI, in order to enhance shipping safety and reduce maritime accidents.

The next article presents a study of thermocline temperature gradients along the Indonesian Throughflow (ITF) pathway during the Last Glacial Maximum (LGM). It examines ITF strength during the LGM in comparison to the Pre-Industrial (PI) period across the Makassar Strait, Maluku Sea, and Banda Sea as key segments of the ITF route. Seasonal temperature variations in the thermocline layer at these locations indicate that the ITF was significantly weakened during both the LGM and PI periods.

The fourth paper examine the impact of upwelling on environmental changes and sedimentation dynamics based on trace fossils in the Maluku Sea. This study analyzes bioturbation patterns and Zr/Rb ratios in sediment cores from the Maluku Sea to reconstruct past environmental conditions and assess the suitability of the sediments for age determination.

The last paper presents a study on bearing capacity and settlement behavior of coastal soils for the proposed development of Balongan Port, West Java. It reviews the bearing capacity and predicts settlement behavior through the integration of field and laboratory test data.

It is expected that the articles published in the first edition of 2025 will make a meaningful contribution to the advancement of science and technology, and serve as a valuable reference for policy development in sustainable coastal and marine management.

We sincerely thank the authors for their valuable contributions through the submission of scientific articles, and the peer reviewers for dedicating their time and expertise to providing critical and constructive feedback. Our appreciation also goes to the editorial team and all individuals and institutions who have supported the successful publication of this journal.

Finally, we invite readers to share feedback, comments, and suggestions for improving the quality of the Bulletin of the Marine Geology in the future.

Bandung, June, 2025

Chief Editor

ISSN 1410-6175

BULLETIN OF THE MARINE GEOLOGY

Vol. 40, No. 1, June 2025

Contents

UPWELLING INFLUENCE ON ENVIRONMENTAL CHANGE AND SEDIMENTATION DYNAMICS FROM TRACE FOSSILS IN THE MOLUCCA SEA: IMPLICATIONS FOR SEDIMENT DATING

PENGARUH UPWELLING TERHADAP PERUBAHAN LINGKUNGAN DAN DINAMIKA SEDIMENTASI BERDASARKAN FOSIL JEJAK DI LAUT MALUKU: IMPLIKASI UNTUK PENENTUAN UMUR SEDIMEN

Taufan Wiguna[1*], Rina Zuraida[1], Agus S. Atmadipoera[2], Fareza S. Yuwono[1], Undang Hernawan[3], Vera Christanti[1], Nicolas Tournier[4], Adrianus Damanik[4], Hendrik Vogel[4], Sri Yudawati Cahyarini[1]

[1]Research Center for Climate and Atmosphere, National Research and Innovation Agency, Bandung 40135, Indonesia
[2]Department Marine Science, FPIK, IPB University, Bogor 16680, Indonesia
[3]Research Center for Oceanography, National Research and Innovation Agency, Ancol, Jakarta 14430, Indonesia
[4]Institute of Geological Sciences & Oeschger Centre for Climate Change Research, University of Bern, Bern 3012, Switzerland

*Corresponding author: taufan.wiguna@brin.go.id

(Received 13 August 2024; in revised from 21 August 2024; accepted 28 March 2025)

DOI : 10.32693/bomg.40.1.2025.896

ABSTRACT: Bioturbation, the alteration of sediment layers by organism activities, plays a crucial role in shaping sedimentary environments. This process affects nutrient cycling, sediment stability, and habitat health, particularly in marine ecosystems like the Molucca Sea. Bioturbation can complicate age determination by disrupting the natural layering of sediments and potentially altering chronological records, which challenges the accuracy of dating methods. This study investigates bioturbation patterns and Zr/Rb ratios in sediment cores from the Molucca Sea to better understand past environmental conditions and assess the suitability of these sediments for age determination. Sediment samples were collected using a box corer from BUDEE22-29BC (within the upwelling region) and BUDEE22-57BC (outside the upwelling area). The cores were analyzed using CT scanning to identify bioturbation features, and the Bioturbation Index (BI) was applied to evaluate the intensity and impact of bioturbation on sediment dynamics. The Zr/Rb ratios were determined using an X-ray fluorescence (XRF) spectrometer, providing insights into grain size distribution. The results suggest the potential shifting of the upwelling center (BUDEE22-29BC) and variations in upwelling intensity (BUDEE22-57BC). Although Zr/Rb ratio shows that BUDEE22-29BC is a high-energy environment, as opposed to BUDEE22-57BC, both sites retain chronological integrity, making them suitable for paleoenvironmental and geochronological analysis.

Keywords: bioturbation, CT scan, paleoenvironment, Banggai, upwelling, BUDEE22

ABSTRAK: *Bioturbasi, perubahan lapisan sedimen akibat aktivitas organisme, memainkan peran krusial dalam membentuk lingkungan sedimen. Proses ini memengaruhi siklus nutrisi, stabilitas sedimen, dan kesehatan habitat, terutama di ekosistem laut seperti Laut Maluku. Bioturbasi dapat mengganggu pelapisan alami sedimen dan berpotensi mengubah catatan kronologis, yang menjadi tantangan dalam akurasi metode penentuan umur. Penelitian ini menyelidiki pola bioturbasi dan rasio Zr/Rb dalam inti sedimen dari Laut Maluku untuk memahami kondisi lingkungan masa lampau dan menilai kelayakan sedimen tersebut untuk penentuan umur sampel. Sampel sedimen diambil dari Laut Maluku menggunakan box corer, dengan sedimen inti diambil dari dua lokasi: BUDEE22-29BC (di pusat upwelling) dan*

BUDEE22-57BC (di luar area upwelling). Inti sedimen dianalisis menggunakan CT scan untuk mengidentifikasi fitur bioturbasi, dan indeks bioturbasi (BI) diterapkan untuk mengevaluasi intensitas dan dampak bioturbasi terhadap dinamika sedimen. Rasio Zr/Rb ditentukan menggunakan X-ray fluorescence (XRF) spectrometer, memberikan wawasan tentang distribusi ukuran butir. Hasil penelitian menunjukkan adanya potensi pergeseran pusat upwelling (BUDEE22-29BC) serta variasi intensitas upwelling (BUDEE22-57BC). Meskipun rasio Zr/Rb menunjukkan bahwa BUDEE22-29BC diendapkan di lingkungan berenergi tinggi, bertolak belakang dengan BUDEE22-57BC, kedua sampel menunjukkan bahwa perlapisan masih tidak terganggu sehingga dapat digunakan untuk analisis lingkungan masa lampau dan geokronologi.

Kata Kunci: *bioturbasi, CT scan, lingkungan purba, Banggai, upwelling, BUDEE22*

INTRODUCTION

Bioturbation refers to the alteration of sediment layers caused by the activities of organisms, including burrowing, tunneling, and movement. This process plays a critical role in marine ecosystems by influencing nutrient cycling, sediment stability, and habitat health (Bosworth & Thibodeaux, 1990). However, bioturbation also complicates sediment analysis by disrupting natural stratigraphy, potentially impacting interpretations of past environmental conditions and sedimentary dynamics.

The Molucca Sea, noted for its rich marine biodiversity and complex oceanographic conditions, presents an ideal environment for studying bioturbation. This region serves as a pathway for major ocean current (ITF: Indonesian Throughflow) which drive complex water mass dynamics. This current influence sediment deposition (Alongi et al., 2013; Iskandar et al., 2023), nutrient distribution (Taufiqurrahman et al., 2020; Xie et al., 2024), and benthic ecosystems (Alongi et al., 2013), creating a highly dynamic marine environment. Changes in water masses, driven by climatic and oceanographic shifts, have significantly shaped the depositional history of the Molucca Sea, making it an important site for investigating past environmental changes. Examining bioturbation in this region can provide valuable insights into marine ecosystem dynamics and the reconstruction of sedimentary histories. Understanding bioturbation is crucial for accurate paleoenvironmental interpretations and for inferring past environmental conditions.

In sediment cores, bioturbation manifests through various features such as cylindrical or conical burrows, mucus-lined tubes from worms and mollusks, feeding traces like fecal pellets or bite marks, and biogenic structures such as mounds and pits. These features are critical for interpreting sediment cores, as they can alter sedimentary records and influence the reconstruction of past environmental conditions (Qunhui et al., 2008). The study of bioturbation is called ichnology, a branch of paleontology. Bioturbation features, also known as traces, and their fossilized versions, trace fossils (may be identified as ichnogenus and ichnospecies) are grouped into assemblages called ichnofacies. Marine ichnofacies have been used to interpret past environmental conditions across various geological ages (Crimes & Droser, 1992; Frey & Pemberton, 1985; Löwemark, 2007; Luo et al., 2020).

Bioturbation complicates sediment analysis by disrupting the natural layering of sediments. Burrowing organisms can create complex structures and mix sediment layers, challenging the principle of superposition, where older layers should lie beneath younger ones (Hülse et al., 2022; Pisias, 1983). This issue is particularly pronounced in high-biodiversity and dynamic environments such as the Molucca Sea. Understanding these complexities is essential for achieving accurate paleoenvironmental reconstructions and for interpreting the sedimentary history of marine ecosystems. Moreover, bioturbation can substantially impact age determination methods, both radiometric and non-radiometric, by disrupting the chronological integrity of sediment layers. Therefore, it is imperative to consider and account for the effects of bioturbation when conducting age determinations to ensure the accuracy and reliability of the results.

The Molucca Sea is renowned for its rich marine biodiversity and complex oceanographic conditions. Key factors such as water temperature, salinity, currents, and nutrient availability significantly influence the marine ecosystems in this region. One of the most prominent oceanographic features is the Banggai Upwelling, located in the southwest of the Molucca Sea, which plays a critical role in nutrient dynamics and marine productivity (Atmadipoera et al., 2018; Wiguna et al., 2024) emphasize that upwelling and past upwelling events bring nutrient-rich waters, profoundly impacting productivity in

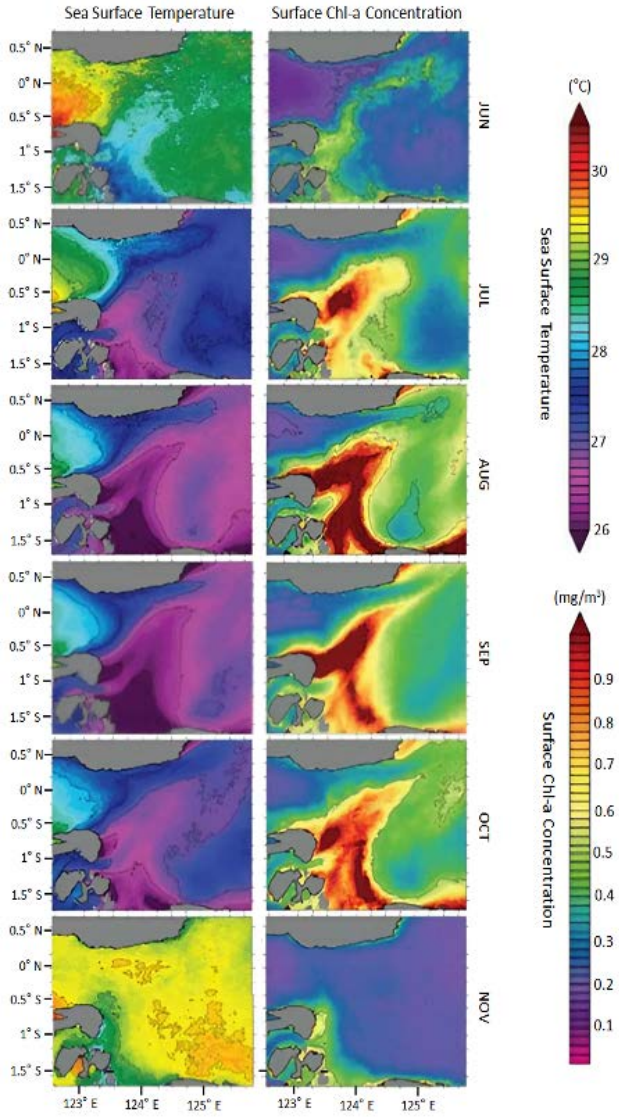

Figure 1. Upwelling events in the Molucca Sea, referred to as the Banggai Upwelling. The sea surface temperature (SST) (left) shows a low range of values (<27°C) during July–October 2015, which correlates with an increase in surface chlorophyll-a concentration (right) (modified from Atmadipoera et al., 2018).

this area (Figure 1). Bakun et al. (2015) suggested that an increase in global temperature will increase the intensity of the Eastern Boundary Upwelling System (EBUS) which lead to rising ocean acidity which will affect carbonate skeletal organisms. Further study by Petrick et al. (2015) inferred an expansion of Benguela Upwelling during warm events. To date, no published study on past upwelling has been carried out in the Indonesian Seas. To fill the gap, multi-discipline research was conducted in the Maluku Sea, Banggai Upwelling Dynamics Experiments and Ecosystem (BUDEE) cruise, onboard RV Baruna Jaya VIII in 2022 by the Research Center for Climate and Atmosphere – BRIN in collaboration with IPB University. The cruise successfully acquired five box core samples and four gravity cores that will help reveal past upwelling conditions to predict future changes. Studying sedimentary dynamics through trace fossils in the Maluku Sea is crucial because these biogenic structures provide direct evidence of benthic activity and environmental conditions during sediment deposition. High levels of bioturbation, characterized by diverse and complex trace fossils, often indicate favorable environmental conditions such as adequate oxygenation, stable sedimentation rates, and nutrient availability. Conversely, reduced or simplified bioturbation structures and the presence of lamination may reflect stressful conditions, such as low oxygen levels (hypoxia), high sedimentation

rates, or environmental disturbances. Hypoxia in marine sediments has been observed to be related to upwelling (Moffitt et al., 2015). Trace fossils serve as valuable proxies for reconstructing past depositional environments, revealing variations in hydrodynamic energy, sediment supply, and ecological stressors over geological time. These features can be analyzed to better understand the interactions between biological activity and sedimentary processes, providing key insights into how marine ecosystems respond to environmental changes and climatic variability.

This study aims to identify biogenic activities in seabed sediments to understand environmental changes in the study area. It will focus on assessing the density of bioturbation features to determine their impact on sediment dynamics. Additionally, this study will evaluate the viability of determining the age of these sediments by examining how bioturbation affects sediment structure. Furthermore, this study aims to investigate the influence of upwelling on trace fossil density and its relationship with environmental changes and sedimentary dynamics in the Molucca Sea.

MATERIALS AND METHODS

The data utilized in this study were derived from sediment samples collected from the seabed of the Molucca Sea (Figure 2) using a box corer with dimensions of 50 cm × 50 cm × 50 cm during BUDEE cruise in 2022 The sediment was extracted using a 3-inch PVC pipe and then split into two parts. One segment underwent CT scanning and XRF scanning for further analysis. Two sediment cores were utilized in this study (Figure 3a): BUDEE22-29BC (36.5 cm) collected from the upwelling region at coordinates 00°50'41.5709"S, 123°55'22.3885"E, with a depth of 2423 m, and BUDEE22-57BC (18.5 cm) collected from outside the upwelling area at coordinates (00°15'55.8097"N, 124°25'28.7600"E, with a depth of 2286 m.

Bioturbation data were obtained through CT scan imaging using a Siemens Somatom X.cite device (Figure 3b), which allows for the acquisition of 128 slices with a 0.5 mm thickness and a spatial resolution of 0.30 mm. The images were analyzed to identify bioturbation features using Synedra software. For data analysis, the bioturbation index (BI) as described by Gani (2020) was applied to evaluate and interpret the extent and impact of bioturbation in the sediment samples. The identification of trace fossil types and ichnogenera was conducted based on morphological characteristics observed in CT scan imagery. The interpretation refers to standard ichnological literature, including Fernández & Pazos (2012), Frey & Pemberton (1985), and Martin (2004), which provide diagnostic criteria for ichnogenera such as *Thalassinoides*, *Chondrites*, and *Planolites* in marine sedimentary environments.

The Zr/Rb ratio was used as an approach to grain size analysis because Zr and Rb are distributed differently across various sediment grain size fractions. Zr typically accumulates in heavy minerals found in coarser fractions, while Rb tends to concentrate in clay minerals found in finer fractions. Thus, the Zr/Rb ratio in sediments can provide information about changes in sediment grain size. A high Zr/Rb ratio indicates a dominance of coarse grains, whereas a low ratio suggests a predominance of fine grains (Dypvik & Harris, 2001). These elements were analyzed using an ITRAX micro XRF sediment core scanner with a Cr-tube set to 30 kV and 50 mA at the University of Bern in Switzerland. Due to irregularities, data collection intervals were adjusted, with BUDEE22-29BC ranging from 1 cm to 35.5 cm and BUDEE22-57BC from 0.5 cm to 16 cm. The vertical spatial resolution was set to 0.5 cm.

RESULTS

The sample BUDEE22-29BC exhibits significant bioturbation (Figure 4), indicative of active biological disturbance. Interestingly, the bioturbation in this core shows vertical segregation where the top part of the core (0-8 cm) is dominated by small-scale unlined bioturbation (0-8 cm) while the lower part of the core (8-36.5 cm), large-scale unlined bioturbation is predominant. The small-scale bioturbation (~0.2 cm) is characterized by lighter-color sediment-filled tunnel networks with small numbers of vertical systems. These structures are often associated with the ichnogenus *Chondrites*, known for their distinctive burrowing patterns. This ichnogenus is classified as feeding trace or fodichnia (Fernández & Pazos, 2012) and it is viewed as an adaptation to reduced oxygen condition (Martin, 2004). We use the presence of this ichnogenus as an indicator of hypoxia, which in turn signifies higher productivity due to upwelling.

The large bioturbation (0.5-1 cm) formed lateral tunnels of various sizes. The tunnels are darker in color than surrounding sediments, unlined and unornamented. Based on the characteristics that can be determined from the CT scan image, these

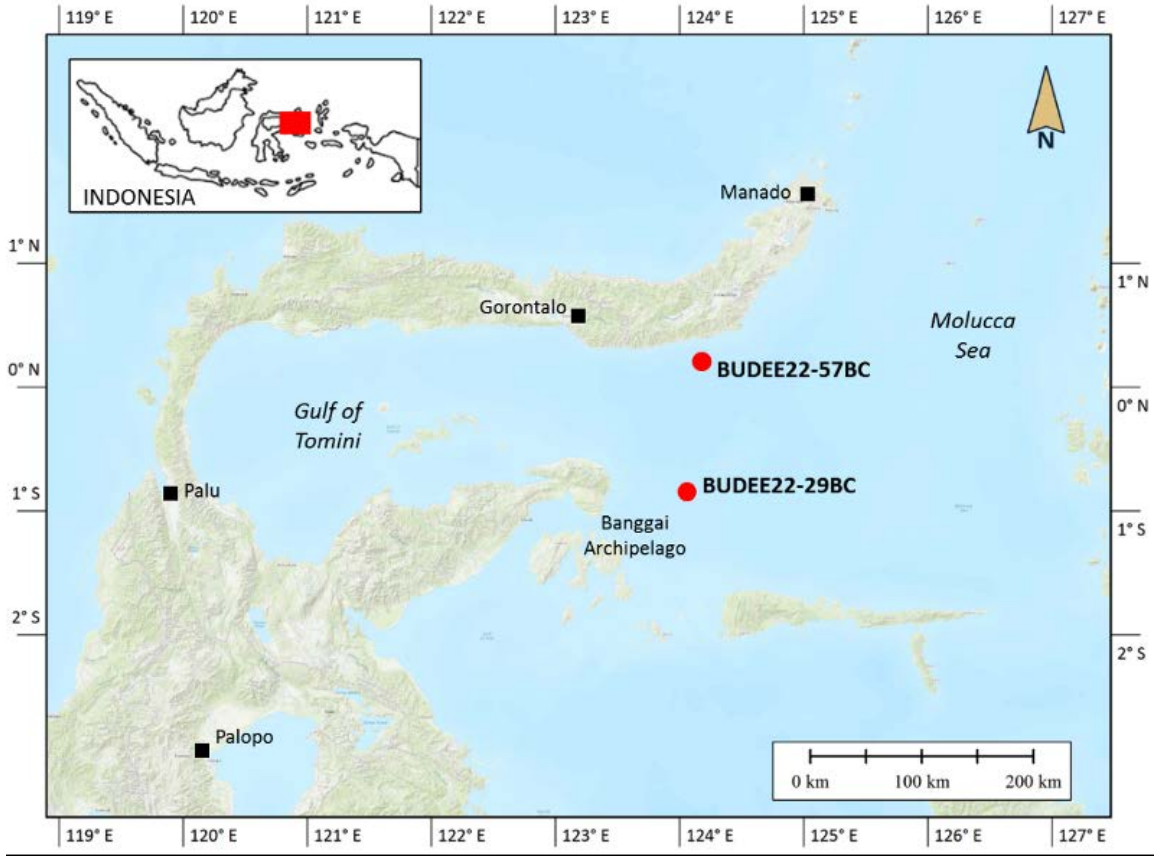

Figure 2. The research area situated in the Molucca Sea (inset map: highlighted in red square) includes two primary sites for core sampling in the study; BUDEE22-29BC and BUDEE22-57BC.

Figure 3. (a) Two samples were utilized in this evaluation; (b) CT scan applied in this study.

structures are identified as belonging to ichnogenus *Thalassinoides*, which is known for its extensive and complex burrowing activities.

Chondrites show increasing abundance to the upper layer, while *Thalassinoides* exhibit opposite trend. Based on the abundance of bioturbation, sample BUDEE22-29BC can be differentiated into two layers:

- Upper layer (0-8 cm) composed of clay that is moderately disturbed (50%) by bioturbation which is predominantly *Chondrites*, the traces are discrete with no overlap observed. From those characters, the bioturbation in this layer is classified as Bioturbation Index (BI) 3.
- Lower layer (8-36.5 cm) that consists of clay that is highly disturbed (70%) by some overlapping of tunnels and burrows that are dominated by *Thalassionoides*. Based on those features, the lower layer is classified into BI 4.

Sample BUDEE22-57BC also demonstrates bioturbation activities, though with distinct characteristics compared to BUDEE22-29BC. This core can be divided into 3 layers based on their bioturbation index (Figure 5):

- The upper part of the core (0-4.5 cm) shows intense bioturbation (diameter < 0.5 cm) and about 95% of the layer is disturbed. Two types of bioturbations were observed in this layer: cylindrical horizontal traces that are darker colored than surrounding sediments, and lighter colored burrows, that disturb sediment layers. Possible identification of the traces is hindered by the position of the traces that overlap each other. Because of these characteristics, this layer can be classified into BI 5.
- The middle part of the core (6.5-8.5 cm) is characterized by low to moderate bioturbation (BI 3-2, diameter ~0.5 cm). The traces that were observed in this layer are small unlined burrows that might be related to the ichnogenus
- *Planolites*, which are often found in marine sediments and are known for their simple, unlined burrowing patterns.
- The lower part of the core (8.5-18.5 cm) exhibits high bioturbation (75%) that destroys sedimentary structure. These characteristics put this layer into BI 4. The dominant bioturbation in this layer is large-scale bioturbation (diameter ~1cm), darker color than surrounding sediments, forming angled or J-shaped burrows, and associated with the ichnogenus *Thalassinoides*. These larger burrows suggest the presence of more robust organisms capable of creating extensive tunnel networks. The combination of small and large-scale bioturbation highlights a dynamic and diverse benthic ecosystem in the depositional environment of this sample.

The environmental profile of sample BUDEE22-29BC suggests fluctuating depositional conditions over time. The lower part of the sample exhibits less bioturbation, implying more stable and favorable conditions for benthic organisms, including increased bottom oxygenation. Conversely, the upper part of the sample shows more intense bioturbation, indicating a stressful environment for organisms, possibly due to upwelling-related low oxygenation, higher energy conditions, or variations in sediment supply. The environmental profile of sample BUDEE22-57BC reveals a more complex history of environmental changes. The middle part of the sample shows relatively undisturbed mud, indicating stable conditions that allowed for the preservation of fine sediment layers, or low oxygenation that various reasons, including upwelling, can cause. However, the upper and lower parts of the sample exhibit more intense bioturbation, suggesting periods of more extreme environmental fluctuations, such as changes in sedimentation rates or energy conditions that increase bottom oxygenation.

The Zr/Rb ratio in core BUDEE22-29BC fluctuates between 0.821 and 1.419, indicating substantial variability in sediment grain size across the depth profile. Higher ratios are observed at specific depths, such as at 16 cm (1.419) and 7 cm (1.358), suggesting the presence of coarser sediment layers. Conversely, lower ratios are recorded at 15 cm (0.845) and 32 cm (0.821), indicating layers with finer sediment. In contrast, the Zr/Rb ratios in core BUDEE22-57BC exhibit a more consistent pattern, with values ranging from 0.282 to 0.654. These relatively low Zr/Rb ratios indicate a general predominance of fine-grained sediments throughout the core. The lowest ratio is observed at 2.5 cm (0.282), while higher ratios, such as at 13.5 cm (0.654), reflect slightly coarser sediment layers. Despite these variations, fine-grained sediments

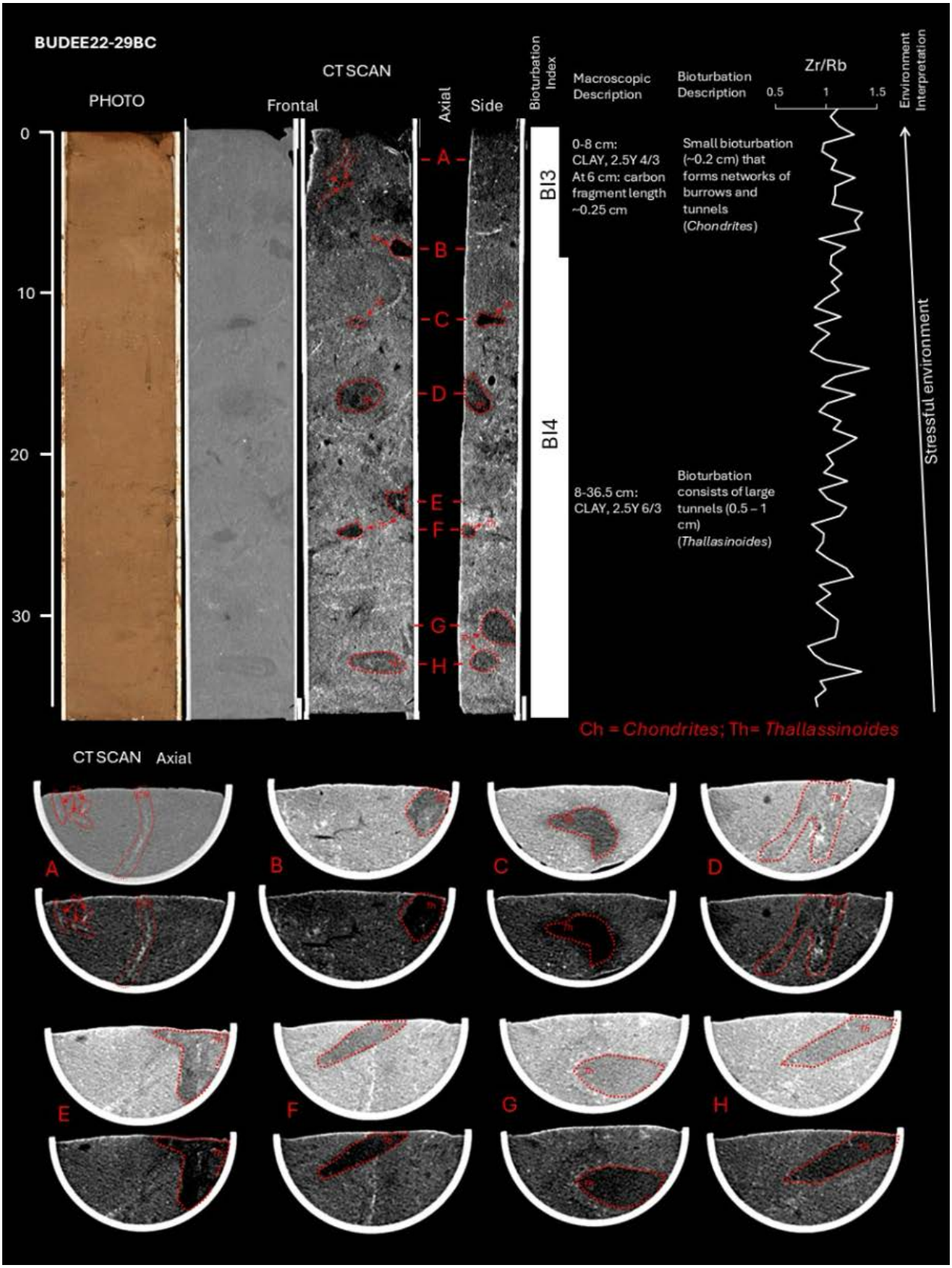

Figure 4. Core photo, CT scan, characteristics of sediments, ichnogenus, bioturbation density, and environment interpretation of BUDEE22-29BC. A-H indicates an axial CT scan showing each slice's lateral section.

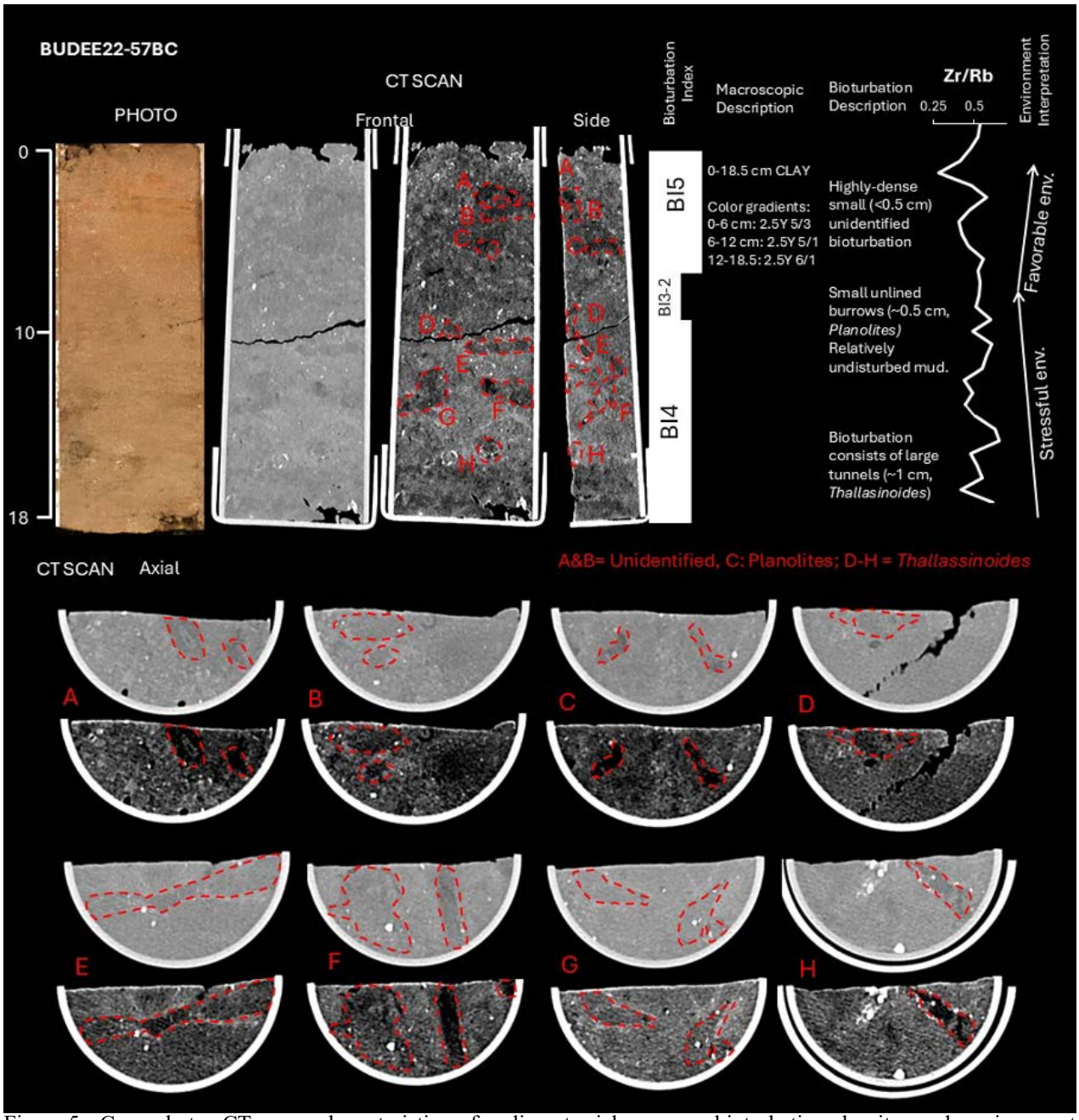

Figure 5. Core photo, CT scan, characteristics of sediments, ichnogenus, bioturbation density, and environment interpretation of BUDEE22-57BC. A-H indicates an axial CT scan showing each slice's lateral section.

dominate the overall profile in BUDEE22-57BC.

The upward increase in Zr/Rb ratio in BUDEE-29BC (Figure 4), indicating a transition toward coarser sediments, suggests higher-energy depositional conditions in the upper layers. This trend aligns with the reduced bioturbation intensity (BI 3) observed in the same layers, reflecting a more stressful environment over time, that might be formed as low oxygenation. In contrast, the lower layers, characterized by lower Zr/Rb ratios and high bioturbation intensity (BI 4), represent stable, low-energy depositional conditions with finer sediment with higher bottom oxygenation. The consistently low Zr/Rb ratios in BUDEE22-57BC (Figure 5) indicate a predominance of fine-grained sediments, corresponding with the intense bioturbation in the upper layers (BI 5). This combination suggests low-energy depositional conditions in the upper layers, while the middle layers, with reduced bioturbation intensity and simpler burrow structures, indicate periods of environmental stress, such as low oxygenation, or rapid sedimentation.

DISCUSSIONS

The two sediment samples, BUDEE22-29BC and BUDEE22-57BC, offer valuable insights into past depositional environments, particularly bottom oxygenation, and the influence of bioturbation on sediment dynamics. By reconstructing bottom oxygenation, we can infer changes in past upwelling, and by understanding the sediment dynamics, we can evaluate the viability of these sediments for age determination.

Depositional Environments in the Center of Upwelling (BUDEE22-29BC)

In sample BUDEE22-29BC, the bioturbation index (BI) decreases upward, with smaller bioturbation features becoming more prevalent. This trend suggests increasingly stressful environmental conditions over time, potentially due to lower bottom oxygenation, and/or increase of sedimentation rates and water energy conditions. This interpretation is supported by the Zr/Rb ratio that increases upward, indicating a shift towards coarser-grained sediments in the upper layers (Figure 4). An increase in Zr relative to Rb suggests higher-energy depositional conditions, consistent with the reduced bioturbation intensity observed in the upper layers (lower BI). This could reflect more stressful environmental conditions, such as higher sedimentation rates or less stable water conditions, which would limit bioturbation activity.

The high bioturbation intensity observed in core BUDEE22-29BC, particularly in its lower layers, suggests a stable depositional environment with moderate sedimentation rates. This is evidenced by the dominance of large-scale burrows attributed to the ichnogenus *Thalassinoides*. These features reflect conditions that likely supported robust benthic organisms, indicative of an oxygenated and nutrient-rich environment. The upper layers, characterized by smaller-scale bioturbation from *Chondrites*, point to a shift towards more stressful conditions, potentially caused by increased sedimentation rates or reduced oxygen availability, or increased energy that is indicated by increased grain size. This gradual transition highlights the dynamic nature of sediment deposition over time.

The absence of lamination, even though there is a slight increase in grain size, suggests mild hypoxia that in turn indicates upwelling (Moffitt et al., 2015). Two interpretations can be drawn based on BI and bioturbation sizes from this site: 1) there was a shift in the position of the upwelling center to site BUDEE22-29BC at present; 2) there was a change in upwelling intensity that increased to the present.

Depositional Environments in the Edge of Upwelling (BUDEE22-57BC)

Sample BUDEE22-57BC exhibits a more complex bioturbation pattern. The succession of bioturbation features suggests an increasingly stressful environment from the lower part of the core to the middle, potentially linked to higher energy conditions, sediment supply fluctuations, or other stressors. In contrast, the upper part of the core seems to transition to a more hospitable environment, possibly characterized by reduced turbidity, improved oxygen levels, and stable salinity and temperature, along with the presence of organic matter. The increased density of bioturbation features in the upper layers indicates these improved conditions, reflecting enhanced water column stability and sediment conditions. The presence of both small-scale and large-scale bioturbation features, associated with genera such as *Planolites* and *Thalassinoides*, highlights a diverse benthic community and shifting environmental conditions over time.

BUDEE22-57BC exhibits consistently lower Zr/Rb ratios, indicative of predominantly fine-grained sediments throughout the core with a slight upward decrease, aligning with the increasing bioturbation intensity (BI) in the upper layers (Figure 5). The decreased Zr/Rb indicates a shift toward finer-grained sediments, which is characteristic of lower-energy depositional environments. The corresponding increase in BI reflects a transition to more stable and hospitable conditions, likely driven by improved oxygen levels, reduced sedimentation rates, or changes in water dynamics.

Based on the BI and bioturbation sizes and ichnogenera, site BUDEE22-57BC shows changes in past upwelling intensity. The lower part indicates intermediate upwelling intensity that increased to stronger intensity in the middle layer before it became weaker. Although this site is at the edge of present-day upwelling center, the area could be affected by local coastal upwelling from July to October (Atmadipoera et al., 2018). Thus, changes in upwelling intensity in this site might be related to coastal upwelling instead of Banggai Upwelling system.

Viability of Sediments for Age Determination

The predominant bioturbation structures observed in sample BUDEE22-29BC are

characterized by horizontally oriented tunnels, indicative of lateral sediment displacement. This distinctive pattern of bioturbation offers potential for chronological analysis, as it may preserve undisturbed sediment layers within the tunnel infill, thereby providing suitable targets for age determination.

In contrast, BUDEE22-57BC shows more drastic environmental fluctuations, with a period of persistent stress followed by improved conditions in the upper layers. The lower and middle layers of BUDEE22-57BC remain viable for age determination. The bioturbation in these layers, primarily consisting of tunnels and burrows, does not significantly disrupt the vertical stratigraphy. The preservation of vertical layering in these sections supports their viability for chronological studies.

CONCLUSSIONS

The study on bioturbation densities and sizes, as indicators of sediment viability for age determination has been carried out on two box cores from Banggai Waters, Molucca Sea. The results suggest the potential shifting of the upwelling center (BUDEE22-29BC) and variations in upwelling intensity (BUDEE22-57BC), which have significantly influenced biogenic structures and sediment characteristics.

Trace fossil assemblages and bioturbation patterns reveal distinct environmental changes in the Molucca Sea. The transition from large-scale *Thalassinoides* in deeper layers to finer-scale *Chondrites* in upper layers of BUDEE22-29BC indicates increasing environmental stress, possibly driven by hypoxia related to upwelling. In contrast, BUDEE22-57BC reflects more complex environmental fluctuations with an initial period of stress followed by improved benthic conditions. These patterns provide strong evidence of past upwelling influence on bottom water oxygenation and ecosystem dynamics.

Sedimentary dynamics inferred from Zr/Rb geochemical proxies and bioturbation intensity indicate variations in depositional energy and sediment grain size. Upward increases in Zr/Rb ratios and reduced BI in BUDEE22-29BC reflect coarser-grained, higher-energy conditions, whereas BUDEE22-57BC shows fine-grained deposition under lower-energy conditions. These findings demonstrate the interplay between biological activity, physical sedimentation processes, and upwelling-driven environmental forces.

The preservation of stratigraphy and trace fossil characteristics in the lower parts of both cores confirms the viability of sediments from BUDEE22-57BC and BUDEE22-29BC for age determination. Despite potential bioturbation disturbances, the sedimentary sequences retain chronological integrity, making them suitable for paleoenvironmental and geochronological analysis.

ACKNOWLEDGEMENTS

The author expresses gratitude to the Baruna Jaya VIII crew, the National Research and Innovation Agency (BRIN), and IPB University for their invaluable support in data collection. This study was funded by Sailing Day Program Grant from BRIN no. 2307/II.7/HK.01.00/6/2022, and the National Geographic Explorer Grant #CP-087R-17. CT scans were conducted at the Institute for Forensic Medicine, and XRF scans at the Institute of Geological Sciences, both at the University of Bern. This work was made possible through collaboration with the Research Organization for Earth Sciences and Maritime-BRIN and the Institute of Geological Sciences at the University of Bern.

REFERENCES

Alongi, D. M., Brinkman, R., Trott, L. A., da Silva, F., Pereira, F., and Wagey, T., 2013. Enhanced benthic response to upwelling of the Indonesian Throughflow onto the southern shelf of Timor-Leste, Timor Sea. *Journal of Geophysical Research: Biogeosciences*, 118(1): 158–170. https://doi.org/10.1029/2012JG002150.

Atmadipoera, A. S., Khairunnisa, Z., and Kusuma, D. W., 2018. Upwelling characteristics during El Nino 2015 in Maluku Sea. *IOP Conference Series: Earth and Environmental Science*, 176(1). https://doi.org/10.1088/1755-1315/176/1/012018.

Bakun, A., Black, B. A., Bograd, S. J., García-Reyes, M., Miller, A. J., Rykaczewski, R. R., & Sydeman, W. J., (2015). Anticipated Effects of Climate Change on Coastal Upwelling Ecosystems. *Current Climate Change Reports*, 1(2): 85–93. https://doi.org/10.1007/s40641-015-0008-4.

Bosworth, W. S., and Thibodeaux, L. J., 1990. Bioturbation: A facilitator of contaminant transport in bed sediment. *Environmental*

Progress, 9(4): 211–217. https://doi.org/10.1002/ep.670090414.

Crimes, T. P., and Droser, M. L., 1992. Trace Fossils and Bioturbation: The Other Fossil Record. *Annual Review of Ecology, Evolution, and Systematics*, 23(23,): 339–360. https://doi.org/https://doi.org/10.1146/annurev.es.23.110192.002011.

Dypvik, H., and Harris, N., 2001. Geochemical facies analysis of fine-grained siliciclastics using Th/U, Zr/Rb and (Zr+Rb)/Sr ratios. *Chemical Geology*, 181: 131–146. https://doi.org/10.1016/S0009-2541(01)00278-9.

Fernández, D. E., and Pazos, P. J., 2012. Ichnology of Marginal Marine Facies of the Agrio Formation (Lower Cretaceous, Neuquén Basin, Argentina) at its Type Locality. *Ameghiniana*, 49(4): 505–524. https://doi.org/10.5710/AMGH.23.7.2012.439.

Frey, R. W., and Pemberton, S. G., 1985. Biogenic Structures in Outcrops and Cores. I. Approaches to Ichnology. *Bulletin of Canadian Petroleum Geology*, 33: 72–115. https://api.semanticscholar.org/CorpusID:130434650.

Gani, M. R., 2020. Clastic shorelines and deltas in 2020 *In:* N. Scarselli, J. Adam, D. Chiarella, D. G. Roberts, A. W. Balli (Editors), *Regional Geology and Tectonics: Principles of Geologic Analysis.* Elsevier B.V., Amsterdam: 343–364. https://doi.org/10.1016/B978-0-444-64134-2.00012-2.

Hülse, D., Vervoort, P., van de Velde, S. J., Kanzaki, Y., Boudreau, B., Arndt, S., Bottjer, D. J., Hoogakker, B., Kuderer, M., Middelburg, J. J., Volkenborn, N., Kirtland Turner, S., and Ridgwell, A., 2022. Assessing the impact of bioturbation on sedimentary isotopic records through numerical models. *Earth-Science Reviews*, 234, 104213. https://doi.org/https://doi.org/10.1016/j.earscirev.2022.104213.

Iskandar, M. R., Jia, Y., Sasaki, H., Furue, R., Kida, S., Suga, T., and Richards, K. J., 2023. Effects of High-Frequency Flow Variability on the Pathways of the Indonesian Throughflow. *Journal of Geophysical Research: Oceans*, 128(5): e2022JC019610. https://doi.org/10.1029/2022JC019610.

Löwemark, L., 2007. Importance and Usefulness of Trace Fossils and Bioturbation in Paleoceanography in 2007. *In*: W. Miller (Editor). *Trace Fossils: Concepts, Problems, Prospects*. Elsevier B.V., Amsterdam: 413–427. https://doi.org/10.1016/B978-044452949-7/50150-9.

Luo, M., Shi, G. R., Buatois, L. A., and Chen, Z.-Q., 2020. Trace fossils as proxy for biotic recovery after the end-Permian mass extinction: A critical review. *Earth-Science Reviews*, 203, 103059. https://doi.org/https://doi.org/10.1016/j.earscirev.2019.103059.

Martin, K. D., 2004. A re-evaluation of the relationship between trace fossils and dysoxia. *Geological Society, London, Special Publications,* 228(1): 141–156. https://doi.org/10.1144/GSL.SP.2004.228.01.08.

Moffitt, S. E., Moffitt, R. A., Sauthoff, W., Davis, C. V., Hewett, K., and Hill, T. M., 2015. Paleoceanographic Insights on Recent Oxygen Minimum Zone Expansion: Lessons for Modern Oceanography. *PLOS ONE*, 10(1): e0115246. https://doi.org/10.1371/journal.pone.0115246.

Petrick, B., McClymont, E. L., Felder, S., Rueda, G., Leng, M. J., and Rosell-Melé, A., 2015. Late Pliocene upwelling in the Southern Benguela region. *Palaeogeography, Palaeoclimatology, Palaeoecology*, 429: 62–71. https://doi.org/10.1016/j.palaeo.2015.03.042.

Pisias, N. G., 1983. Geologic time series from deep-sea sediments: Time scales and distortion by bioturbation. *Marine Geology*, 51(1): 99–113. https://doi.org/https://doi.org/10.1016/0025-3227(83)90091-9.

Qunhui, Y., Huaiyang, Z., Fuwu, J., Hu, W., & Weifang, Y., 2008. Bioturbation in Seabed Sediments and Its Effects on Marine Sedimentary Processes and Records. *Advances in Earth Science*, 23(9): 932–941. 10.11867/j.issn.1001-8166.2008.09.0932.

Taufiqurrahman, E., Wahyudi, A. J., and Masumoto, Y., 2020. The Indonesian throughflow and its impact on biogeochemistry in the Indonesian Seas. *ASEAN Journal on Science and Technology for Development*, 37(1): 29–35. https://doi.org/10.29037/AJSTD.596.

Wiguna, T., Yuwono, F. S., Zuraida, R., Atmadipoera, A., Vogel, H., Damanik, A., Tournier, N., and Cahyarini, S. Y., 2024. Paleoproductivity drivers in the Banggai

Waters, Sulawesi, Indonesia: Insights from elemental analysis of marine surface sediment. *BIO Web Conf.*, 106, 03008. https://doi.org/10.1051/bioconf/202410603008.

Xie, T., Cao, Z., Hamzah, F., Schlosser, P., and Dai, M., 2024. Nutrient Vertical Flux in the Indonesian Seas as Constrained by Non-Atmospheric Helium-3. *Geophysical Research Letters*, 51(24). https://doi.org/10.1029/2024GL111420.

THERMOCLINE WATER TEMPERATURE GRADIENT AT THE INDONESIAN THROUGHFLOW PATHWAYS DURING LAST GLACIAL MAXIMUM (LGM)

GRADIEN TERMOKLIN TEMPERATUR LAUT PADA JALUR ARUS LINTAS INDONESIA SAAT GLASIAL MAKSIMUM TERAKHIR

Rima Rachmayani[1*], Oktavira Dwi Demia Larasati[2], Marfasran Hendrizan[3]

[1] Research Group of Environmental and Applied Oceanography, Faculty of Earth Sciences and Technology, Bandung Institute of Technology, Indonesia

[2] Study Program of Earth Science, Faculty of Earth Sciences and Technology, Bandung Institute of Technology, Indonesia

[3] Paleoclimate and Paleoenvironment Research Group, National Research and Innovation Agency (BRIN), Indonesia

*Corresponding author: rrachmayani@itb.ac.id

(Received 08 April 2025; in revised from 10 April 2025; accepted 05 June 2025)

DOI : 10.32693/bomg.40.1.2025.937

ABSTRACT: This study aims to investigate the strength of the Indonesian Throughflow (ITF) during the Last Glacial Maximum (LGM) in comparison to the Pre-Industrial (PI) at the Makassar Strait, the Molucca Sea, and the Banda Sea, representing the pathways of the ITF. The analysis was performed based on the temperature distribution of the south (S) and north (N) thermocline gradients. Temperature data were obtained from the simulation of the Climate Community System Model, version 4 (CCSM4). The depth of the thermocline layer during the LGM and the PI period exhibits seasonal variability across the S-N stations. At Station 1, 2, and 3, the thermocline depth during the LGM ranges from 49 - 218 m (51 - 251 m), 55 - 250 m (69 - 254 m), and 48 - 238 m (48 - 218 m) in the south (north), respectively. The analysis of seasonal temperature variations in the thermocline layer in the three locations indicates that the ITF was significantly weakened both during the LGM and PI, indicated by the negative S-N Thermocline Water Temperature (TWT) gradient. The result suggests the southern part of each station is predominantly fresher compared to the northern part during these times. Additionally, it implies that the ITF is more robust in the eastern region (Banda Sea) during the LGM compared to the PI. This variation may relate to the intensity of seasonal local winds, mixing processes, and the remote influence of El Niño-like events, which could affect water transport along the pathway of the ITF.

Keywords: Thermocline Water Temperature, Indonesian Throughflow, Last Glacial Maximum, Makassar Strait, Molucca Sea, Banda Sea

ABSTRAK: *Penelitian ini bertujuan untuk menyelidiki kekuatan Arus Lintas Indonesia (Arlindo) selama Last Glacial Maximum (LGM) dibandingkan dengan Pra-Industri (PI) di Selat Makassar, Laut Maluku, dan Laut Banda, yang mewakili jalur Arlindo. Analisis dilakukan berdasarkan distribusi gradien suhu pada lapisan termoklin di stasiun bagian selatan (S) dan utara (N). Data suhu diperoleh dari simulasi Climate Community System Model, version 4 (CCSM4). Kedalaman lapisan termoklin selama LGM dan periode PI menunjukkan variabilitas musiman di seluruh stasiun S-N. Di Stasiun 1, 2, dan 3, kedalaman termoklin selama LGM berkisar antara 49 - 218 m (51 - 251 m), 55 - 250 m (69 - 254 m), dan 48 - 238 m (48 - 218 m) di selatan (utara), secara berurutan. Analisis variasi suhu musiman pada lapisan termoklin di tiga lokasi menunjukkan bahwa ITF melemah secara signifikan baik selama LGM maupun PI, ditunjukkan oleh gradien Thermocline Water Temperature (TWT) di stasiun S-N yang negatif. Hasil ini menunjukkan bahwa bagian selatan setiap stasiun menyimpan air tawar lebih banyak dibandingkan dengan bagian*

utara pada LGM dan PI. Selain itu, hal ini menyiratkan bahwa ITF lebih kuat di wilayah timur (Laut Banda) selama LGM dibandingkan dengan PI. Variasi ini mungkin berhubungan dengan intensitas angin lokal musiman, proses pencampuran, dan pengaruh dari El Niño-like, yang dapat mempengaruhi transpor massa air di sepanjang jalur ITF.

Kata Kunci: Thermocline Water Temperature, Arus Lintas Indonesia, Last Glacial Maximum, Selat Makassar, Laut Maluku, Laut Banda

INTRODUCTION

A key component of the Indonesian Throughflow (ITF), which moves warm water from the Pacific to the Indian Ocean, the thermocline is defined by a fast drop in temperature with depth (Gordon, 2005). Thermohaline circulation allows this mechanism to greatly affect world climate patterns (Gordon, 2005; Talley, 2013). Understanding the function of the thermocline in climate dynamics requires study of its temperature gradient over past, present, and future changes within the ITF. The thermocline temperature gradient between the northern and southern part of Makassar Strait, a key route for the ITF, has shown significant variation over the last 30,000 years. Moreover, it showed that the thermocline gradient was more pronounced between 13.4–19 kiloyears ago (ka) and 24.2–27 ka before present (BP) relative to the Holocene epoch at roughly 10 ka BP (Fan et al., 2018). El Niño-like climate conditions cause the ITF to weaken, which lowers trade wind stress. The thermocline inside the ITF is still influenced by monsoonal cycles and tidal mixing. Intensified water mixing in the austral winter produces a thicker mixed layer and more bottom stratification. The future thermocline temperature gradient of the ITF is expected to respond to climate change and associated oceanographic activities.

Studies (e.g., Holbourn et al., 2011; Feng et al., 2017; Zhang et al., 2024) show that changes in the Earth's orbit have affected the upper water layers of the ITF during the past 120,000 years, suggesting that upcoming orbital changes might also affect the thermocline configuration. Future changes are anticipated to come from a mix of human-induced climate change and natural oceanographic processes, hence stressing the need for ongoing monitoring and research to forecast and understand these changes.

A major geological era is the Last Glacial Maximum (LGM). The LGM is known as a time marked by worldwide cooling and a remarkable drop in sea levels. Relative to modern conditions, a sea level drop of up to 120 m (Peltier et al., 2006) exposed the Sunda Shelf, Gulf of Thailand, South China Sea, Java Sea, and Sahul Shelf during this time. El Niño-like circumstances affected the hydroclimatology of the Indonesian waters and the Pacific Ocean during the LGM (Ding et al., 2013; Fan et al., 2018; Pang et al., 2021). Climate conditions turned drier during the LGM, marked by lower atmospheric water content and rainfall, which raised surface salinity in the Indonesian waters (Xu et al., 2008; Linsley et al., 2010). Thus, the ITF showed less strength during the LGM era (Holbourn et al., 2011; Ding et al., 2013; Fan et al., 2018).

Every second, the IFT moves roughly 15 Sv (1 Sv = 10^6 m³/s) of water mass to the Indian Ocean (Sprintall et al., 2009; Gordon et al., 2010). Contributing about 12–13 Sv, the Makassar Strait is the ITF's primary transport path, accounting for 77% of the total (Gordon et al., 2010). The ITF affects the distribution of heat and salinity in the Pacific and Indian Oceans (Lee et al., 2015; Hu et al., 2019), therefore influencing temperature and precipitation patterns in nearby marine and terrestrial habitats. This has spurred a lot of study meant to grasp the historical development of the ITF. Numerous research investigations have been undertaken to analyse the evolution of ITF in the past using paleoceanographic reconstruction (Bradley, 1999; Holbourn et al., 2011; Ding et al., 2013; Hendrizan et al., 2017; Fan et al., 2018; Pang et al., 2021). However, knowledge of the ITF's evolution in the Makassar Strait and other ITF's pathways is somewhat limited.

The connection between the ITF and the thermocline has not been much studied using numerical modeling. Shen et al., 2023 discussed the ITF and thermocline variability associated with the El Niño-Southern Oscillation (ENSO) and the Indian Ocean Dipole (IOD) by using CMIP5 models. It showed a decline in ITF transport under global warming conditions by 2100 (Shen et al., 2023). Back to the past, Rachmayani et al., (2019) used the Community Climate System Model, version 3 – Dynamic Global Vegetation Model (CCSM3-DGVM), to investigate climatic variability during important Marine Isotope Stages (MIS), revealing seasonal temperature anomalies linked to local insolation. Zuyi (2003) studied the numerical

experiments where the closing of the ITF has caused notable changes in oceanic circulation, hence affecting temperature distributions in the tropical Pacific and Indian Oceans. Though numerical experiments have difficulties related to the complexity of regional climate systems and the limits of historical data, these models provide notable insights.

This study looks at the seasonal temperature distribution at certain ITF pathways, namely the Makassar Strait, Molucca Sea, and Banda Sea, from model output of CCSM4. By looking at temperature layer changes represented by thermocline water temperature gradient (TWT), this study highlights the strength of the ITF during the LGM in relation to PI conditions at the three mentioned locations.

METHODS

Study area

Figure 1 displays the area of interest, Indonesia, with three stations selected in the Makassar Strait (Station 1), the Molucca Sea (Station 2), and the Banda Sea (Station 3). The three stations are denoted with red dots in the north (N) and south (S) of each station. This is made to represent ITF pathways.

Data

Data was manageably taken from the World Data Center for Climate (WDCC). The WDCC is hosted by the German Climate Computing Center (Deutsches Klimarechenzentrum - DKRZ) in Hamburg, and it was openly accessed from https://www.wdc-climate.de/ui/. Since the past and recent climates are considered to be different, one time slice of the LGM at 21,000 years ago is selected to represent the period of glaciation, and the LGM climate is compared to the recent climate represented by PI as a reference. Investigation on TWT in this recent study is carried out by using the CCSM4 both in the LGM and PI model outputs (Brady et al., 2013) under the Paleoclimate Modelling Intercomparison Project, phase 3 (PMIP3) contribution to the Coupled Model Intercomparison Project, phase 5 (CMIP5), PMIP3-CMIP5 LGM experiments (Kageyama et al., 2021). Boundary conditions and forcings are summarised in Table 1.

Model

The CCSM4 is a general circulation model that integrates components for the atmosphere, ocean,

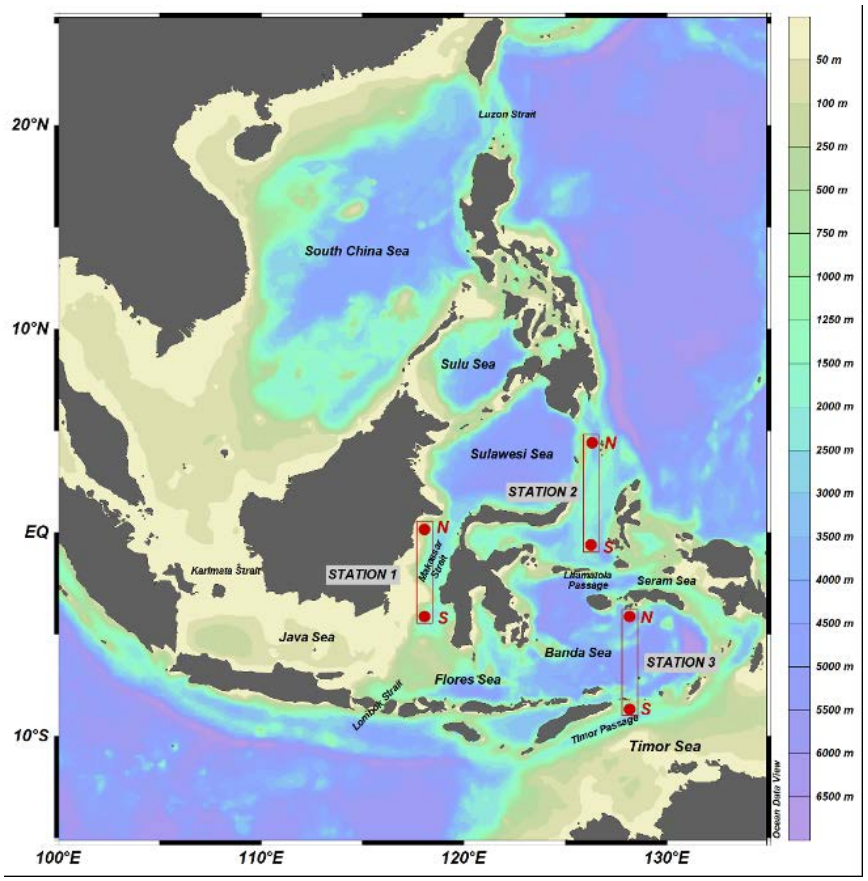

Figure 1. Study area of Indonesia. Shaded colours depict bathymetry; red dots exhibit N-S stations at the selected ITF pathways of Makassar Strait, Molucca Sea, and Banda Sea.

Tabel 1. Boundary conditions and forcings simulated by using CCSM4 (Brady et al., 2013) for LGM and PI experiments

Simulation	GHGs	Ice sheets	Orbital year	Vegetation/ aerosols	Length of simulation
PI	CO_2 = 284.7 ppm CH_4 = 791.6 ppb N_2O = 275.68 ppb	Modern Greenland and Antarctica	1990 CE	Pre-Industrial	1,300 yr
LGM	CO_2 = 185 ppm CH_4 = 350 ppb N_2O = 200 ppb	PMIP3 LGM	21 ka	PI	1,000 yr

Note:
CE= common era
ka= kilo- annum
yr= year
ppm= part per million
ppb= part per billion

land, and sea ice, exchanging information through a coupler which released in April 2010. Its atmospheric component, CAM4, features a 1.25° × 0.9° resolution with 26 vertical layers, improving El - Niño Southern Oscillation (ENSO) representation and high-latitude stability in LGM simulations. The land model, CLM4, shares the same resolution (Lawrance et al*.,* 2012), incorporating enhanced hydrology and a carbon–nitrogen biogeochemistry model, influencing vegetation responses to climate change. The ocean component (Smith et al*.,* 2010), based on the Parallel Ocean Program (POP2), utilizes a displaced grid with improved Gulf Stream dynamics and reduced sea surface temperature biases. It employs a standard displaced grid with poles positioned in Greenland and Antarctica and features 60 vertical levels (Danabasoglu et al., 2012a). The nominal 1° horizontal resolution consists of a uniform 1.1° spacing in longitude, while latitude varies from 0.27° at the equator to 0.54° at 33° latitude. The sea ice model, derived from the Community Ice Code (CICE4), enhances surface albedo and radiative transfer, leading to better Arctic Sea ice simulations (Hunke and Lipscomb, 2010; Holland et al., 2012) and operates on the same horizontal grid as the ocean component. Overall, CCSM4 introduces key improvements over previous versions, enhancing climate simulation accuracy (Brady et al*.,* 2019). Details on its development and documentation of the 1850 Common Era (CE) PI control simulation can be found in Gent et al. (2011). A wide range of additional simulations has been conducted with CCSM4 as part of CMIP5, including the Last Millennium (Landrum et al*.*, 2012) and future scenario simulations (Meehl et al*.*, 2012).

The LGM simulation, however, implements a more scale-selective fourth-order divergence damping to enhance high-latitude stability in CAM4 by mitigating grid-scale noise caused by steep ice sheets over North America and Greenland (Lauritzen et al*.,* 2012). CAM4 offers notable improvements, including a significantly better representation of the spatial and temporal characteristics of ENSO (Richter and Rasch, 2008; Neale et al., 2008; Deser et al*.,* 2012). For the climate change simulations in this study, while the plant functional type distribution remains fixed at preindustrial values (Lawrence and Chase, 2007), the leaf area index and vegetation height are prognostic and responsive to climate variations (Thornton et al., 2007). A newly implemented overflow parameterisation enhances the Gulf Stream's path and the meridional overturning circulation in the North Atlantic, leading to improved sea surface temperature and salinity accuracy compared to CCSM3 (Danabasoglu et al*.,* 2012b). The increased vertical resolution, especially in the upper ocean, helps mitigate sea surface temperature errors in major upwelling regions and refines the mean and annual cycle of sea surface temperature in the eastern Pacific along the equator (Gent et al*.,* 2011).

RESULTS

Seasonal Thermocline Changes During LGM and PI

Figure 2 shows sea temperature vertically from the surface to the deep layer at each N-S station to see the seasonal thermocline occurrences during the LGM. Figure 2a-b exhibits the seasonal thermocline

depth during LGM at Station 1 in the north (N) point at an average depth of 51-254 m and the south (S) point at an average depth of 49-218 m. Figure 2c-d illustrates the thermocline at Station 2 in the north (N) with an average depth of 69-254 m and south (S) points with an average depth of 55-250 m. Figure 2e-f presents the thermocline at Station 3 in the north (N) point with an average depth of 48-218 m and the south (S) point with an average depth of 48 -238 m. Judging from the results, the upper-to-lower seasonal thermocline depth at the three stations experiences slight seasonal changes from 21 to 36 m. Sea surface temperature (SST) at the three stations exhibits a slightly warmer temperature at the north points compared to the south points. Station 1 at Makassar Strait and Station 2 at Molucca Sea experience a similar range of SST of 25.5-27.5°C; meanwhile, Station 3 at Banda Sea experiences a colder SST in a range of 24.5-27.5°C. Seasonal SST changes are clearly seen at every south-north station where the coldest SST in the December-January-February (DJF) season represented by the month of February, is captured at the north stations of Makassar and the Molucca Sea, and the warmest SST is captured during September-October-November (SON) in November, as at every station in the south. Meanwhile, the coldest SST at the south stations occurs five months after February, that is, in July-August (June-July-August, JJA season). Furthermore, sea temperature during the LGM is captured as colder at the surface by 3-5°C and vertically in the thermocline until the deep layer by 2°C compared to the PI at every south-north station. However, the seasonal sea temperature pattern of the thermocline during PI at the three stations looks similar relative to the seasonal sea temperature pattern during LGM.

The thermocline layer depth during LGM and PI (Figure 3) seems similar to each, but varies at south (north) points, where the seasonal thermocline layer during LGM at Station 1 ranges from 36 to 211 m (43 to 224 m), and Station 2 ranges from 42 to 216 m and 53 to 226 m at the south and north stations, respectively. The seasonal thermocline layer at Station 3 ranges at the south (north) from 42 to 178 m (34 to 185 m). It is shown from Figure 2 and Figure 3 that the seasonal changes of the thermocline layer's depth are minor since the seasonal SST changes only occur in the mixed layer depth (MLD). The averaged seasonal thermocline depth at the three stations during LGM and PI is listed in Table 2.

Tabel 2. The averaged seasonal depth of thermocline at the three stations of Makassar Strait, Molucca Sea, and Banda Sea

No.	Location	Station	Upper Thermocline Depth (m)		Lower Thermocline Depth (m)		Maximum and Minimum Temperature at the Thermocline Layer (C)	
			LGM	PI	LGM	PI	LGM	PI
1	Makassar Strait	North	51	43	254	224	26.89-10.18	29.17-13.24
		South	49	36	218	211	26.28-11.34	28.94-13.01
2	Molucca Sea	North	69	53	254	226	26.48-10.25	29.53-12.18
		South	55	42	250	216	26.80-10.44	29.38-13.05
3	Banda Sea	North	48	34	218	185	27.62-12.06	29.19-13.10
		South	48	42	238	178	26.02-10.61	29.41-13.38

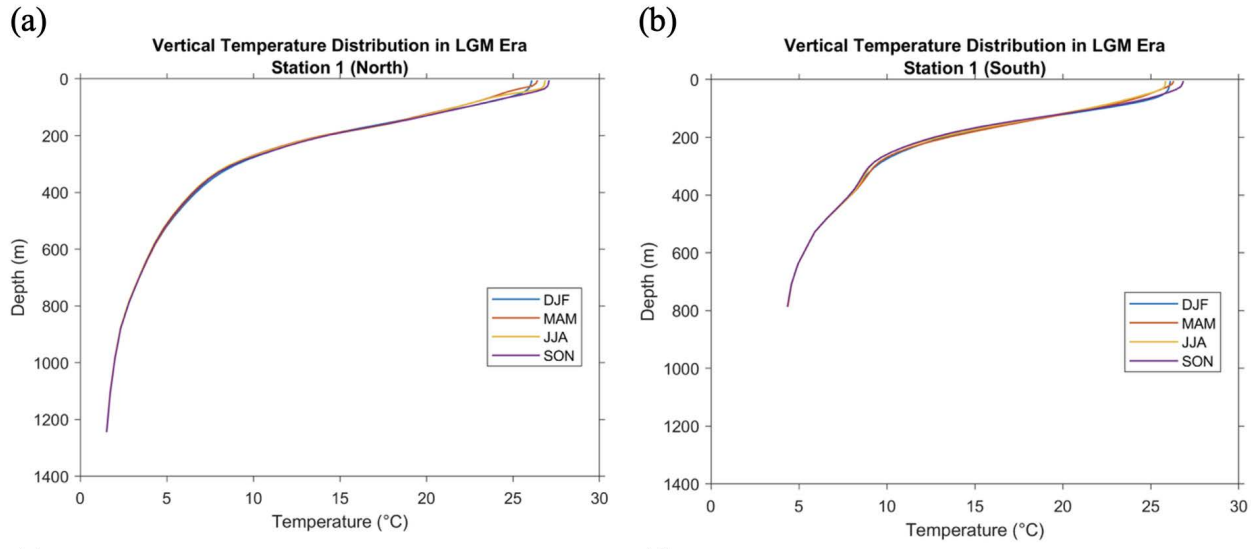

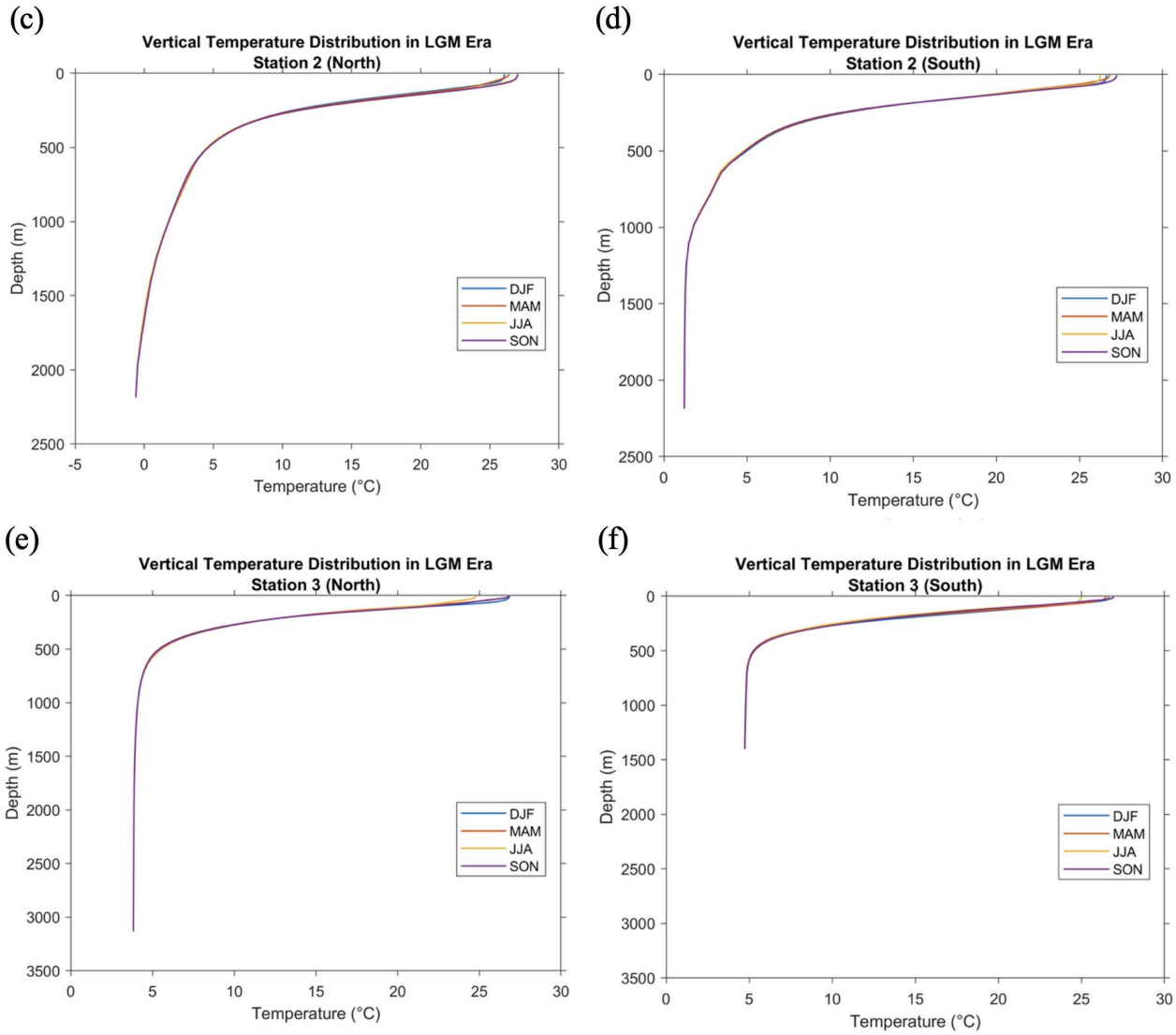

Figure 1. Seasonal vertical sea temperature at the three vertical stations: (a) 1-north, (b) 1-south, (c) 2-north, (d) 2-south, (e) 3-north, and (f) 3-south (see map in Figure 1). Coloured lines show the vertical sea temperature in December-January-February (DJF), March-April-May (MAM), June-July-August (JJA), and September-October-November (SON) during the LGM.

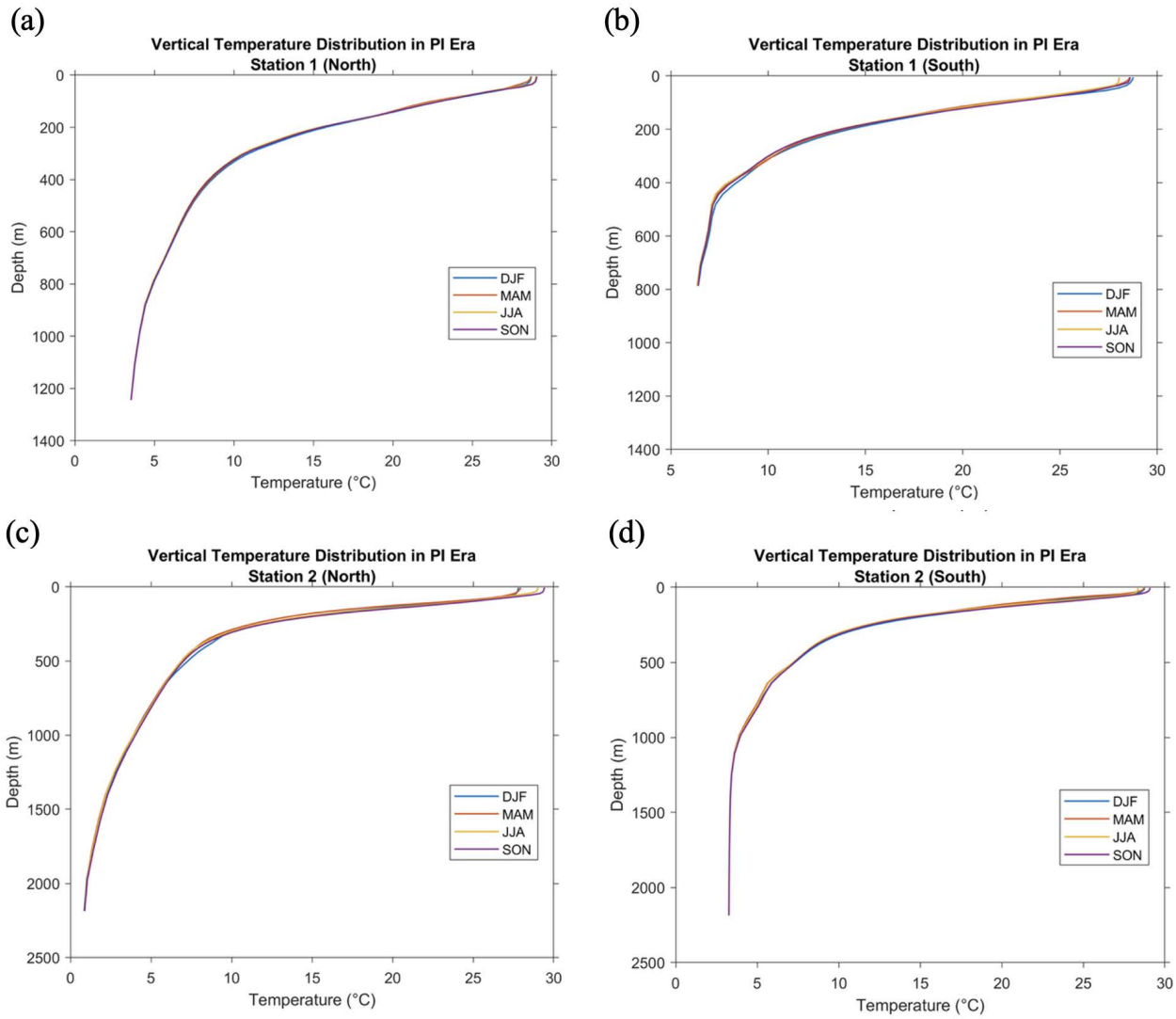

Figure 3. As in Figure 2, but for PI.

Seasonal Thermocline Water Temperature (TWT) Gradient during LGM and PI

Figure 4 addresses a gradient of TWT vertically from the surface to the thermocline layer at each S-N station (Table 2) to see the seasonal TWT occurrences during the LGM. Figures 4a-c exhibit the gradient of TWT at stations 1-3 between the south (S) and the north (N) points as listed in Table 2 with maximum depths at each station (Station 1=800 m, Station 2=2,250 m, Station 3=1,500 m). It can be seen that the vertical profile of the S-N TWT gradient at Station 1 (Makassar Strait), Station 2 (Molucca Sea), and Station 3 (Banda Sea) varies, where the negative S-N TWT gradient robustly is captured at 75-254 m depth down to -2.05 °C/m, 45-267 m depth down to -1.63 °C/m, and varies shallower from 25-251 m depth down to -1.25 °C/m at each mentioned station, respectively. While the positive S-N TWT gradient is apprehended lower than 105 m depth at Station 1 (Makassar Strait) up to 0.5 °C/m. Moreover, the positive S-N TWT gradient is captured robustly at 55-251 m depth up to 0.66 °C/m at Station 2 (Molucca Sea), at 25-251m up to 1.45 °C/m at Station 3 (Banda Sea). Additionally, seasonal changes of the S-N TWT gradient are clearly seen at each station. The most negative TWT gradient is exhibited during SON in September and October at 165 m depth, and the most positive TWT gradient is revealed during MAM in March at 85 m depth at Station 1 (Makassar Strait). Meanwhile, at Station 2 (Molucca Sea), the most negative TWT gradient is shown during JJA in July at 115 m depth, and the most positive TWT gradient is experienced during DJF in January at 65 m depth. At Station 3 (Banda Sea), the seasonal changes are similar to Station 1 (Makassar Strait), where the most negative TWT gradient is in September (SON) at 115 m depth, and the most

positive TWT gradient is demonstrated in February (DJF) at 155 m depth.

The S-N TWT gradient during LGM (Figure 4) is compared to the S-N TWT gradient in PI (Figure 5). It is revealed that the seasonal negative S-N TWT gradient vertically shifted and became shallower from 75-254 m depth during the LGM to 25-236 m depth during PI (Station 1, Makassar Strait). At station 2 (Molucca Strait), the negative S-N TWT gradient experienced at depths of 35-251 m during the PI shows a shallower depth at about 10 m compared to the LGM. The positive-to-negative shifted S-N TWT gradient at Station 3 (Banda Sea) occurs clearly at 25-222 m depth during the DJF in LGM compared to PI. Particularly, the TWT gradient during LGM and PI at the thermocline layer (Table 2), is displayed in Table 3.

Tabel 3. Seasonal averages of TWT gradient at the three stations of Makassar Strait, Molucca Sea, and Banda Sea during LGM and PI

No.	Location	Maximum Thermocline Depth at S-N Stations (m)		Seasonal	Seasonal averaged TWT gradient (ϕC/m)	
		LGM	PI		LGM	PI
1	Makassar Strait	49-254	36-224	DJF	-0.48	-1.07
				MAM	-0.29	-1.19
				JJA	-0.82	-1.39
				SON	-0.94	-1.14
2	Molucca Sea	55-254	42-226	DJF	0.15	-0.38
				MAM	-0.36	-0.58
				JJA	-1.08	-1.08
				SON	-0.77	-0.93
3	Banda Sea	48-238	34-185	DJF	0.49	-0.88
				MAM	0.70	0.31
				JJA	-0.32	0.19
				SON	-0.35	-0.74

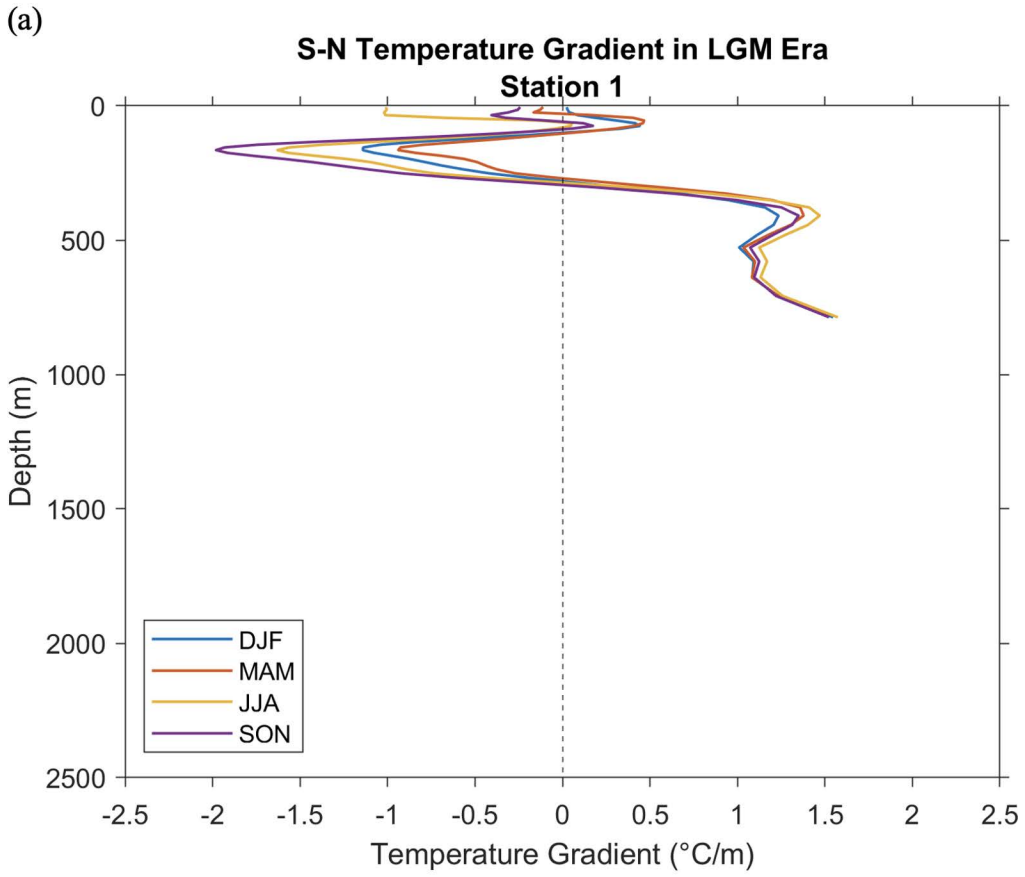

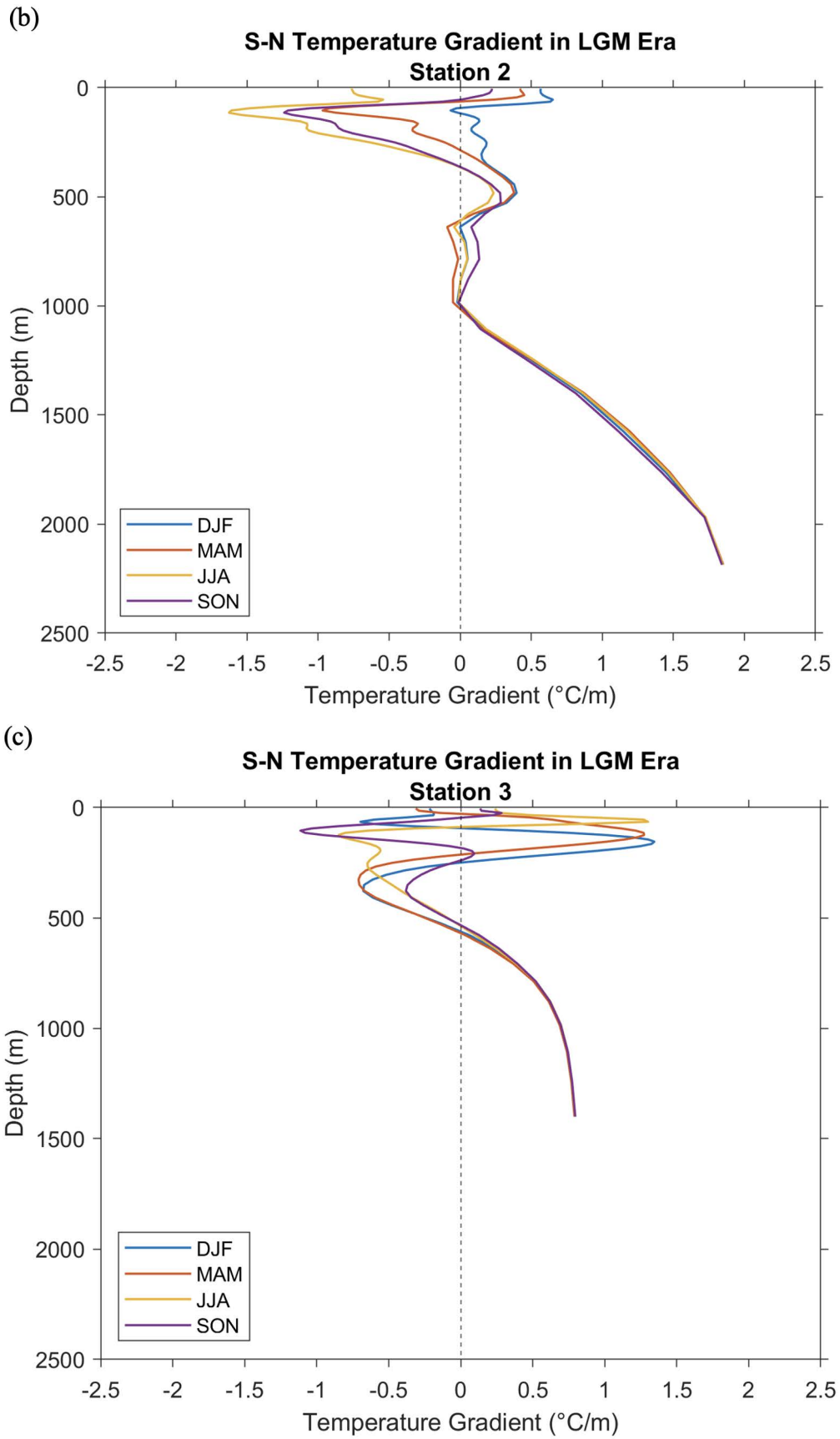

Figure 4. South-North (S-N) thermocline water temperature (TWT) gradient at the three vertical transects: (a) 1, (b) 2, (c) 3 (see map in Figure 1). Coloured lines show the gradient in December-January-February (DJF), March-April-May (MAM), June-July-August (JJA), and September-October-November (SON) during LGM.

(a)

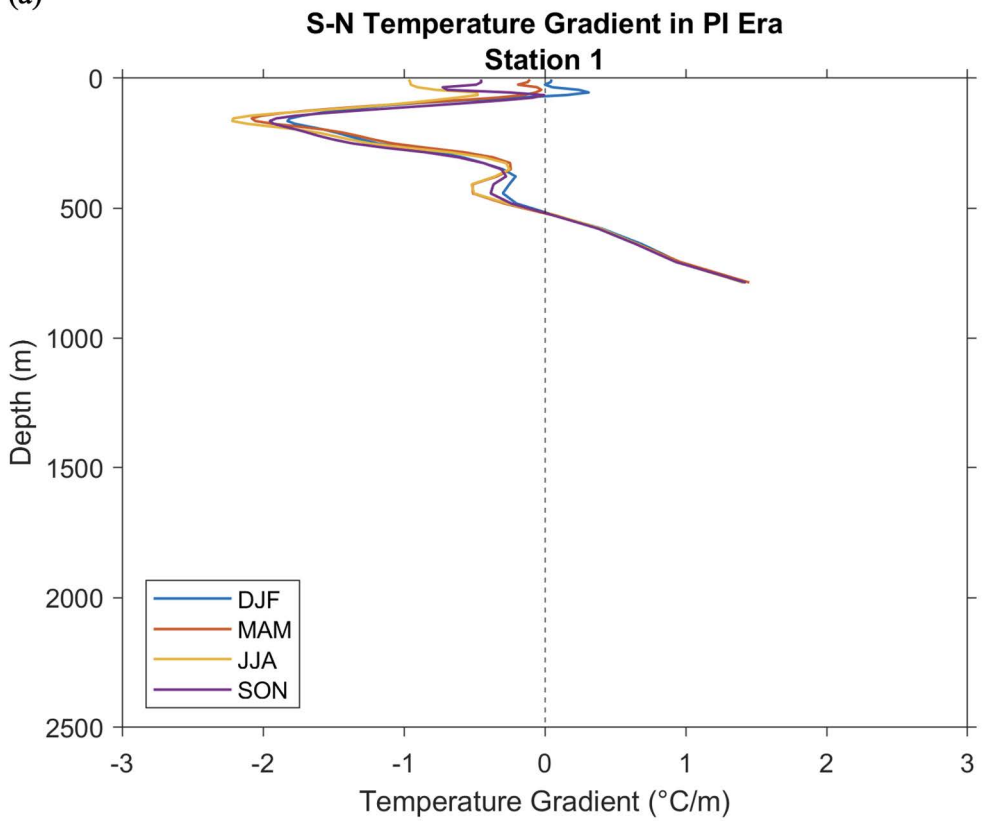
S-N Temperature Gradient in PI Era
Station 1
Depth (m)
0
500
1000
1500
2000
2500
-3
-2
-1
0
1
2
3
Temperature Gradient (°C/m)
DJF
MAM
JJA
SON

(b)

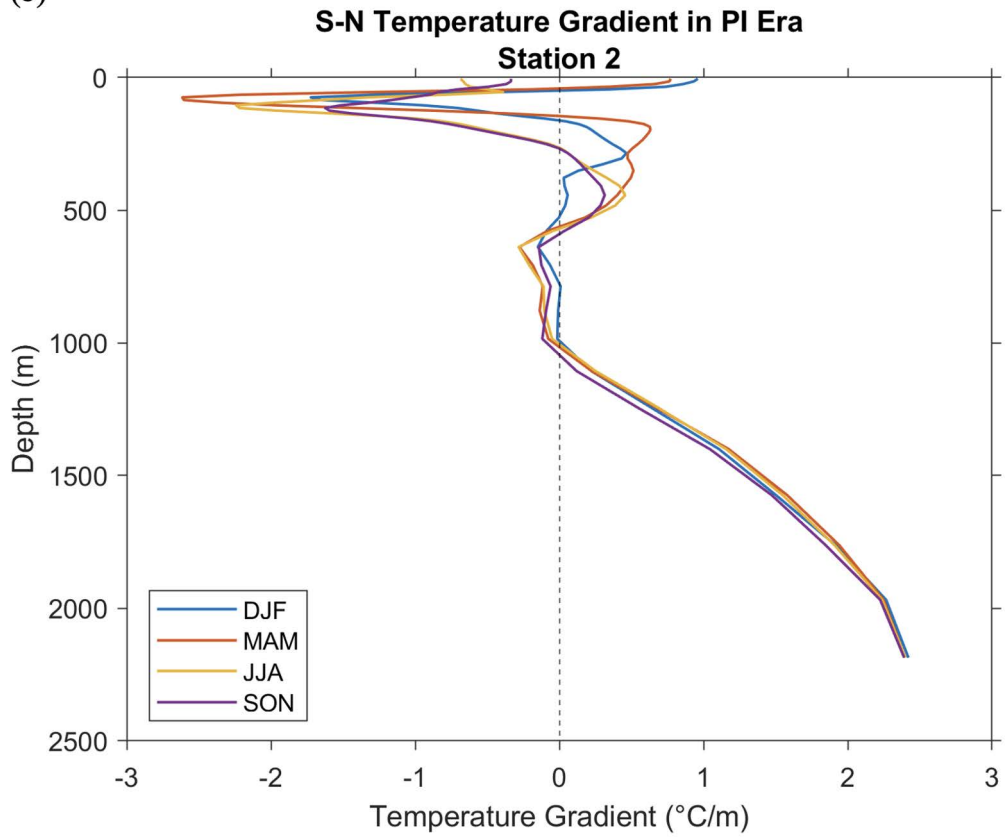
S-N Temperature Gradient in PI Era
Station 2
Depth (m)
0
500
1000
1500
2000
2500
-3
-2
-1
0
1
2
3
Temperature Gradient (°C/m)
DJF
MAM
JJA
SON

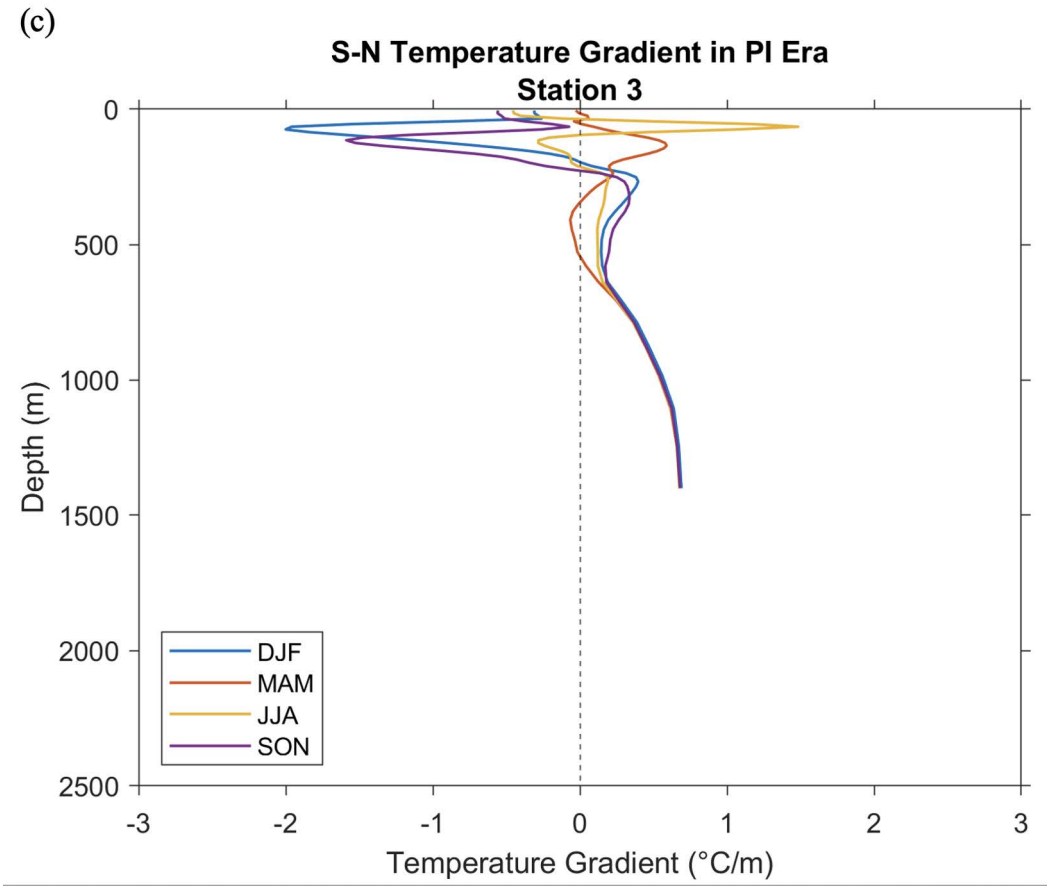

Figure 5. As in Figure 4, but for PI.

DISCUSSIONS

In equatorial regions, the thermocline develops due to solar radiation and heat transfer, resulting in a significant temperature gradient that limits further changes in heat movement. The ITF's significant role in global heat redistribution has led to extensive research on its historical variations. During the LGM, a substantial decrease in sea level of around 120 m likely resulted in notable alterations to the pathways, strength, thermal structure, and heat transport capacity of the ITF.

Analysis of the TWT gradient (Table 3) of the S-N points from the surface to each thermocline depth (Table 3) during the LGM at the Makassar Strait, Molucca Sea, and Banda Sea indicates that temperatures are generally warmer at northern points compared to southern points within this depth range. The S-N TWT gradient at the Makassar Strait demonstrates clear seasonal variation from the surface to maximum thermocline depth of 254 m, where a robust negative TWT gradient is found in all seasons. In contrast, the Molucca Sea experiences a predominantly positive TWT gradient during DJF. While in Banda Sea, positive TWT gradients are mainly captured in three seasons, except SON. However, the temperature profile at Molucca Sea and Banda Sea remains with dominant warmer at the northern points and cooler at the southern points, extending from the surface to a depth of ~75-251 m in the Molucca Sea and ~45-186 m in the Banda Sea. The Banda Sea exhibits a unique thermal profile, maintaining a balanced range of cooler and warmer temperatures from the surface to a depth of 236 m during specific months. This suggests that the water transport from the tropical Pacific Ocean to the Makassar Strait via the Celebes Sea undergoes alterations *en route* due to differing water characteristics.

In the ITF's primary pathway, surface and intermediate fresher waters interact with the saltier Pacific tropical waters, leading to a gradual reduction in salinity maximum. The outflowing ITF water exhibits a fresher and cooler thermocline, along with an isohaline layer. The Celebes Sea maintains high salinity characteristics; however, its subsurface salinity maximum decreases southward along the Makassar Strait, ultimately vanishing prior to reaching the Banda Sea. The subsurface temperature

is lower, and the thermocline is notably shallower in the southern Makassar Strait relative to the northern region (Table 2).

A comparison of surface and thermocline temperatures among these three locations facilitates an evaluation of paleo-ITF variability between the PI and the LGM. All three records indicate a larger south-north TWT gradient during two key periods—the PI and the LGM—suggesting that the southern Makassar Strait, Molucca Sea, and Banda Sea were relatively fresher (indicated by the negative S-N TWT gradient) in the thermocline layer during these times, seasonally (Figures 4-5, Table 3), except in Molucca Sea and Banda Sea in DJF during LGM, in Banda Sea in MAM during LGM and PI, in Banda Sea in JJA during PI. This negative S-N TWT gradient implies a primarily weakened ITF during both LGM and PI. Fan et al. (2018) suggested that the diminished ITF strength during LGM, attributed to decreased sea levels, likely led to weakened thermal advection, resulting in cooler temperatures in the southern region compared to the relatively warmer northern region. During the PI, a reduced TWT gradient indicates a more robust ITF, facilitating the mixing and transport of warmer waters from the Pacific through Makassar Strait and Molucca Sea, which then circulates the waters to Banda Sea. This procedure promoted a more consistent thermocline temperature throughout the strait. Additionally, it is posited that the tidal mixing intensity of the Indonesian Sea under LGM conditions was comparable to PI, and the explanation for the heightened contrast in thermocline across the Makassar Strait pertains to the intensity of the Makassar Strait Throughflow (MSTF). This intensity influences the extent of warmer and saltier thermocline water transported across the strait, thereby affecting the temperature and salinity gradients between the sediment cores located in the north-south orientation.

Furthermore, Fan et al*.,* (2018) determined that the Southeast monsoon contributed to oceanic upwelling, leading to vertical mixing that could produce a significantly cooler thermocline in the shoaled region. Likewise, this condition aligns with the observation that a weakened ITF consistently coincides with a strengthened Mindanao Current during a contemporary El Niño-like state. A stronger Mindanao Current may facilitate the eastward movement of warm, saline water from the North Pacific into the Pacific North Equatorial Counter current, resulting in a reduced flow of warm water westward into the ITF. The increased eastward transport of warm water in an El Niño-like state may further facilitate the eastward propagation of the equatorial Pacific atmospheric convection center during the LGM.

The TWT gradients in the Molucca Sea and Banda Sea have not been examined in prior research. Only a study on TWT at the ITF's exit of Timor Sea was explored and indicated that the ITF's passage through the Timor Sea likely weakened during the LGM due to shallower water depths in that region at that time (Xu et al., 2008; Holbourn et al., 2011). During the LGM in the Molucca Sea, a steeper TWT gradient was observed in months of JJA, suggesting limited inflow of the ITF. Cooler thermocline waters remained in the southern Molucca Sea as a result of diminished warm water transport (Figure 4 and Table 3).

The results from the S-N TWT gradient at Banda Sea during LGM (Figure 4c) align with either Ding et al., 2013, who proposed a strengthened ITF during DJF and MAM seasons (indicate by negative TWT gradient), or Xu et al., 2008 and Holbourn et al*.,* (2011), who suggested a weakened ITF during the LGM in the Timor Sea; in the rest of the seasons in Banda Sea. This variation may result from the Banda Sea functioning as a significant outflow area for the ITF, where the thermocline depth and temperature reflect the final adjustments of ITF waters prior to their entry into the Indian Ocean. During the PI, a distinct warmer thermocline temperature is observed at the northern point in DJF and SON seasons, while a cooler thermocline temperature is noted at the southern point, in contrast to the thermocline temperature recorded during the LGM, particularly in DJF.

The analysis of the TWT gradient at the three locations—Makassar Strait, Molucca Sea, and Banda Sea—during the LGM indicates that the ITF is more pronounced and stronger to the east (Banda Sea) of Indonesian waters compared to the other stations (Makassar Strait and Molucca Sea) and compared to PI in all seasons (indicate by the positive and larger TWT gradient). This variation may correlate with the intensity of seasonal local winds and mixing processes.

CONCLUSSIONS

This research examines the seasonal temperature distribution along specific ITF pathways in the Makassar Strait, Molucca Sea, and Banda Sea. The temperature distribution is examined in relation to the south (S) and north (N) thermocline water

temperature gradient to elucidate the strength of the ITF during the LGM in comparison to the present/PI. The depth of the thermocline layer during the LGM and the PI period appears comparable, yet it exhibits seasonal variability across southern and northern points. At Station 1, the thermocline depth during LGM ranges from 49 to 218 m in the south and 51 to 254 m in the north. At Station 2, it ranges from 55 to 250 m across the southern and northern points, while at Station 3, it spans from 48 to 238 m in the south and 48 to 218 m in the north. All three records indicate a larger south-north TWT gradient during the LGM—suggesting that the southern Makassar Strait, Molucca Sea, and Banda Sea were predominantly fresher compared to the northern part in thermocline layers during this time. The examination of the south-north TWT gradient across the Makassar Strait and Molucca Sea indicates a notable reduction in the ITF during the LGM, although this trend is not observed in the Banda Sea. The analysis of the TWT gradient at the Makassar Strait, Molucca Sea, and Banda Sea indicates that the ITF was stronger to the east (Banda Sea) of Indonesian waters relative to Makassar Strait and Molucca Sea during the LGM and compared to PI in all seasons. It has been suggested to be associated with decreased sea levels, leading to weakened thermal advection, resulting in cooler temperatures in the southern region compared to the relatively warmer northern region during the LGM. Moreover, this variation may relate to the intensity of seasonal local winds, mixing processes, and the remote influences of El Niño-like events, which could impact water transport along the pathway of the ITF. Further investigation is required to calculate ITF transport between the S-N stations vertically at each location.

ACKNOWLEDGEMENTS

Investigation on TWT in this recent study is carried out by using model output of Community Climate System Model, version 4. Data was manageably taken from the World Data Center for Climate (WDCC). The WDCC is hosted by the German Climate Computing Center (Deutsches Klimarechenzentrum - DKRZ) in Hamburg and it was openly accessed from https://www.wdc-climate.de/ui/. Moreover, this study was supported by funding from Kemenristek/BRIN under PROGRAM RISET DASAR KEMITRAAN year 2021, scheme WORLD CLASS RESEARCH (WCR), contract number 588a/IT1.C01/TA.00/2021 and Program Penelitian dan Pengabdian kepada Masyarakat ITB (PPMI-ITB) year 2019.

REFERENCES

Bradley, R.S., 1999. *Paleoclimatology: Reconstructing Climates of the Quaternary*. 2nd Edition, Academic Press, San Diego, 10p.

Brady, E.C., Otto-Bliesner, B.L., Kay, J.E., Rosenbloom, N., 2013. Sensitivity to Glacial Forcing in the CCSM4. *American Meteorological Society*, 26(6):1901-1925. https://doi.org/10.1175/JCLI-D-11-00416.1.

Brady, E.C., Stevenson, S., Bailey, D., Liu, Z., Noone, D., Nusbaumer, J., Otto-Bliesner, B. L., Tabor, C., Tomas, R., Wong, T., Zhang, J., Zhu, J., 2019. The Connected Isotopic Water Cycle in the Community Earth System Model version 1. *Journal of Advances in Modeling Earth Systems*, 11:2547–2566. https://doi.org/10.1029/2019MS001663.

Briegleb, B.P., and Light, B., 2007. A Delta-Eddington Multiple Scattering Parameterization for Solar Radiation in the Sea Ice Component of the Community Climate System Model. *University Corporation for Atmospheric Research*, *NCAR Technical Note* 4721STR, 100 pp.

Danabasoglu, G., Bates, S.C., Briegleb, B.P., Jayne, S.R., Jochum, M., Large, W.G., Peacock, S., and Yeager, S.G., 2012a. The CCSM4 ocean component. *Journal of Climate*, 25:1361–1389. https://doi.org/10.1175/JCLI-D-11-00091.1.

Danabasoglu, G., Yeager, S.G., Kwon, Y.O., Tribbia, J.J., Phillips, A., and Hurrell, J.W., 2012b. Variability of the Atlantic Meridional Overturning Circulation in CCSM4. *Journal of Climate*, 25:5153–5172. https://doi.org/10.1175/JCLI-D-11-00463.1.

Deser, C., Phillips, A., Tomas, R., Okumura, Y., Alexander, M., Capotondi, A., Scott, J., Kwon, Y.O., Ohba, M., 2012. ENSO and Pacific Decadal Variability in the Community Climate System Model Version 4. *Journal of Climate*, 25:2622–2651.

Ding, X., Bassinot, F., and Guichard, F., fang, N.Q., 2013. Indonesian Throughflow and monsoon activity records in the Timor Sea since the last glacial maximum. *Marine Micropaleontology*, 101:115 – 126.

Fan, W., Jian, Z., Chu, Z., Dang, H., Wang, Y., Bassinot, F., Han, X., Bian, Y., 2018. Variability of the Indonesian Throughflow in the Makassar Strait over the Last 30 ka. *Scientific Reports*, 8:5678. https://doi.org/10.1038/s41598–018–24055–1.

Feng, M., Zhang, N., Liu, Q., Wijffels, S., 2018. The Indonesian throughflow, its variability and centennial change. Geoscience Letters 5, 3. https://doi.org/10.1186/s40562-018-0102-2.

Gent, P.R., Danabasoglu, G., Donner, L.J., Holland, M.M., Hunke, E.C., Jayne, S.R., Lawrence, D.M., Neale, R.B., Rasch, P.J., Vertenstein, M., Worley, P.H., Yang, Z.-L., Zhang, M., 2011. The Community Climate System Model Version 4. *Journal of Climate*, 24:4973–4991. doi:10.1175/2011JCLI4083.1.

Gordon, A. L., 2005. Oceanography of the Indonesian Seas and Their Throughflow. *Oceanography*, 18(4):14-27.

Gordon, A. L., Sprintall, J., Van Aken, H. M., Susanto, D., Wijffels, S., Molcard, R., Wirasantosa, S., 2010. The Indonesian Throughflow during 2004–2006 as observed by the INSTANT program. *Dynamics of Atmospheres and Oceans*, 50(2):115–128. https://doi.org/10.1016/j.dynatmoce.2009.12.

Hendrizan, M., Kuhnt, W., and Holbourn, A., 2017. Variability of Indonesian Throughflow and Borneo Runoff During the Last 14 kyr. *Paleoceanography*, 32:1054–1069. https://doi.org/10.1002/2016PA003030.

Holbourn, A., Kuhnt, W., Xu, J., 2011. Indonesian Throughflow variability during the last 140 ka: the Timor Sea outflow. *Geological Society of London Special Publications*, 355:283–303. https://doi.org/10.1144/SP355.14.

Holland, M. M., Bailey, D. A., Briegleb, B. P., Light, B., and Hunke, E., 2012. Improved Sea Ice Shortwave Radiation Physics in CCSM4: The Impact of Melt Ponds and Aerosols on Arctic Sea Ice. *Journal of Climate*, 25:1413–1430.

Hu, S., Zhang, Y., Feng, M., Du, Y., Sprintall, J., Wang, F., Hu, D., Xie, Q., Chai, F., 2019. Interannual to Decadal Variability of Upper–Ocean Salinity in the Southern Indian Ocean and the Role of the Indonesian Throughflow. *Journal of Climate*, 32: 6403–6421. https://doi.org/10.1175/JCLI–D–19–0056.1.

Hunke, E. C., and Lipscomb, W. H., 2010. *CICE: The Los Alamos Sea Ice Model Documentation and Software User's Manual, Version 4.1.* Los Alamos National Laboratory. Tech. Rep. LA- CC-06-012, 76 pp.

Kageyama, M., Harrison, S. P., Kapsch, M.-L., Lofverstrom, M., Lora, J. M., Mikolajewicz, U., Sherriff-Tadano, S., Vadsaria, T., Abe-Ouchi, A., Bouttes, N., Chandan, D., Gregoire, L. J., Ivanovic, R. F., Izumi, K., LeGrande, A. N., Lhardy, F., Lohmann, G., Morozova, P. A., Ohgaito, R., Paul, A., Peltier, W. R., Poulsen, C. J., Quiquet, A., Roche, D. M., Shi, X., Tierney, J. E., Valdes, P. J., Volodin, E., and Zhu, J., 2021. The PMIP4 Last Glacial Maximum experiments: preliminary results and comparison with the PMIP3 simulations. *Climate of the Past*, 17(3):1065–1089.

Landrum, L., Holland, M.M., Schneider, D.P., and Hunke, E., 2012. Antarctic Sea Ice Climatology, Variability, and Late Twentieth-Century Change in CCSM4. *Journal of Climate*, 25:4817–4838. https://doi.org/10.1175/JCLI-D-11-00289.1.

Lauritzen, P. H., Mirin, A.A., Truesdale, J., Raeder, K., Anderson, J.L., Bacmeister, J., and Niele, R., 2012. Implementation of new diffusion/filtering operators in the CAM-FV dynamical core. *International Journal of High Performance Computing Applications,* 26:63–77.

Lawrence, P. J., and Chase, T. N., 2007. Representing a new MODIS consistent land surface in the Community Land Model (CLM3.0). *Journal Geophysical Research,* 112:G01023. https://doi.org/10.1029/2006JG000168.

Lee, S.K., Park, W., Baringer, M.O., Gordon, A.L., Huber, B., Liu, Y., 2015. Pacific origin of the abrupt increase in Indian Ocean heat content during the warming hiatus. *Nature Geoscience*, 8:445–449. https://doi.org/10.1038/ngeo2438.

Linsley, B.K., Rosenthal, Y., Oppo, D.W., 2010. Holocene evolution of the Indonesian Throughflow and the Western Pacific Warm Pool. *Nature Geoscience*, 3:578–583.

Meehl, G. A., and Coauthors, 2012. Climate System Response to External Forcings and Climate

Change Projections in CCSM4. *Journal of Climate*, 25:3661–3683.

Neale, R. B., Richter, J. H., and Jochum, M., 2008. The Impact of Convection on ENSO: From a Delayed Oscillator to a Series of Events. *Journal of Climate*, 21:5904–5924.

Pang, X., Bassinot, F., Sepulcre, S., 2021. Indonesian Throughflow variability over the last two glacial–interglacial cycles: Evidence from the eastern Indian Ocean. *Quaternary Science Reviews*, 256. https://doi.org/10.1016/j.quascirev.2021.106839.

Peltier, W. R. and Fairbanks, R. G., 2006. Global glacial ice volume and Last Glacial Maximum duration from an extended Barbados sea level record. *Quaternary Science Reviews*, 25:3322–3337. https://doi.org/10.1016/j.quascirev.2006.04.010.

Rachmayani, R., Prange, M., Schulz, M., dan Ningsih, S. N., 2019. Climate Variability in Indonesia from 615 Ka to Present: First Insights from Low-Resolution Coupled Model Simulations. *Die Erde*, 150(4). https://doi.org/10.12854/erde-2019-428.

Richter, J. H., and Rasch, P. J., 2008. Effects of Convective Momentum Transport on the Atmospheric Circulation in the Community Atmosphere Model, version 3. *Journal of Climate*, 21:1487–1499.

Shen, C., Moore, J.C., Kuswanto, H., Zhao, L., 2023. The Indonesian Throughflow circulation under solar geoengineering. *Earth Dynamics System*, 14(6):1317–1332. https://doi.org/10.5194/esd-14-1317-2023.

Smith, R. D., and Coauthors, 2010. *The Parallel Ocean Program (POP) reference manual*. Los Alamos National Laboratory Tech. Rep. LAUR-10-01853, 140 pp.

Sprintall, J., Wijffels, S.E., Molcard, R., Jaya, I., 2009. Direct estimates of the Indonesian throughflow entering the Indian Ocean: 2004–2006. *Journal Geophysical Research*, 114:C07001. https://doi.org/10.1029/2008JC005257.

Talley, L., 2013. Closure of the Global Overturning Circulation Through the Indian, Pacific, and Southern Oceans: Schematics and Transports. *Oceanography*, 26:80–97. https://doi.org/10.5670/oceanog.2013.07.

Thornton, P., et al., 2007. Vulnerability, climate change and livestock: Research opportunities and challenges for poverty alleviation. *SAT eJournal*, 4:1-23. www.icrisat.org/journal/SpecialProject/sp7.pdf.

Xu, J., Holbourn, A., Kuhnt, W., Jian, Z., Kawamura, H., 2008. Changes in the thermocline structure of the Indonesian outflow during Terminations I and II. *Earth Planet Science Letter*, 273:152–162. https://doi.org/10.1016/j.epsl.2008.06.029.

Zhang, P., Xu, J., Holbourn, A., Kuhnt, W., Pei, R., Xiong, Z., Li, Ti., 2024. Precession-Driven Variations in the Indonesian Throughflow Thermocline and Its Implications on the Agulhas Leakage. *Geophysical Research Letters*, 51. https://doi.org/10.1029/2024GL110520.

STUDY OF HEAVY METAL LEAD (PB) IN THE NORTHERN WATERS OF BELITUNG REGENCY

STUDI KANDUNGAN LOGAM BERAT TIMBAL (PB) DI PERAIRAN UTARA KABUPATEN BELITUNG

Salsabila Fathona[1*], Rima Rachmayani[1], Ayu Utami Nurhidayati[2], Dwi Amanda Utami[2]

[1] Oceanography Study Program, Institut Teknologi Bandung

[2] Research Center for Climate and Atmosphere, Paleoclimate and Paleoenvironment Research Group, National Research and Innovation Agency Republic of Indonesia

*Corresponding author: salsabilaafath@students.itb.ac.id

(Received 11 November 2023; in revised from 1 December 2023 accepted 14 April 2025)

DOI : 10.32693/bomg.40.1.2025.860

ABSTRACT: Belitung Regency has significant tin potential, spread across the land, rivers, and beaches which have been mined for hundreds of years. However, tin mining activities are indicated to be a source of pollution in the northern region of Belitung Regency. This study aims to determine the distribution of the lead (Pb) concentrations in sediments and water columns in the northern waters of Belitung Regency and to evaluate the seasonal effect, particularly ocean currents, on the distribution patterns. In situ data were collected during the westerly season, including sediment samples, water column samples, and oceanographic parameters such as seawater quality and current measurements. During the easterly season, only sediment samples were obtained. Pb concentrations in sediments and water samples were analyzed at the National Research and Innovation Agency (BRIN) laboratory using the Atomic Absorption Spectrophotometry (AAS) method. The results showed that Pb concentrations in sediment samples ranged from 10.08 to 50.08 mg/kg during the easterly season, and from 10.96 to 60.72 mg/kg during the westerly season. In the water column, Pb concentrations ranged from 0 to 0.05 mg/L during the westerly season. The distribution pattern of Pb in sediments in the easterly season tended to spread offshore, while in the westerly season it is accumulated in the river. These patterns are influenced by seasonal flow variations, geographical location, and sediment grain size. Pb concentrations in sediments are higher in the westerly season compared to the easterly season. This is likely due to increased erosion and surface runoff during the rainy season, which leads to greater deposition of heavy metals in marine sediments.

Keywords: AAS, Belitung Regency, Lead (Pb), ocean currents, sediment, water column

ABSTRAK: *Wilayah Kabupaten Belitung memiliki potensi timah cukup besar yang tersebar di darat, sungai dan pantai yang telah ditambang sejak ratusan tahun lalu. Namun aktivitas pertambangan timah tersebut diindikasikan menjadi sumber pencemar wilayah utara Kabupaten Belitung. Tujuan dari penelitian ini yaitu mengetahui sebaran konsentrasi logam timbal (Pb) dalam sedimen dan kolom air di perairan utara Kabupaten Belitung, serta mengetahui pengaruh musim, terutama arus laut terhadap sebaran konsentrasi Pb. Pengambilan data dilakukan secara insitu, data yang ambil berupa sampel sedimen, sampel kolom air, dan parameter oseanografi seperti kualitas air dan arus laut, pada musim barat dan sampel sedimen pada musim timur. Konsentrasi Pb dalam sedimen dan kolom air dianalisis di laboratorium Badan Riset dan Inovasi Nasional (BRIN) menggunakan metode Atomic Absorption Spectrophotometry (AAS). Hasil penelitian menunjukkan konsentrasi Pb di sampel sedimen pada musim timur sebesar 10,08 – 50,08 mg/kg sedangkan pada musim barat sebesar 10,96 – 60,72 mg/kg. Pola sebaran kandungan*

Pb dalam sedimen pada musim timur cenderung menyebar ke arah lepas pantai, sedangkan pada musim barat terakumulasi di sungai. Hal ini dipengaruhi oleh pola aliran musiman yang berbeda, letak geografis, dan ukuran butir sedimen (jenis sedimen). Pada musim barat, konsentrasi Pb dalam sedimen lebih tinggi dibandingkan dengan musim timur. Hal ini disebabkan karena pada musim hujan banyak terjadi erosi dan masuknya limpasan air ke badan air, sehingga lebih banyak logam berat yang terendapkan dalam sedimen.

Kata Kunci: *AAS, Kabupaten Belitung, Timbal (Pb), arus laut, sedimen, kolom air*

INTRODUCTION

Heavy metals are classified as inorganic metal chemicals with a specific gravity of more than 5 gr/cm³. They exhibit toxic properties when introduced into water bodies in amounts exceeding certain thresholds. The presence of heavy metals poses significant environmental and health risks due to their toxicity, which can adversely affect humans, animals, and plants (Tchounwou et al., 2012). Heavy metals in nature exhibit several distinct properties or characteristics, such as persistence, difficulty to degrade, accumulation in ecosystems, and long half-lives. Among these, mercury (Hg), lead (Pb), and bismuth (Bi) are particularly notable for having the highest levels of these characteristics. These metals are highly persistent, resistant to degradation, prone to bioaccumulation, and possess exceptionally long half-lives compared to other heavy metals (Duffus, 2002). These properties make them particularly hazardous to both environmental and human health, as they can remain in ecosystems for extended periods and accumulate in living organisms, leading to toxic effects over time. Heavy metals in nature can come from two main sources, which are natural and anthropogenic sources. Heavy metals that come from natural sources come from rock weathering, the deposition of particles in the atmosphere, and the lava emitted by volcanoes during an eruption. Meanwhile, anthropogenic sources come from human activity waste such as residential and industrial waste, as well as mining, agricultural, and other waste activities (Demirak et al., 2006; Ghrefat and Yusuf, 2006; Khaled et al., 2006; Singh et al., 2006).

The Bangka Belitung Islands Province (Babel) is known as the only tin-producing region in Indonesia. Tin mining activities inevitably generate waste in the form of tailings containing high concentrations of lead (Pb) (Herman, 2006). These tailings are often not managed properly, allowing them to disperse into aquatic environments through surface runoff, infiltration into the soil, or transport by river flows to the sea. Mining activities can also expose heavy metal content previously trapped in geological formations, thereby increasing the release of Pb into aquatic ecosystems, including rivers surrounding tin mining sites. Additionally, dredging and washing of tin ore can accelerate the mobility of Pb in water and sediments, increasing the risk of bioaccumulation in aquatic organisms and the entry of this heavy metal into the food chain (Shazili et al., 2006). Rivers contaminated with Pb will flow into the sea, continuing the hydrological cycle by carrying dissolved chemical elements that can accumulate in aquatic environments (Soegianto, 2019). This accumulation can lead to coastal pollution, potentially damaging marine ecosystems and causing toxic effects on marine biota. In the long term, Pb contamination not only impacts the health of aquatic organisms but also poses a threat to human health through the consumption of contaminated seafood (Guo et al., 2020).

The main problems associated with heavy metals are toxicity, bioaccumulation, and biomagnification, which cause significant effects on ecosystems, human health, and other living organisms. Therefore, it is very important to know the distribution of heavy metal contamination to interpret the mechanisms of accumulation and transportation of heavy metals into the aquatic environment influenced by oceanographic factors and obtain the necessary information for monitoring, maintenance, and utilization of coastal management areas (DeForest et al., 2007; Demirak et al., 2006; Naser, 2013; Ozkan and Buyukisik, 2012; Wang and Rainbow, 2008). This research aims to determine the concentration of heavy metal lead (Pb) in sediment and water samples so that the distribution pattern can be known, which is influenced by oceanographic phenomena in the northern waters of Belitung Regency.

METHODS

The research area is located in the northern waters of Belitung Regency, Bangka Belitung Province, with three areas as the focus of research: the coastal area, estuary, and offshore (Figure 1). Sediment sampling was conducted at 13 stations

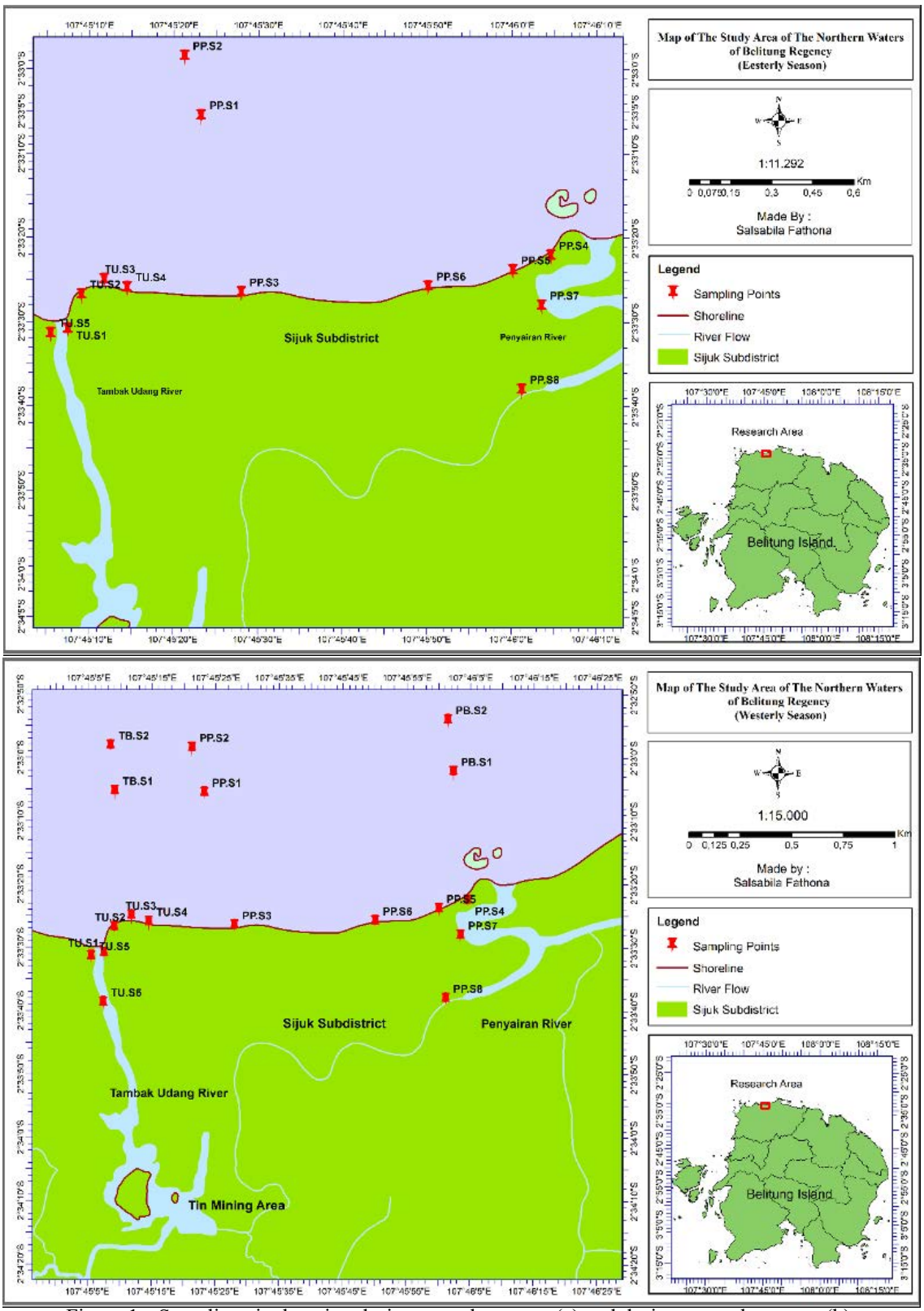

Figure 1. Sampling site location during easterly season (a) and during westerly season (b)

Table 1. Sample site during easterly season

No.	Sample Site	Description of Sample Site
1.	TU.S1	Tambak Udang estuary
2.	TU.S2	Tambak Udang estuary
3.	TU.S3	Penyairan beach close to Tambak Udang estuary
4.	TU.S4	Penyairan beach close to Tambak Udang estuary
5.	TU.S5	Tambak Udang estuary
6.	PP.S1	Offshore, north of Penyarian Beach
7.	PP.S2	Offshore, north of Penyarian Beach
8.	PP.S3	Penyairan beach
9.	PP.S4	Penyairan beach close to Penyairan estuary
10.	PP.S5	Penyairan beach close to Penyairan estuary
11.	PP.S6	Penyairan beach
12.	PP.S7	Penyairan estuary
13.	PP.S8	Penyairan estuary

Table 2. Sample site during westerly season

No.	Sample Site	Description of Sample Site
1.	TU.S1	Tambak Udang Estuary
2.	TU.S2	Tambak Udang Estuary
3.	TU.S3	Penyarian beach (near to the Tambak Udang estuary)
4.	TU.S4	Penyarian beach (near to the Tambak Udang estuary)
5.	TU.S5	Tambak Udang Estuary
6.	TU.S6	Tambak Udang Estuary
7.	PP.S1	Offshore, north of Penyarian Beach
8.	PP.S2	Offshore, north of Penyarian Beach
9.	PP.S3	Penyairan beach
10.	PP.S4	Penyarian beach (near to the Penyairan estuary)
11.	PP.S5	Penyarian beach (near to the Penyairan estuary)
12.	PP.S6	Penyairan beach
13.	PP.S7	Penyairan estuary
14.	PP.S8	Penyairan estuary
15.	PB.S1	Offshore, north of Penyarian Beach
16.	PB.S2	Offshore, north of Penyarian Beach
17.	TB.S1	Offshore, north of Penyarian Beach
18.	TB.S2	Offshore, north of Penyarian Beach

(Table 1) in the easterly season (August 2022), and sediment and water sampling was conducted at 18 stations (Table 2) in the westerly season (December 2022).

The research employs two main types of data which is primary and secondary data. Primary data, collected in August 2022 (easterly season) and December 2022 (westerly season), comprises field data from sediment samples, water samples, and oceanographic parameters. The data from the easterly season was collected by the research team from the National Research and Innovation Agency (BRIN) in August 2022. Primary data in the easterly season is sediment data which collected in-situ, and secondary data in the easterly season is current data. The data, including coastal sediments, offshore sediments, and estuary from two rivers, the Penyairan River and Tambak Udang River, were then processed and analyzed *ex-situ* at the Engineering Geology and Chemistry Laboratory at (BRIN).

The data from the westerly season were collected on December 20 and 21, 2022. The data collected from the westerly season is in-situ, such as sediment samples and water column samples, water chemistry-physical parameter data, and current data. Furthermore, the sediment sample and water column samples were processed and analyzed ex-situ at the Engineering Geology and Chemistry Laboratory at (BRIN). Data on the chemical and physical parameters of the waters were taken using the Horiba U-50 Multiparameter Water Quality Checker. The secondary data used in this study is current data that was downloaded from the website https://www.hycom.org/.

Sediment samples on the coast were collected from the bottom layer by using equipment. The boat was occupied to take the samples from Tambak Udang River, Penyairan River, and offshore by a grab sampler. Water sampling was collected by following the methods from (APHA, 2017) and Sutrisyani (2016). Water sampling was carried out using a polyethylene sample bottle with a volume of 500 mL, which had previously been cleaned with tap water and rinsed with ambient seawater. Water samples obtained were then preserved with concentrated HNO_3 with a pH < 2.

In the laboratory, sediment samples were dried, sieved, sub-sampled, and destructed to enable elemental analysis using atomic absorption spectrophotometry (AAS). Surface water samples were processed similarly, with the addition of dilution and filtration steps. During laboratory analysis, each sediment sample was divided into three sub-samples to ensure triplicate measurements for quality control. The sub-samples for AAS analysis typically weighed around 0.5000 to 0.5010 grams. Subsequently, the sample destruction process was carried out, transforming the sediment sample into a form that could be measured, enabling the analysis of its elemental content (Habibi, 2020). The sample destruction process commenced by mixing the sediment sample with a solution containing 10 mL of HF, 1 mL of HNO_3, and 1 mL of H_2SO_4. Prior to heating, the sediment sample and the solution were thoroughly mixed to achieve homogeneity. After the heating process, the sample was cooled until all vapors had dissipated. The subsequent step involved mixing the dried and cooled sample with 25 mL of concentrated HCl until homogenous. The mixture was then heated using a hot plate at a temperature of 360°C for 5 minutes and subsequently cooled until no vapor was present. The following step consisted of diluting the sediment sample with distilled water (aquabidest) and filter paper of Whatman Grade 41. During this process, the sample was filtered to remove any impurities. The dilution process was considered complete when the solution reached a volume of 100 mL within a measuring flask. For surface water samples, the preparation involved taking 50 mL of surface water and adding 1 mL of HNO_3. The mixture was then heated until the water sample was reduced to 20 mL. The shrunken sample was transferred into a 50 mL measuring flask using filter paper, and aquabidest was added to reach the flask's capacity. The sample was then shaken within the measuring flask. AAS analysis followed the calibration curve quantification method using Certipur® lead (Pb) standard solutions of varying concentrations, such as 0.08, 0.06, 0.04, 0.02, 0.1, and 0.5 ppm. After obtaining the value of Pb concentration in sediment samples from the calibration curve, calculations were then carried out to obtain the concentration of Pb in dry samples. The calculation of Pb in dry samples used the following equation.

$$Concentration\ of\ Pb\ \left(\frac{mg}{kg}\right) = \frac{X\left(\frac{mg}{l}\right) \times V(l)}{M(kg)}$$

Where:
X : Pb concentration in sample solution (mg/l)
V : Volume of sample solution (l)
M : Sample weight (kg)

The concentration of lead (Pb) and data on the physical and chemical parameters of the waters were analyzed descriptively. Data obtained from the

measurement of physical and chemical parameters of seawater and lead metal concentration data obtained from water column samples were compared with the quality standards of seawater and river water based on the Government Regulation of the Republic of Indonesia as (Indonesian State Gazette, 2021) Data on the concentration of lead (Pb) refers to the Sediment Quality Guideline (ANZECC & ARMCANZ). Furthermore, the lead (Pb) concentration data obtained from sediment and water column samples is compared between the two, as well as the easterly and westerly season sample data, which will be compared to determine which one has more concentration. The results of this comparison are then used to draw conclusions about the qualitative conditions in the northern waters of Belitung Regency.

RESULTS

Condition of the ocean current

The seawater current data in this study were sourced from the Hybrid Coordinate Ocean Model (HYCOM) for August and December 2022, representing the easterly and westerly seasons, respectively. Seasonal patterns strongly influence the seawater currents in the northwestern waters of Belitung Regency. The Quiver plot and current rose diagram (Figure 2) illustrate that during the easterly season (August), surface currents predominantly flow westward and northwestward at speeds ranging from 0.07 to 0.2 m/s. The westerly season, occurring from December to February, is characterized by winds blowing from the west, as depicted in the Quiver plot and the current rose diagram (Figure 3). During this period (December), currents primarily move eastward to southeastward with varying speeds. The daily variability of seawater current speeds ranges from 0.08 to 0.45 m/s.

The concentration of lead (Pb) in sediment and water

This study assessed Pb concentrations in sediment and water samples (Table 3). Laboratory analysis revealed that during both the easterly and westerly seasons, Pb concentrations in sediments generally remained below the threshold established by the ANZECC and ARMCANZ-based Sediment Quality Guidelines (SQG) (Table 4). During the Easterly season, the highest recorded Pb concentration in sediments was 50.09 mg/kg dry weight, with an average of 17.75 mg/kg dry weight. In the westerly season, concentrations peaked at 60.74 mg/kg dry weight, with an average of 27.32 mg/kg dry weight. In contrast, Pb concentrations in water samples from various stations during the westerly season exceeded the water quality standard set by the Minister of Environment and Forestry Regulation No. 22 of 2021. As shown in Table 5, Pb concentrations in river water reached a maximum of 0.057 mg/L, averaging 0.026 mg/L, while seawater concentrations peaked at 0.048 mg/L, with an average of 0.027 mg/L.

During the easterly season (Figure 4), Pb concentrations in the open sea reached 19.02 mg/kg dry weight, exceeding those in coastal areas, which ranged from 10.08 mg/kg to 50.09 mg/kg dry weight. In river areas, Pb concentrations varied between 10.75 mg/kg and 20.49 mg/kg dry weight. In contrast, during the westerly season (Figure 5), Pb concentrations in river sediments near the mainland were significantly higher, with levels reaching 60.74 mg/kg dry weight in the Tambak Udang River and 56.21 mg/kg dry weight in the Penyairan River. Coastal and offshore areas exhibited lower concentrations, ranging from 10.96 mg/kg to 34.15 mg/kg dry weight. Overall, Pb concentrations in sediments were consistently higher during the westerly season compared to the easterly season (Figure 6).

Laboratory test results revealed that Pb concentrations in the water column during the westerly season were detected at nearly all stations (16 out of 18), except for TU.S1 (Tambak Udang River) and TU.S3 (coastal), where Pb was undetectable. According to PP No. 22 of 2021, the threshold for Pb in seawater supporting marine biota is 0.008 mg/L, while for river water across all classes, it is 0.03 mg/L. Pb concentrations in seawater exceeded regulatory limits at 10 out of 11 stations (Figure 7). Spatial variations were observed, with one out of 11 stations showing no Pb detection. Similarly, in river water, one station exhibited undetectable Pb levels. Overall, Pb concentrations in sediment were consistently higher than those in the water column (Figure 8).

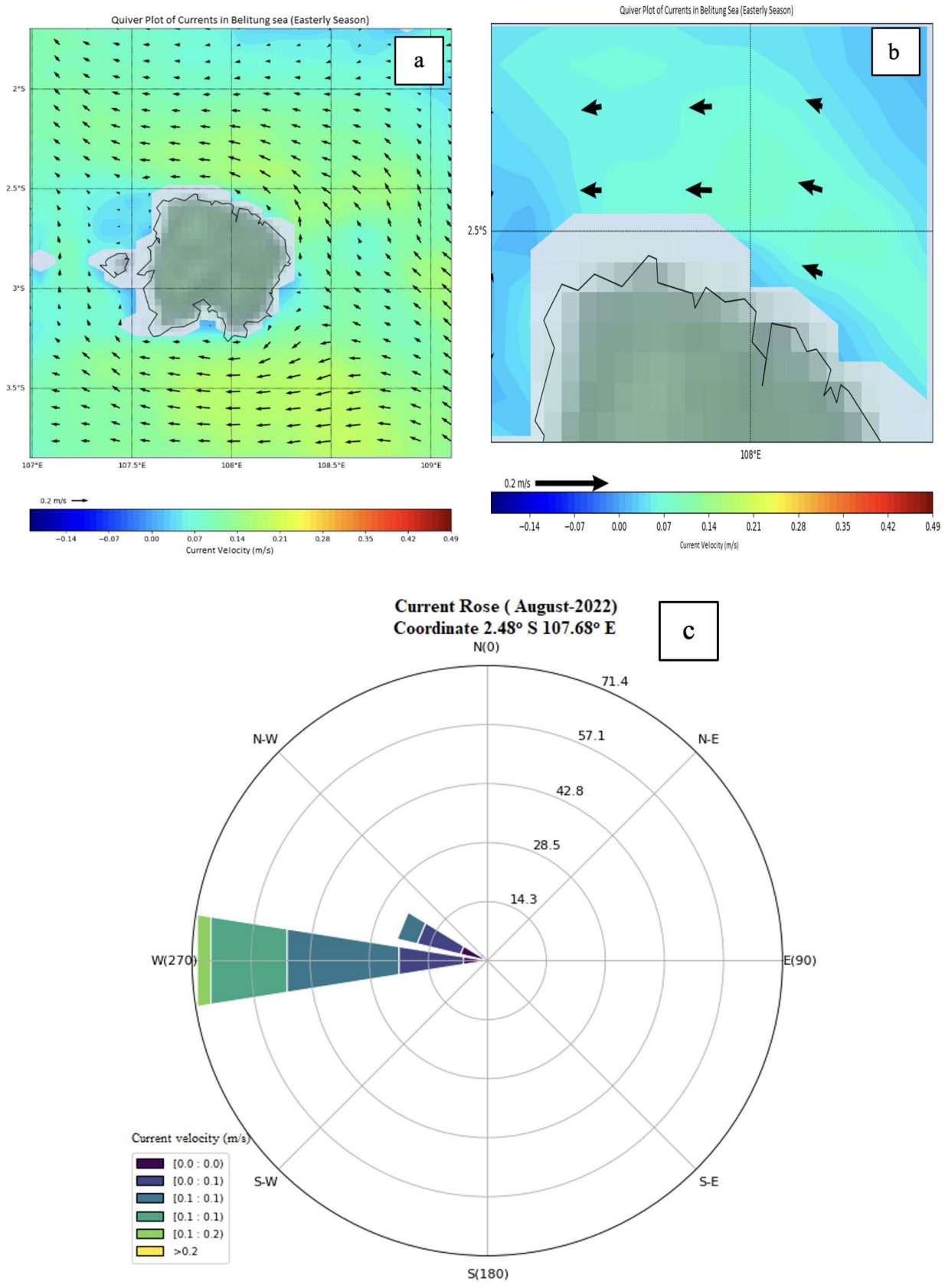

Figure 2. Ocean current at Belitung Island (easterly season) (a), ocean current in Northern of Belitung Regency (easterly season) (b), taken from HYCOM and ocean current rose at Belitung Island (August 2022) (c)

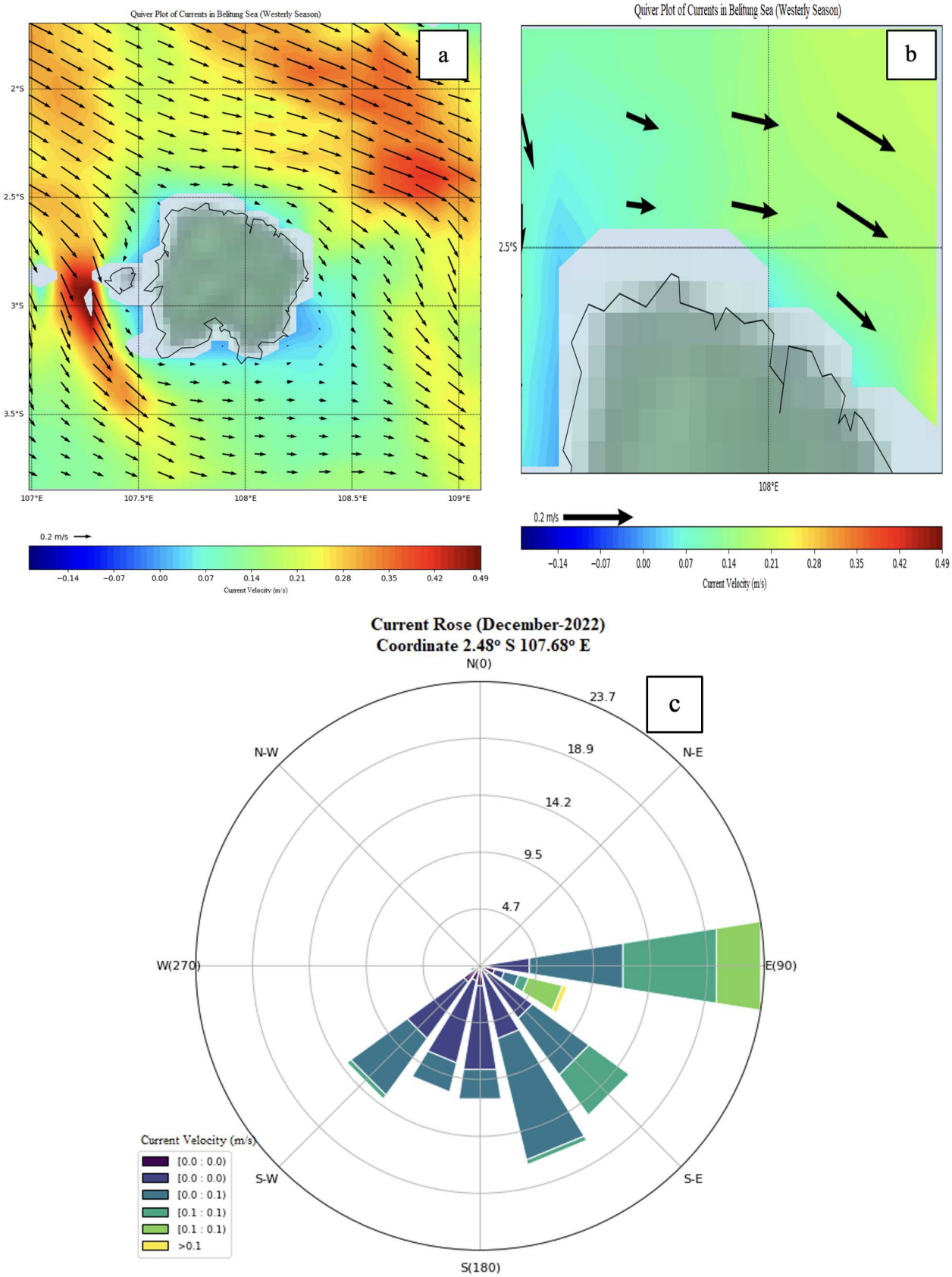

Figure 3. Ocean current at Belitung Island (westerly season) (a), ocean current in Northern of Belitung Regency (westerly season) (b), taken from HYCOM and ocean current rose at Belitung Island (August 2022) (c)

Table 3. The concentration of lead (Pb) in sediment and water during the easterly and westerly seasons.

Sample Site	Easterly Season		Westerly Season	
	Concentration of lead (sediment) (mg/kg)	Concentration of lead (sediment) (mg/kg)	Concentration of lead (river water) (mg/L)	Concentration of lead (seawater) (mg/L)
TU.S1	14.31	16.05	Nd	-
TU.S2	11.06	10.96	0.005	-
TU.S3	18.86	24.53	-	Nd
TU.S4	10.73	20.57	-	0.028
TU.S5	14.31	13.78	0.04	-

Sample Site	Easterly Season		Westerly Season	
	Concentration of lead (sediment) (mg/kg)	Concentration of lead (sediment) (mg/kg)	Concentration of lead (river water) (mg/L)	Concentration of lead (seawater) (mg/L)
TU.S6	-	60.74	0.025	-
PP.S1	20.82	30.18	-	0.037
PP.S2	50.09	18.31	-	0.025
PP.S3	10.08	23.4	-	0.019
PP.S4	10.73	28.49	0.03	-
PP.S5	19.02	21.13	-	0.025
PP.S6	14.31	29.62	-	0.028
PP.S7	15.93	37.54	0.057	-
PP.S8	20.49	56.21	0.025	-
PB.S1	-	34.15	-	0.045
PB.S2	-	21.14	-	0.028
TB.S1	-	10.96	-	0.022
TB.S2	-	34.15	-	0.048

Nd: Not detected.

Table 4. Statistics descriptive of the concentration of lead (Pb) in the sediment during easterly and westerly seasons

	Easterly Season	Westerly Season
Maximum	50.09	60.74
Minimum	10.08	10.96
Average	17.75	27.32
Sediment Quality Guideline		
ANZECC/ARMCANZ Guidelines		50

Table 5. Statistics descriptive of Pb the concentration in the sediment on westerly season

	River Water	Seawater
Maximum	0.057	0.048
Minimum	Nd	Nd
Average	0.026	0.027
PP No. 22 of 2021	0.008	0.03

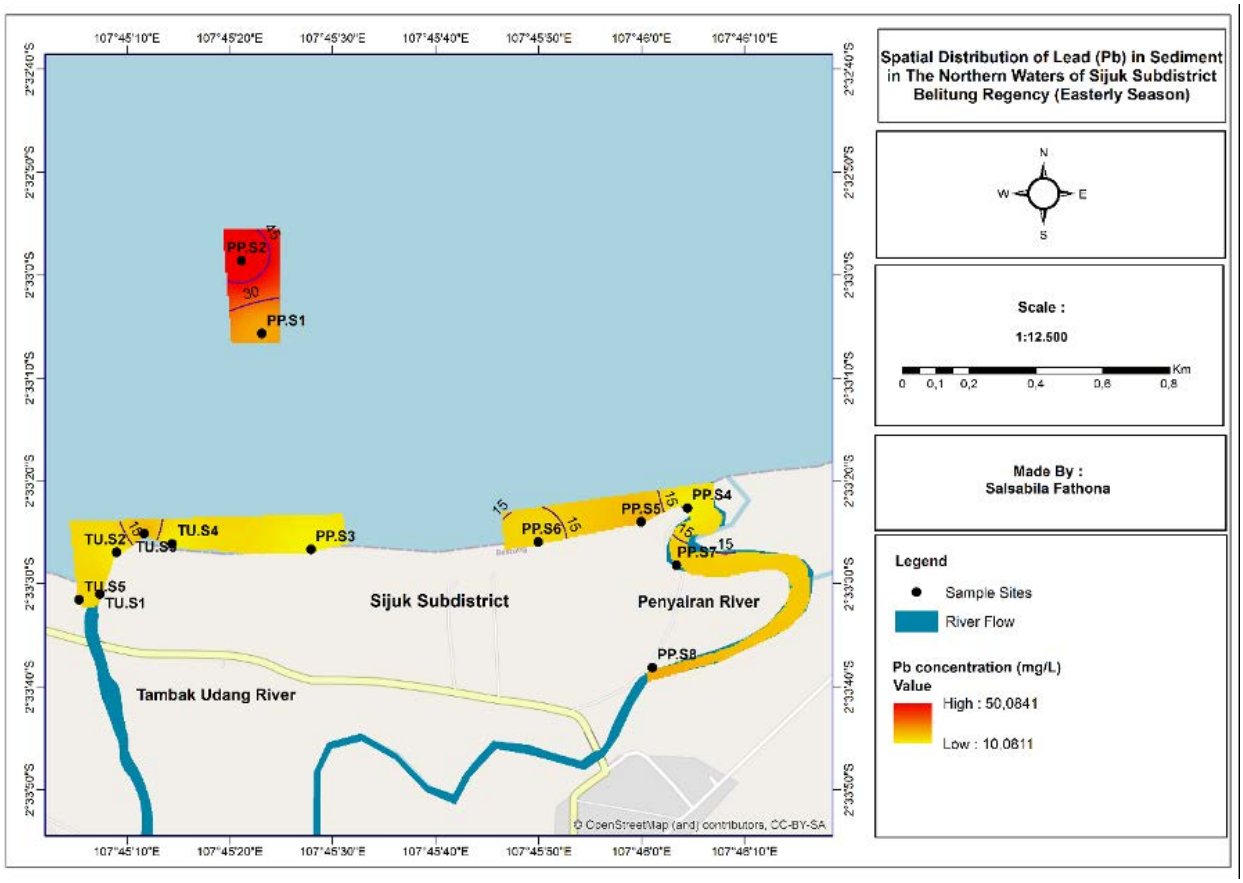

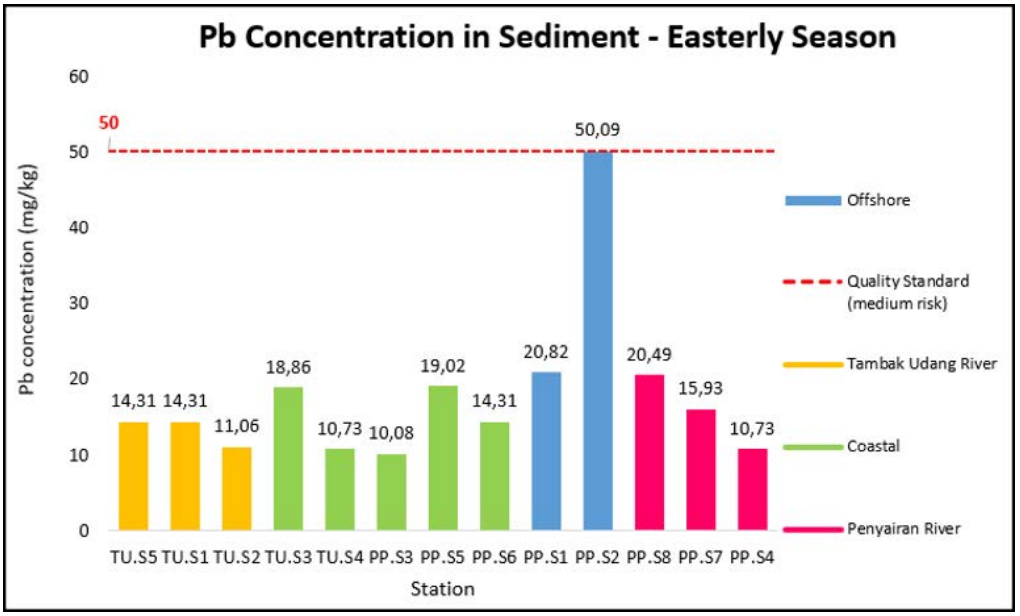

Figure 4. Spatial distribution of lead (Pb) in sediment during the easterly season (a), Lead (Pb) concentration in sediment during the easterly season at all sampling sites (b).

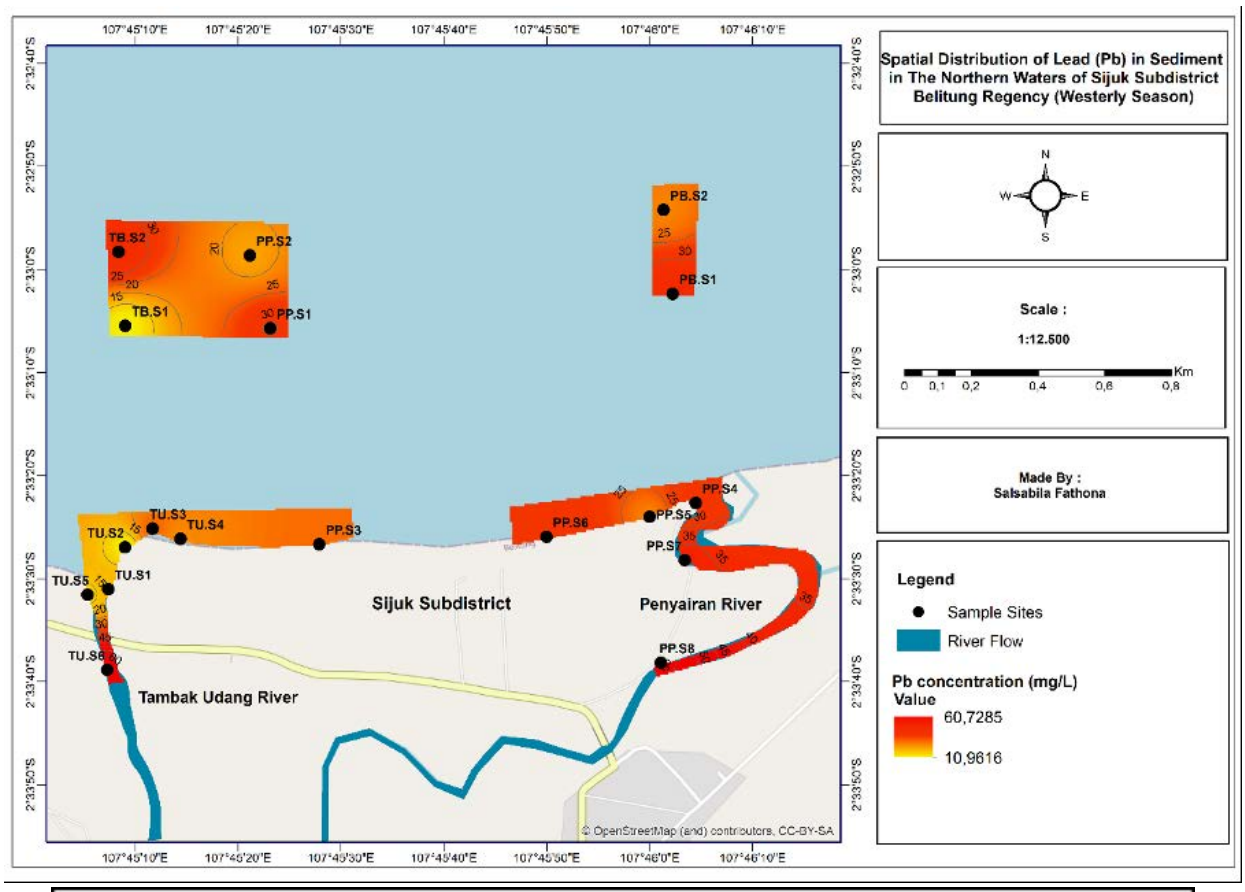

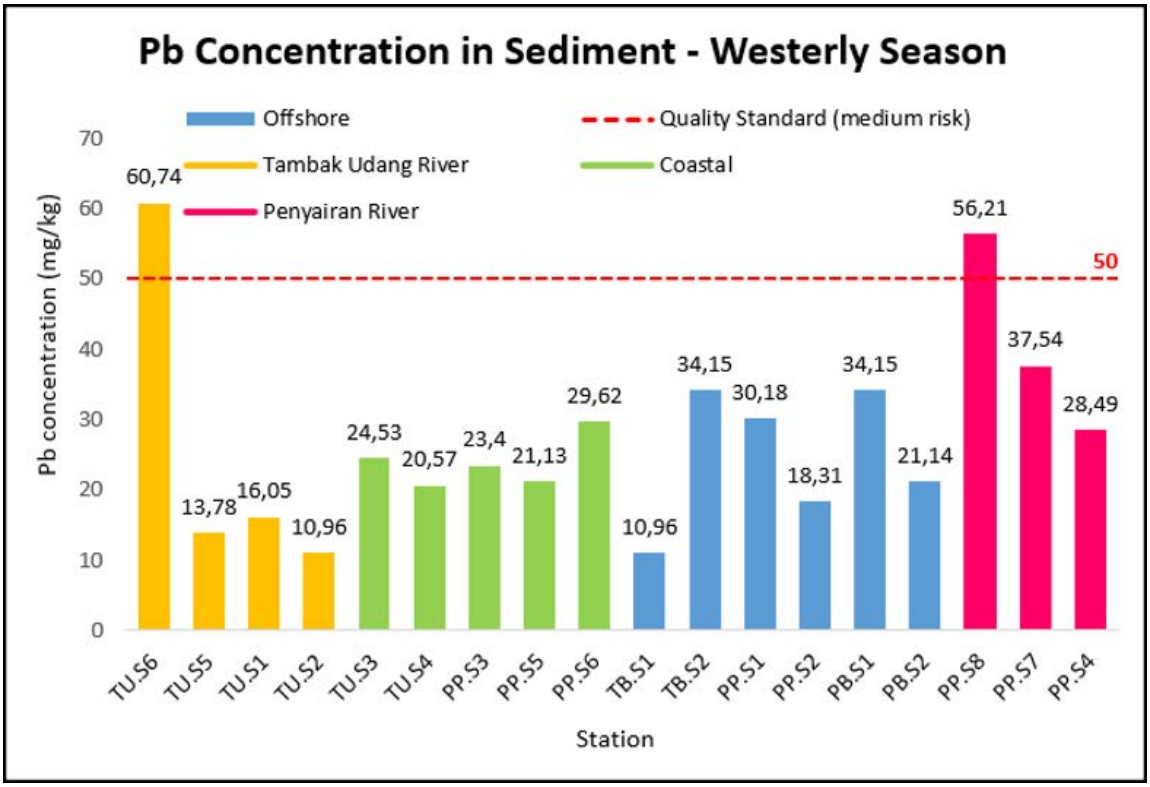

Figure 5. Spatial distribution of lead (Pb) in sediment during the westerly season (a), Lead (Pb) concentration in sediment during the westerly season at all sampling sites (b).

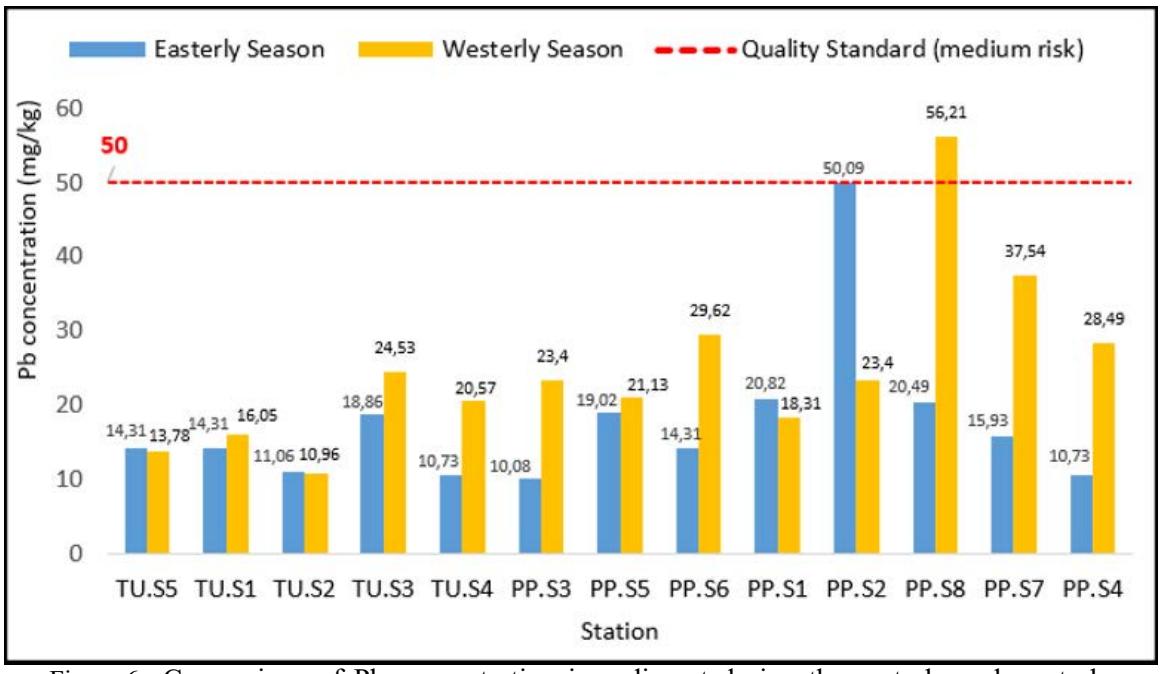

Figure 6. Comparison of Pb concentration in sediment during the easterly and westerly

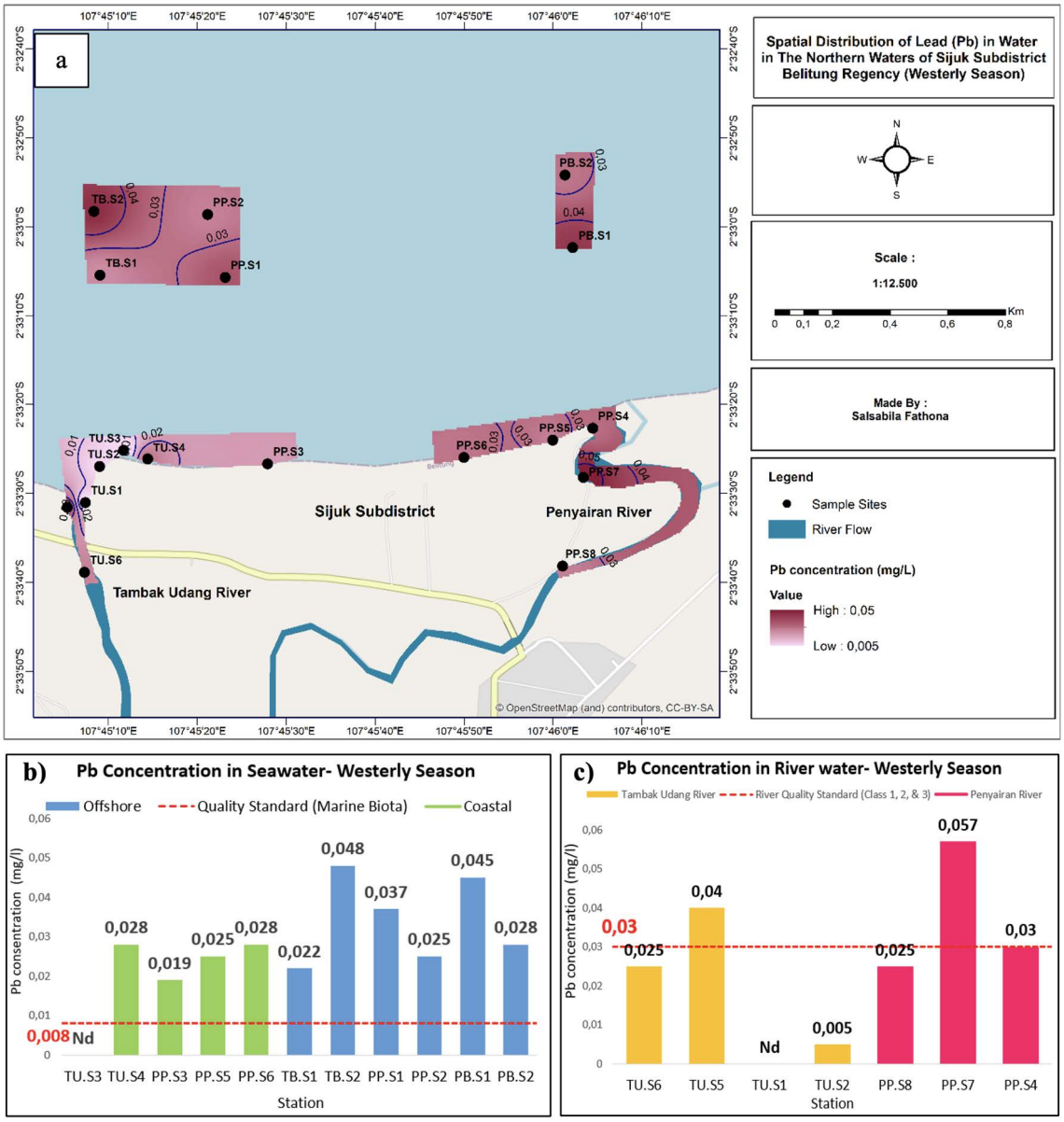

Figure 7. Spatial distribution of lead (Pb) in water during the westerly season (a), lead (Pb) concentration in seawater during the westerly season at all sampling sites (b), lead (Pb) concentration in river water during the westerly season at all sampling sites (c)

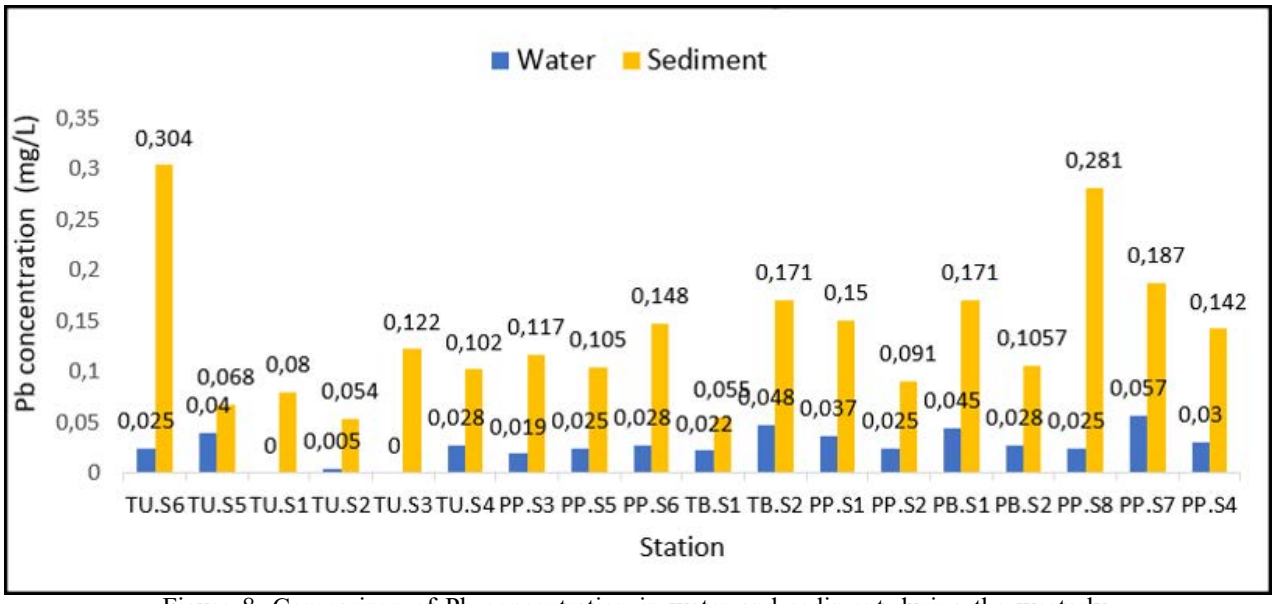

Figure 8. Comparison of Pb concentration in water and sediment during the westerly

DISCUSSIONS

This study assessed Pb concentrations in both sediments and the water column, with sampling conducted in the Penyairan River, Tambak Udang River, coastal areas, and offshore. Sediment samples were collected during both the easterly and westerly seasons, whereas water samples were obtained only during the westerly season. The absence of settlements or port activities in the study area strongly suggests that the primary source of Pb contamination originates from tin mining operations directly connected to the site.

Spatial analysis revealed that during the easterly season, Pb concentrations were higher offshore compared to coastal and river areas. This distribution pattern is likely influenced by seawater currents, which in Sijuk waters move northwestward at low speeds of 0.07 to 0.2 m/s during this season. As a result, Pb-contaminated water masses are transported away from the mainland and deposited offshore.

During the westerly season, Pb concentrations in river sediments near the mainland were higher than those in coastal and offshore areas. This distribution pattern is likely influenced by seawater currents, sediment grain size, geographical location, and tidal dynamics. In this season, currents in Sijuk waters move from east to south at higher speeds (0.08–0.45 m/s) compared to the easterly season. As a result, Pb-contaminated water masses are transported toward the mainland and deposited in river sediments.

They facilitate the movement of particles from one location to another, significantly influencing pollutant distribution. As noted by Lebreton et al. (2017), currents play a crucial role in transporting materials, including various forms of waste, across vast areas. These dynamic forces carry both solid and liquid contaminants, spreading pollution over large distances and affecting ecosystems far beyond the initial source of contamination. Geographical location also plays a crucial role in the distribution of Pb concentrations across the four regions. In Sijuk, Belitung, Pb contamination primarily originates from former tin mining sites on land, which are directly connected to the two rivers flowing into the sea. As a result, Pb accumulates in the sediments of the Tambak Udang and Penyairan Rivers, contributing to elevated concentrations in these areas.

Heavy metal concentrations in sediments are strongly influenced by sediment grain size. Finer sediments, such as clay and silt, exhibit higher heavy metal accumulation due to their larger surface area and greater cation exchange capacity, which enhances metal adsorption and retention. Zhao et al. (2023) demonstrated a significant positive correlation between heavy metal content and fine sand or clay fractions. The highest heavy metal concentrations are typically found in fine-grained sediments, including clay, silty sand, and mud, rather than in pure sand. This phenomenon is driven by electrochemical attraction forces between sediment and mineral particles, which facilitate metal adsorption. Fine-grained sediments provide a more effective binding surface for heavy metal ions compared to coarse sediments like pure sand (Zhang et al., 2014). Additionally, the offshore dispersion of Pb is influenced by tidal patterns. Belitung Waters

experience a diurnal tide, characterized by a single tide per day on average. This results in a back-and-forth water movement, which periodically transports heavy metals from coastal areas to offshore regions. The tidal-driven currents play a crucial role in redistributing contaminants, contributing to the accumulation of Pb in offshore sediments.

The seasonal variation in Pb concentration in sediments indicates significantly higher levels during the westerly season compared to the easterly season. Najamuddin (2016) reported that heavy metal concentrations tend to be lower in the dry season (easterly season) and higher in the rainy season (westerly season). This increase is primarily attributed to intensified erosion and surface runoff during the rainy season, which transports greater amounts of heavy metals into water bodies, leading to their accumulation in sediments.

Laboratory results confirm that Pb concentrations in sediments are significantly higher than in the water column. This discrepancy arises because heavy metals, including Pb, predominantly settle in sediments, making them a reliable indicator of heavy metal accumulation in aquatic environments. Upon entering marine systems, heavy metals dissolve in water before binding to organic matter and fine-grained sediments, leading to their long-term accumulation. Amin et al. (2011) noted that heavy metal concentrations in sediments tend to increase over time, depending on environmental conditions. Similarly, Bai et al. (2016) reported that heavy metals readily bind to organic matter and settle at the bottom, where they integrate with sediments. Their strong affinity for fine particles, such as clay and silt, further enhances their accumulation in benthic environments, solidifying sediments as a primary sink for these pollutants.

Moreover, Pb concentrations in both the water column and sediments are influenced by various marine water quality parameters, including temperature, salinity, pH, and dissolved oxygen (Sagala et al., 2015). This study observed variations in these parameters between river and sea stations. However, due to the limited dataset, establishing a strong correlation between Pb concentrations and these water quality parameters remains challenging. A more comprehensive dataset is necessary to substantiate these relationships with greater certainty, as suggested by findings from previous studies.

The relationship between water quality parameters and the behavior of lead (Pb) in marine environments is significantly influenced by temperature. Lower seawater temperatures enhance the adsorption of heavy metals onto particulates, facilitating their deposition onto the seabed. In contrast, higher temperatures reduce adsorption efficiency, increasing the dissolution of heavy metal compounds in the water column. This temperature-dependent mechanism underscores the dynamic mobility of heavy metals in aquatic systems, emphasizing temperature as a critical water quality parameter (Wang et al., 2011). Additionally, heavy metals are more prevalent in low-salinity areas, as lower salinity conditions reduce the ability of metals to precipitate or bind to particulates, keeping them in suspension or solution. In contrast, higher salinity levels promote metal precipitation and adsorption onto sediments, effectively removing them from the water column (Connel & Miller, 1995, as cited in Ali et al., 2010).

The solubility of heavy metals in water is strongly influenced by dissolved oxygen (DO) levels. Under low-oxygen or anoxic conditions, the solubility of heavy metals decreases, leading to their precipitation and accumulation in sediments. Metals such as Zinc (Zn), Chromium (Cr), Cadmium (Cd), Lead (Pb), Mercury (Hg), and Silver (Ag) exhibit reduced solubility in anoxic environments, resulting in their deposition rather than remaining in the water column (Wang et al., 2015). Additionally, pH and heavy metal solubility have an inverse relationship. Heavy metals dissolve more readily in low-pH conditions, increasing their concentration in the water column, whereas higher pH levels promote their precipitation and adsorption onto sediments (Sagala et al., 2015).

CONCLUSSIONS

This study on Pb content in the northern waters of Belitung Regency yielded the following key findings. Pb concentrations in sediments ranged from 10.08 to 50.08 mg/kg (dry weight) during the easterly season and from 10.96 to 60.72 mg/kg (dry weight) during the westerly season. In the water column, Pb concentrations during the westerly season were approximately 0–0.05 mg/L. The distribution of Pb in sediments varied by season. In the easterly season, Pb tended to disperse offshore, whereas in the westerly season, it accumulated in river sediments. This pattern was influenced by seasonal flow dynamics, geographical location, and sediment grain size. Pb concentrations in sediments were generally higher in the westerly season than in the easterly season. This increase is attributed to intensified

erosion and runoff during the rainy season, leading to greater heavy metal deposition in sediments. These findings provide valuable insights into the distribution, accumulation, and transport of heavy metals in aquatic environments. They also highlight the importance of continuous monitoring and effective coastal management strategies to mitigate heavy metal contamination.

ACKNOWLEDGEMENTS

The authors would like to express their gratitude to the Oceanography Study Program for providing opportunities and platforms in exploring oceanography fieldwork and facilitating research tools. In addition, the authors also want to express their sincere appreciation to the National Research and Innovation Agency (BRIN) for research guidance services and laboratory services.

REFERENCES

Ali, H., Khan, E., and Sajad, M.A., 2010. Phytoremediation of Heavy Metals Concepts and Applications. *Chemosphere,* 91(7): 869–881.

Amin, B.E., Afriyani, M., and Saputra, A., 2011. Distribusi Spasial Logam Pb dan Cu pada Sedimen dan Air Laut Permukaan di Perairan Tanjung Buton Kabupaten Siak Provinsi Riau. *Jurnal Teknobiologi*, 2011(2): 1–8.

APHA (American Public Health Association), 2017. Standard Methods for the Examination of Water and Wastewater. 23rd ed. Washington, DC: APHA, AWWA, WEF.

Bai, Jihong, Xiao, R., Zhang, K., and Gao, H., 2016. Heavy Metal Concentrations in Riverine and Coastal Sediments. *Environmental Science and Pollution Research*, 23(10): 9485-9498.

Duffus, John H., 2002. Heavy Metals A Meaningless Term?. *Pure and Applied Chemistry*, 74(5): 793-807.

DeForest, D., Brix, K., and Adams, W., 2007. Assessing metal bioaccumulation in aquatic environments: The inverse relationship between bioaccumulation factors, trophic transfer factors and exposure concentration. *Aquat Toxicol*, 84:236–246.

Demirak, A., Yilmaz, F., Tuna, A.L., Ozdemir, N., 2006. Heavy Metals in Water, Sediment and Tissues of Leuciscus Cephalus from a Stream in Southwestern Turkey. *Chemosphere*, 63:1451–1458.

Ghrefat H., and Yusuf, N., 2006. Assessing Mn, Fe, Cu, Zn, and Cd Pollution in Bottom Sediments of Wadi Al-Arab Dam Jordan. *Chemosphere*, 65:2114–2121.

Guo, W., He, M., Yang, Z., Lin, C., Quan, X., and Wang, H., 2020. The Role of Sediment-Water Exchange in the Fate of Heavy Metals in Aquatic Systems. *Environmental Pollution*, 266, 115–127.

Habibi, Y., 2020. Validasi Metoda Destruksi Basah dan Destruksi Kering pada Penentuan Logam Timbal (Pb) dan Kadmium (Cd) dalam Tanaman Rumput. *Integrated Lab Journal*, 8(1): 25– 31.

Herman, D. Z., 2006. Tinjauan Terhadap Tailing Mengandung Unsur Pencemar Arsen (As), Merkuri (Hg), Timbal (Pb), dan Kadmium (Cd) dari Sisa Pengolahan Bijih Logam. *Indonesian Journal on Geoscience*, 1(1): 31-36.

Indonesian State Gazette, 2021. Government Regulation no. 22 of 2021 on Environmental Protection, Organisation and Management. Republic of Indonesia.

Khaled, A., Nemr, A.E., Sikaily, A.E., 2006. An Assessment of Heavy Metal Contamination in Surface Sediments of the Suez Gulf Using Geoaccumulation Indexes and Statistical Analysis, *Chem Ecol*, 22:239–252.

Lebreton, Laurent, Zwet, J.V.D., Damsteeg, J.W., Slat, B., Andrady, A., and Reisser, J., 2017. River Plastic Emissions to the World's Oceans. *Nature Communications*, 8(1): 15611.

Najamuddin, T. Prartono, H.S., Sanusi, and Nurjaya, I.W., 2016. Distribusi dan perilaku Pb dan Zn terlarut dan partikulat di perairan estuaria Jeneberang, Makassar, *Jurnal Ilmu dan Teknologi Kelautan Tropis,* 8(1):11-28.

Naser, H. A., 2013, Assessment and management of heavy metal pollution in the marine environment of the Arabian Gulf: A review, *Mar Pollut Bull*, 72:6–13.

Ozkan, E. Y., and Buyukisik, B., 2012. Geochemical and Statistical Approach for Assessing Heavy Metal Accumulation in the Southern Black Sea Sediments, *Ekoloji*, 21(83):11–24.

Sagala, S.L., Bramawanto, R., Kuswardani, A.R., and Pranowo, W.S., 2015. Distribution Of Heavy Metals in Natuna Coastal Waters. *Jurnal Ilmu Dan Teknologi Kelautan Tropis,* 6: 297-310.

Shazili, N.A.M., Yunus, K., Ahmad, A., Abdullah, N., and Rashid, M.K.A., 2006. Heavy Metal Pollution Status in the Malaysian Aquatic Environment. *Aquatic Ecosystem Health & Management*, 9(2), 137–145.

Singh, K.P., Mohan, D., Singh, V.K., and Malik, A., 2006. Studies on Distribution and Fractionation of Heavy Metals in Gomti River Sediments-a Tributary of The Ganges. *J Hydrol,* 312:14–27.

Soegianto, A., 2019. Pencemaran Logam Berat di Perairan dan Dampaknya terhadap Biota Laut. *Jurnal Ilmu dan Teknologi Kelautan Tropis*, 11(2): 451–462.

Sutrisyani, S., 2016. Metode Pengambilan dan Pengawetan Sampel Air Laut. *Buletin Teknik Litkayasa Akuakultur*, 1(1): 1-8.

Tchounwou, Paul B., Clement G., Yedjou, Anita K., Patlolla, and Dwayne J.S., 2012. Heavy Metals Toxicity and the Environment. *EXS,* 101: 133–164.

Wang, Ning, Chen, X., Sheng, Y., and Liu, G., 2015. Effects of Dissolved Oxygen on the Solubility and Mobility of Heavy Metals in Aquatic System. *Journal of Environmental Sciences*, 34: 1-10.

Wang, W. X., and Rainbow, P.S., 2008. Comparative Approaches to Understand Metal Bioaccumulation in Aquatic Animals, *Comp Biochem Physiol Part C Toxicol Pharmacol,* 148:315–323.

Wang, Shaofeng, Yan, Y., and Pan, X., 2011. Effect of Temperature on the Adsorption and Desorption of Heavy Metals in Aquatic Environments. *Environmental Sciences and Pollution Research*, 18(6): 908-916.

Zhang, Chuanbo, Yang, Z., Li, Z., Wang, Y., and Zeng, L., 2014. Distribution and Enrichment of Heavy Metals in Sediment of Xiangjiang River, China. *Environmental Earth Sciences*, 71(9): 3949-3957.

Zhao, Y., Wang, L., Li, Y., and Zhang, J., 2023. Analysis of Heavy Metals in Sediments with Different Particle Sizes. *Scientific Reports,* 13: Artikel 71502.

IMPACT OF SIGNIFICANT WAVE HEIGHT, WIND SPEED, AND PRECIPITATION VARIABILITY ON SHIPPING SAFETY IN INDONESIAN ARCHIPELAGIC SEA LANES

DAMPAK VARIABILITAS KETINGGIAN GELOMBANG SIGNIFIKAN, KECEPATAN ANGIN DAN CURAH HUJAN TERHADAP KESELAMATAN PELAYARAN DI ALUR LAUT KEPULAUAN INDONESIA

Azkal Fathurohman[1,2], Gandhi Napitupulu[1*], Ghina Fujiawati[2,3], Moses Napitupulu[4]

[1]Oceanography Study Program, Bandung Institute of Technology

[2]Bhumi Warih Geohydromatics, Bandung, Indonesia

[3]Meteorology Study Program, Bandung Institute of Technology

[4]Naval Architecture and Marine Engineering Department, University of Indonesia

*Corresponding author: gandhinapitupulu88@gmail.com

(Received 31 July 2024; in revised from 19 August 2024 accepted 02 July 2025)

DOI : 10.32693/bomg.40.1.2025.895

ABSTRACT: Unexpected and unpredictable extreme weather poses significant risks to maritime activities, particularly in Indonesian waters and the Indonesian Archipelagic Sea Lanes, known as ALKI, which have been internationally recognized for shipping and aviation since 1985. This study assesses these risks by analyzing patterns of wave height, wind speed, and rainfall along ALKI to improve shipping safety and mitigate accident risks. Data from the European Centre for Medium-Range Weather Forecasts (ECMWF) ERA5 for the period 1993 to 2023 and Global Precipitation Measurement (GPM) for 2001 to 2020 were processed using descriptive statistics and Empirical Orthogonal Function (EOF) methods. The results reveal high waves (1-2.5 m) and strong winds at Beaufort scale 4 prevailing in northern Indonesian waters from December to February and southern waters from June to August. Higher rainfall (350-600 mm) occurs in the northern region from September to November and in the southern from December to February. Extreme waves (90^{th} percentile) reach up to 3 m in open ocean areas such as the Natuna Sea, western Sumatra, southern Java, the Maluku Sea, and northern Papua Sea. Extreme winds are observed over open ocean areas, with slight spatial shifts, as seen in the Arafura Sea (9-10 m/s). Extreme rainfall (250-350 mm) is concentrated in the northwestern region. EOF analysis identifies global climate phenomena and regional oceanographic dynamics as the primary drivers of significant wave height variability. Improved understanding of weather variability can enhance navigation safety along the ALKI routes and inform more effective regulation, law enforcement, and monitoring.

Keywords: Indonesian archipelagic sea lanes, significant wave height, wind speed, rainfall, shipping safety

ABSTRAK: *Cuaca ekstrem yang tidak terduga dan tidak terprediksi berisiko besar terhadap aktivitas maritim, terutama di perairan Indonesia dan Alur Laut Kepulauan Indonesia (ALKI) yang telah diakui secara internasional untuk pelayaran dan penerbangan sejak 1985. Penelitian ini dilakukan untuk memahami penyebab risiko tersebut dengan mengkaji pola tinggi gelombang, kecepatan angin, dan curah hujan di ALKI dalam rangka meningkatkan keselamatan pelayaran dan mengurangi kecelakaan. Analisis dilakukan dengan menggunakan statistik deskriptif dan Empirical Orthogonal Function (EOF) terhadap data European Center for Medium-Range Weather Forecasts (ECMWF) ERA5 periode 1993-2023 dan data Global Precipitation Measurement (GPM) tahun 2001-2020. Hasil analisis menunjukkan gelombang tinggi (1–2,5 m)*

dan angin kencang pada skala Beaufort 4 dominan di perairan utara Indonesia pada Desember hingga Februari dan perairan selatan pada Juni hingga Agustus. Curah hujan yang lebih tinggi (350–600 mm) terjadi di wilayah utara pada September hingga November dan di wilayah selatan pada Desember hingga Februari. Gelombang ekstrem (persentil ke-90) dapat mencapai hingga 3 m di perairan laut lepas seperti Laut Natuna, barat Sumatra, selatan Jawa, Laut Maluku, dan Laut Papua bagian utara. Angin ekstrem teramati di area laut lepas dengan sedikit pergeseran spasial, seperti di Laut Arafura (9–10 m/detik). Curah hujan ekstrem (250–350 mm) terkonsentrasi di wilayah barat laut. Analisis EOF mengidentifikasi fenomena iklim global dan dinamika oseanografi regional sebagai faktor utama yang memengaruhi variabilitas tinggi gelombang signifikan. Pemahaman yang lebih baik tentang variabilitas cuaca dapat meningkatkan keselamatan navigasi di sepanjang jalur ALKI serta mendukung regulasi, penegakan hukum, dan pengawasan yang lebih efektif.

Kata Kunci: *Alur Laut Kepulauan Indonesia, tinggi gelombang signifikan, kecepatan angin, curah hujan, keselamatan pelayaran*

INTRODUCTION

Indonesia is an archipelagic country with an extensive maritime area. Its strategic geographic location between two continents and two oceans brings significant political, economic, and security value to Indonesia and is also recognized by other countries (Hutagalung, 2017). This position allows Indonesia's maritime territory to function as an international shipping corridor. To regulate this, the Indonesian government enacted Law No. 17 of 1985, which ratified the United Nations Convention on the Law of the Sea (UNCLOS) of 1982 and established a consensus dividing Indonesia's waters into three designated routes known as the Indonesian Archipelagic Sea Lanes (ALKI). The ALKI routes are highly strategic for Indonesia, as international vessels and aircraft can pass through them continuously and efficiently without obstruction (Batara, 2023; Napitupulu et al., 2022a). This creates both opportunities and responsibilities for the national economy to grow in areas such as shipping, navigation, marine industries, and trade (Nainggolan, 2016; Prasetyo et al., 2020).

According to Law No. 31 of 2021 on the Implementation of Shipping, shipping is defined as an integrated system of water transportation, port operations, safety and security, and marine environmental protection. Indonesian-flagged vessels permitted to operate internationally include passenger ships, cargo ships with a gross tonnage of 500 GT or more, and mobile offshore drilling units. In addition, the law also regulates the types and functions of ships that may be used in both national and international shipping (Apriyanto et al., 2019). Ship categories authorized for operation include passenger ships, cargo ships, mobile offshore drilling units, fishing vessels, research vessels, and naval ships (Monika et al., 2022; Xing & Zhu, 2021).

The shipping and marine industries represent a potential strength for Indonesia's development as a maritime nation (Batara, 2023; Prasetyo et al., 2020). However, one aspect that needs to be cautious considered in shipping is extreme and unpredictable weather conditions. Such conditions can endanger crew and passenger safety, damage ships and even cause casualties. The International Convention for the Safety of Life at Sea (SOLAS) serves as the main regulation of international shipping safety, including provisions for dealing with extreme weather and planning safe routes. SOLAS provides guidance for national regulations, institutions, and shipping companies to collectively ensure maritime safety. In Indonesia, coordination among agencies such as the Meteorology, Climatology and Geophysics Agency (BMKG) and port authorities is essential for providing accurate and timely information, including weather observation, early warning, shipping routes, and vessel positioning. Furthermore, Law No. 17 of 2008 on shipping and the Minister of Transportation Regulation No. 20 of 2015 on shipping safety standards require shipping companies to plan safe routes by considering weather conditions, sea traffic, and accident-prone areas. According to the National Search and Rescue Agency (*Badan Nasional Pencarian dan Pertolongan*, BASARNAS) statistics for 2022, there were 823 reported maritime accidents resulting in injuries, fatalities, and missing persons, affecting a total of 6510 individuals. Based on investigations by the National Transportation Safety Committee (*Komisi Nasional Keselamatan Transportasi*, KNKT), these accidents were caused by various factors, including fires, engine explosions, collisions, listing and sinking of vessels, and capsizing. Among these, adverse weather conditions remain a significant contributing factor.

Based on accident reports published by the KNKT, several severe maritime incidents have been documented and analyzed. The first involved the cargo vessel Multi Prima I, which sank on November 22, 2018, in the Kapoposang Bali–Mataram waters, East Nusa Tenggara. The report noted wind speeds of 5–8 m/s and wave heights reaching 4 m at the time of the incident. Similar wind conditions were observed in January in the Flores Sea, when another cargo vessel, Itanini, capsized due to extreme winds and waves estimated at 2.5–3 m in height. On December 29, 2016, the passenger ship Karamando sank south of Jailolo Port, North Maluku, amid high waves ranging from 4–5 m. Another incident involved MV Marina Bari 2B, which rolled over and sank after being struck by 5 m waves; BMKG reported wind speeds there reaching up to 23 m/s. Most of these incidents were also accompanied by light to heavy rainfall.

Weather and climate phenomena can change significantly at any time due to various factors, such as storms, tropical cyclones, earthquakes, tsunamis, and global warming, which contributes to climate change and sea level rise (Akbar et al., 2024; Napitupulu, 2025; Nurdjaman et al., 2023). These changes can disrupt typical weather patterns in specific regions and may negatively affect certain communities and human activities (Nagi et al., 2023; Ningsih et al., 2023). Climate change, in particular, can have adverse impacts on maritime transport by altering shipping routes, increasing hazards and the risk of damage to maritime infrastructure, reducing the efficiency of transport operations, and raising the frequency of maritime accidents (Izaguirre et al., 2021; Monios & Wilmsmeier, 2020; Napitupulu et al., 2025).

The wind patterns over Indonesia are primarily influenced by the monsoon cycle (Bayong Tjasyono et al., 2008; Napitupulu, 2024). This cycle is driven by the apparent position of the sun relative to the Earth's latitude. Generally, from June to August, the tilt of the Earth results in greater solar exposure over the northern hemisphere, corresponding to summer conditions (Napitupulu et al., 2022b). Meanwhile, it is winter in the southern hemisphere. During this period, winds predominantly blow from the southern hemisphere (characterized by colder temperatures and higher pressure) toward the northern hemisphere (warmer, lower pressure). This phase is referred to as the Australian Monsoon in Indonesia, as the prevailing winds originate from Australia. In contrast, from December to February, the apparent position of the sun shifts toward the southern hemisphere, resulting in summer there and winter in the northern hemisphere (Napitupulu et al., 2022c). Consequently, winds primarily blow from Asia (cold, high pressure) toward Australia (warm, low pressure), a phase known as the Asian Monsoon.

Waves are primarily generated by wind forcing (Kara, 2016; Radjawane et al., 2023). This process disturbs the water's surface tension, resulting in variations in water level. Wave conditions can differ considerably depending on the prevailing wind systems (Ningsih et al., 2023). Interactions between the atmosphere and ocean, particularly between wind and waves, directly influence maritime activities such as fisheries, shipping, marine research, and transportation.

The Indonesian region is characterized by strong convective activity, which leads to highly variable rainfall patterns. Indonesian waters serve as one of the world's most significant convection centers, playing a critical role in the climate system of the equatorial region and acting as an indicator of shifts in climate variability (Yamanaka et al., 2018). Rainfall variability in Indonesia is influenced by several factors, including the Asia–Australia monsoon, the Intertropical Convergence Zone (ITCZ), the El Nino–Southern Oscillation (ENSO), and topographic effects. Indonesian rainfall patterns are generally classified into three types: monsoonal, equatorial, and local patterns (Aldrian & Susanto, 2003).

The monsoonal pattern features peak rainfall during December, January, and February (DJF). Regions that exhibit this pattern include southern Sumatra, central and southern Kalimantan, Java, Bali, Nusa Tenggara, and parts of Papua. The equatorial pattern is characterized by two rainfall peaks, typically around March and September during the equinoxes, and is generally observed in northern Sumatra and northern Kalimantan. In contrast, the local pattern shows peak rainfall during June, July, and August (JJA), which is opposite to the monsoonal pattern. This local pattern is typically found in Maluku, Sulawesi, and parts of Papua. Accordingly, this study aims to analyze weather patterns, including wind, wave, and rainfall variability, along ALKI-I, ALKI-II, and ALKI-III to inform safer shipping schedule planning.

METHODS

Three routes of the Indonesian Archipelagic Sea Lanes (Alur Laut Kepulauan Indonesia, ALKI) were selected as the areas of interest (Figure 1). From

north to south, these comprise ALKI-I, ALKI-II, and ALKI-III. ALKI-I includes the Malacca Strait, Natuna Sea, Karimata Strait, Java Sea, and Sunda Strait. ALKI-II covers the Celebes Sea, Makassar Strait, Flores Sea, and Lombok Strait. ALKI-III encompasses the Maluku Sea, Seram Sea, and Banda Sea, and is divided into three sub-routes: (1) ALKI-III A, from the Banda Sea through the Ombai Strait into the Sawu Sea and exiting to the Indian Ocean; (2) ALKI-III B, from the Banda Sea through the Leti Strait into the Timor Sea; and (3) ALKI-III C, extending eastward from the Banda Sea to the Arafura Sea.

This study used secondary data consisting of significant wave height (combined wind waves and swell) and 10 m u-component and v-component wind data from the European Centre for Medium-Range Weather Forecasts (ECMWF) ERA5 reanalysis dataset, with 6-hourly intervals. The ERA5 dataset covers 30 years (1993–2023) for the Indonesian region, spanning 7.5° N to 13.0° S in latitude and 96.0° E to 134.5° E in longitude. In addition, daily rainfall data were obtained from the Global Precipitation Measurement (GPM) dataset, covering 20 years (2001–2020) and spanning 15.0° S to 10.0° N in latitude and 90.0° E to 149.0° E in longitude.

The significant wave height parameter represents the average height of the highest one-third of surface ocean or sea waves generated by wind and swell (Yamanaka et al., 2018). It measures the vertical distance between the wave crest and trough (Napitupulu et al., 2021). The ocean surface wave field consists of a combination of waves with different heights, wavelengths, and directions, known as the two-dimensional wave spectrum (Suprijo et al., 2024). This spectrum can be decomposed into wind-sea waves, which are directly driven by local winds, and swell, which consists of waves generated by winds at distant locations and times (Radjawane et al., 2024). Significant wave height is commonly used to describe sea state and swell conditions. For example, engineers use this parameter to estimate loads on offshore structures,

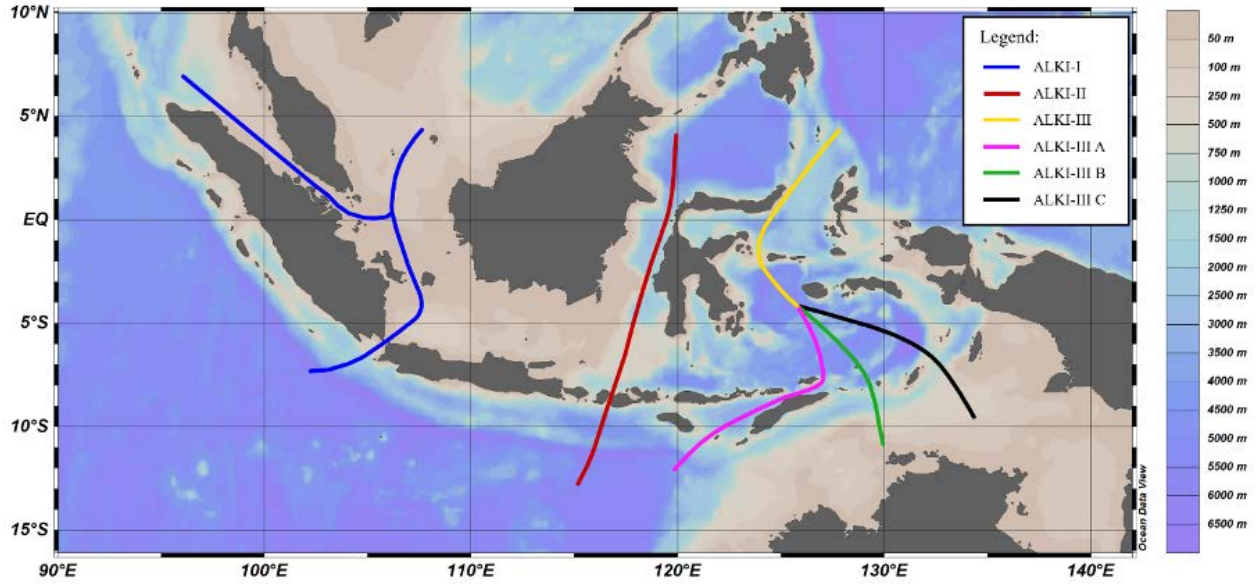

Figure 1. Indonesian Archipelago Sea Lanes (ALKI) routes.

Table 1. Classification of wave height categories in Indonesian waters (BMKG, 2024).

No	Description	Wave height range (m)
1	Calm	0.10 – 0.50
2	Low	0.50 – 1.25
3	Moderate	1.25 – 2.50
4	High	2.50 – 4.00
5	Very High	4.00 – 6.00
6	Extreme	6.00 – 9.00
7	Very Extreme	9.00 – 14.00

Table 2. Beaufort scale classification (Royal Meteorological Society, 2024).
*) These values refer to the well-developed wind waves of the open sea

Beaufort wind scale	Wind descriptive terms	Limits of wind speed (m/s)	Sea state	Sea descriptive terms	Probable wave height (m)*
0	Calm	<1	0	Calm (glassy)	-
1	Light air	1-2	1	Calm (rippled)	0.1
2	Light breeze	2-3	2	Smooth (wavelets)	0.2
3	Gentle breeze	4-5	3	Slight	0.6
4	Moderate breeze	6-8	3-4	Slight – Moderate	1.0
5	Fresh breeze	9-11	4	Moderate	2.0
6	Strong breeze	11-14	5	Rough	3.0
7	Near gale	14-17	5-6	Rough – Very rough	4.0
8	Gale	17-21	6-7	Very rough – High	5.5
9	Strong gale	21-24	7	High	7.0
10	Storm	25-28	8	Very High	9.0
11	Violent storm	29-32	8	Very High	11.5
12	Hurricane	>33	9	Phenomenal	>14

Table 3. Rainfall intensity classification (BMKG, 2024)

No	Description	Rainfall intensity (mm/day)
1	Cloudy	0 – 0.5
2	Light rain	0.6 - 20
3	Moderate rain	21 - 50
4	Heavy rain	51 - 100
5	Very heavy rain	101 - 150
6	Extreme	> 150

such as oil platforms, or for coastal engineering applications (Abdullah et al., 2022).

According to the National Agency of Meteorology, Climatology, and Geophysics (BMKG), wave height classifications are shown in Table 1. The Beaufort scale (Table 2) is also used, as it provides a standard basis for estimating wind force at sea (Kara, 2016). As illustrated by the cases described earlier, extreme waves in Indonesian waters can be categorized as high (2.5–4 m) or very high (4–6 m), excluding tsunami events. Wind conditions in these events typically reached the 4th to 5th level on the Beaufort scale, while in one extreme case, gale-force winds corresponding to level 8 were observed. In addition, rainfall intensity classifications defined by BMKG are presented in Table 3.

The collected data were first summarized using descriptive statistics and compositely visualized in monthly averaged spatial maps. The 90th percentile was then calculated to identify extreme values of wave height, wind speed, and rainfall, enabling the identification of potential extreme events within the dataset. Furthermore, Empirical Orthogonal Function (EOF) analysis was applied to examine the climate patterns influencing wave height variability along each ALKI route. Each mode derived from the EOF represents an independent spatial pattern (eigenvector), and its associated variance is quantified by an eigenvalue. This analysis helps to identify the dominant modes driving wave height variability in the study area.

RESULTS AND DISCUSSIONS

Monthly Variations of Significant Wave Height, Sea Surface Wind, and Precipitation

Figure 2 shows the monthly distribution of significant wave heights (Hs) across Indonesian waters. Overall, the seas inside the archipelago tend to be relatively calmer compared to offshore areas. In

the northern part of ALKI-I, particularly the Natuna Sea, moderate waves ranging from 1.5 to 2.5 m are observed between November and February, driven by swells propagating from the South China Sea. Wave heights typically peak in December and January, reaching up to 2.5 m. At the mouth of the Malacca Strait, wave conditions are influenced by the Indian Ocean. Higher waves generally occur from April to October, coinciding with the Australian Monsoon, when winds form cyclonic patterns along the western coast of Sumatra (Kartadikaria et al., 2024). The peak of the Australian Monsoon, between June and August, results in significant wave heights of around 1–2 m. In contrast, the inner Malacca Strait remains considerably calmer because wave propagation is limited by Sumatra and western Malaysia. A similar low-wave pattern appears in the Karimata Strait, although slightly higher due to exposure to swells from the Natuna Sea and South China Sea, with waves reaching 1–1.5 m during December to February. In the Java Sea, waves propagate in January with heights around 1 m. Further south, towards the Sunda Strait, the waters open to the Indian Ocean. During the Asian Monsoon (November to March), wave heights reach around 2 m, while in the Australian Monsoon period, waves can exceed 3 m. These findings are consistent with previous studies. Wicaksana et al. (2015) and Anggara et al. (2018) reported that significant wave heights in the Natuna Sea, Karimata Strait, and Java Sea during the Asian and Australian Monsoons typically range between 0.3–3.3 m, 1–3 m, and 0.5–2.5 m, respectively. Furthermore, extreme events can produce wave heights exceeding 3 m, and in rare cases, waves in the Natuna Sea may reach up to 5.1 m during the winter season (Anggara et al., 2018; Muliati et al., 2019).

In ALKI-II, the route is more straightforward compared to the other lanes, beginning in the Celebes Sea, which has limited exposure to the Pacific Ocean.

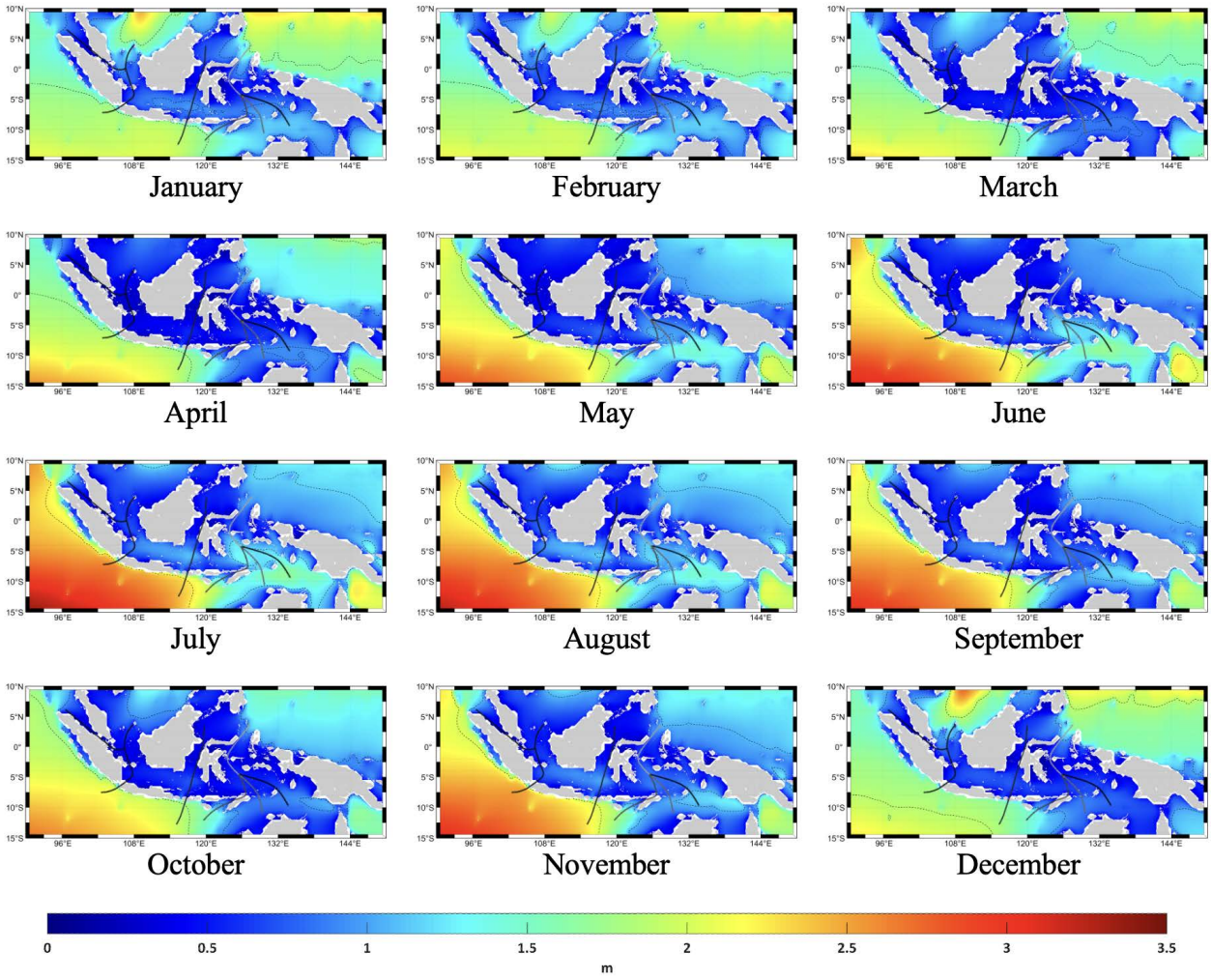

Figure 2. Monthly average significant wave height (SWH) from January 1993 to December 2023. The dashed line indicates the 2 m SWH contour.

Waves in this section generally remain low from November to March and tend to peak slightly in January and February, reaching just over 1 m. In the Makassar Strait, wave heights rarely exceed 1 m. Similar characteristics were reported by Labania et al. (2021), who found that maximum wave heights in the Makassar Strait typically range from 0.5 to 0.9 m. Further south, the Flores Sea is more open, allowing waves to build up to around 1–1.5 m in July and August. Higher waves occur outside the southern entrance of the Lombok Strait, which directly faces the Indian Ocean. As in the Sunda Strait, wave heights here can reach around 2 m during the Asian Monsoon and exceed 3 m during the Australian Monsoon, particularly between June and August.

ALKI-III begins in the Pacific Ocean, which is characterized by moderate wave activity during the Asian Monsoon period. Wave heights exceeding 2 m are observed from December to March, although these waves tend to dissipate slightly in the Maluku Sea, where they range between 1–2 m. Lail et al. (2018) similarly reported wave heights of around 1–1.5 m during the western season in Sangihe District, near the Maluku Sea. The Seram Sea, being more enclosed, generally experiences calm conditions throughout the year. In contrast, the Banda Sea is affected by the Australian Monsoon from May to August, with wave heights reaching approximately 1–1.5 m. Beyond this point, ALKI-III splits into three passages: ALKI-III A, B, and C. ALKI-III A passes through the Ombai Strait before reaching the southwest of the Sawu Sea. While the Ombai Strait remains relatively calm, the Sawu Sea experiences waves exceeding 1 m year-round, which increase to around 1.5–2 m beyond the Sawu Sea. Along the ALKI-III B route, covering the Leti Strait and the Timor Sea, wave heights exceed 1 m during January and February and become higher during the Australian Monsoon (May to August), with

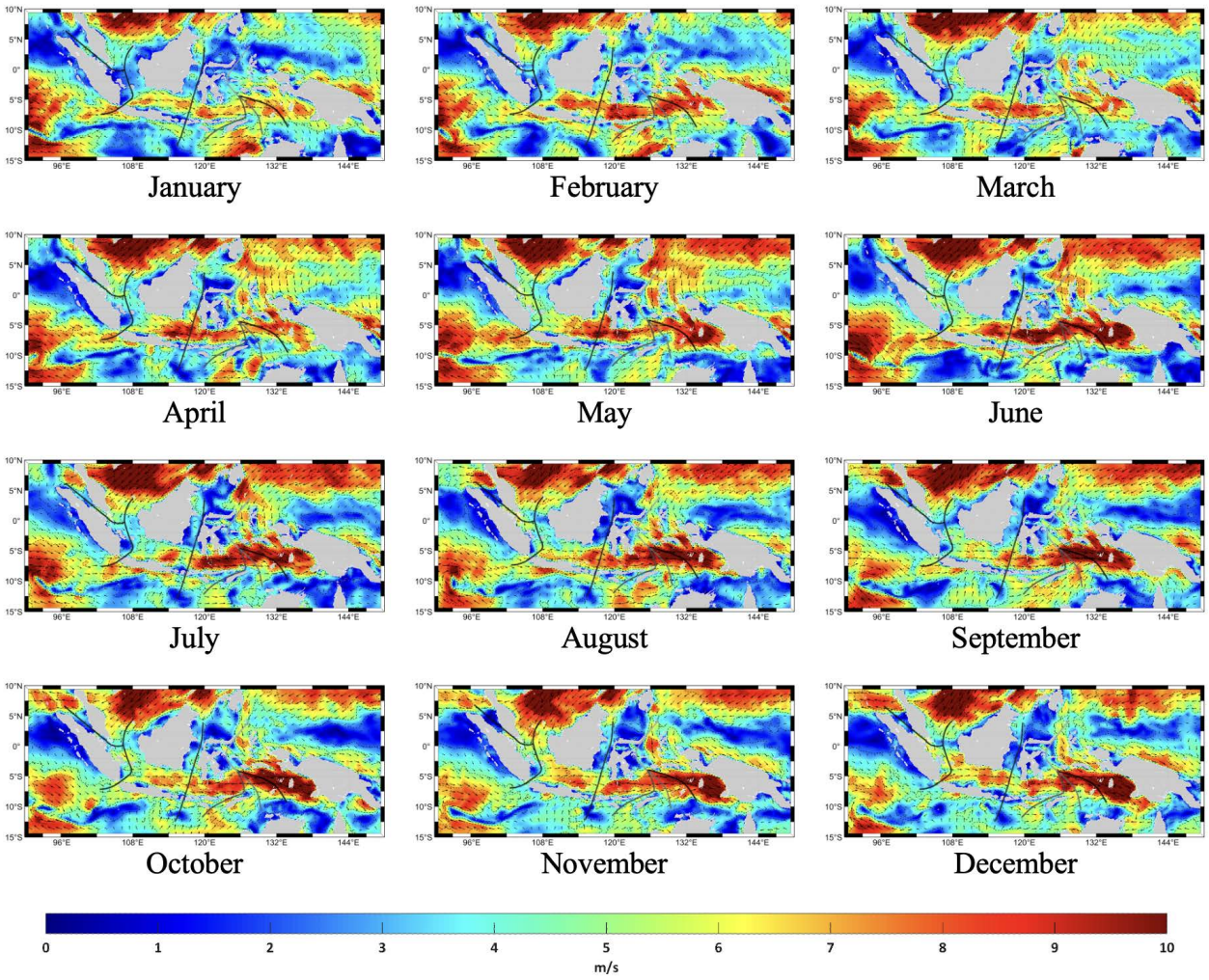

Figure 3. Monthly average 10 m wind speed from January 1993 to December 2023. Dashed line and arrows indicate wind speeds of 5 m/s and prevailing SSW direction.

significant wave heights around 1–1.5 m. A similar seasonal pattern is observed in ALKI-III C, which crosses the Arafura Sea. Here, wave heights reach slightly higher magnitudes and persist for a longer duration, lasting until September.

The wind patterns and their monthly variability are shown in Figure 3. In December, moderate to fresh breezes begin to blow southward from the South China Sea at approximately 8–10 m/s, alongside winds entering from the Pacific Ocean northeast of Indonesia. These winds move into Indonesian waters through several passages, including the Karimata Strait, Makassar Strait, Celebes Sea, and Maluku Sea. By January, wind speeds prevail inside the Java Sea, Flores Sea, and Banda Sea, generally ranging from 5–6 m/s. In the following month, speeds exceed 6 m/s in the Java Sea and rise to over 9 m/s in the Flores Sea, Banda Sea, Timor Sea, and Arafura Sea. Overall, during the Asian Monsoon period, ALKI-I experiences 4th Beaufort scale winds across the Natuna Sea, Karimata Strait, and Java Sea, especially in January and February, reaching up to 7–8 m/s. In ALKI-II, moderate breezes occur in the Makassar Strait, while stronger winds exceeding 8 m/s are observed in the Flores Sea and outside the Lombok Strait, facing the Indian Ocean. Finally, in ALKI-III, 5th Beaufort scale winds prevail along the routes in January, with wind speeds exceeding 9 m/s in February.

During the transition from the Asian monsoon to the Australian monsoon in April and May, moderate breezes begin to blow from Australia, entering from the southeast over the Arafura Sea. These winds can reach up to 8 m/s on the southern side of ALKI-III, covering the Arafura Sea, Timor Sea, Leti Strait, and Banda Sea. As the Australian monsoon sets in by June, moderate winds spread across the Banda Sea and Flores Sea, generally ranging from 7–8 m/s, and extend slightly into the Java Sea and Seram Sea. In this period, winds with speeds of 9–10 m/s are observed in the Arafura Sea, affecting parts of ALKI-II. In July, gentle to moderate breezes prevail across

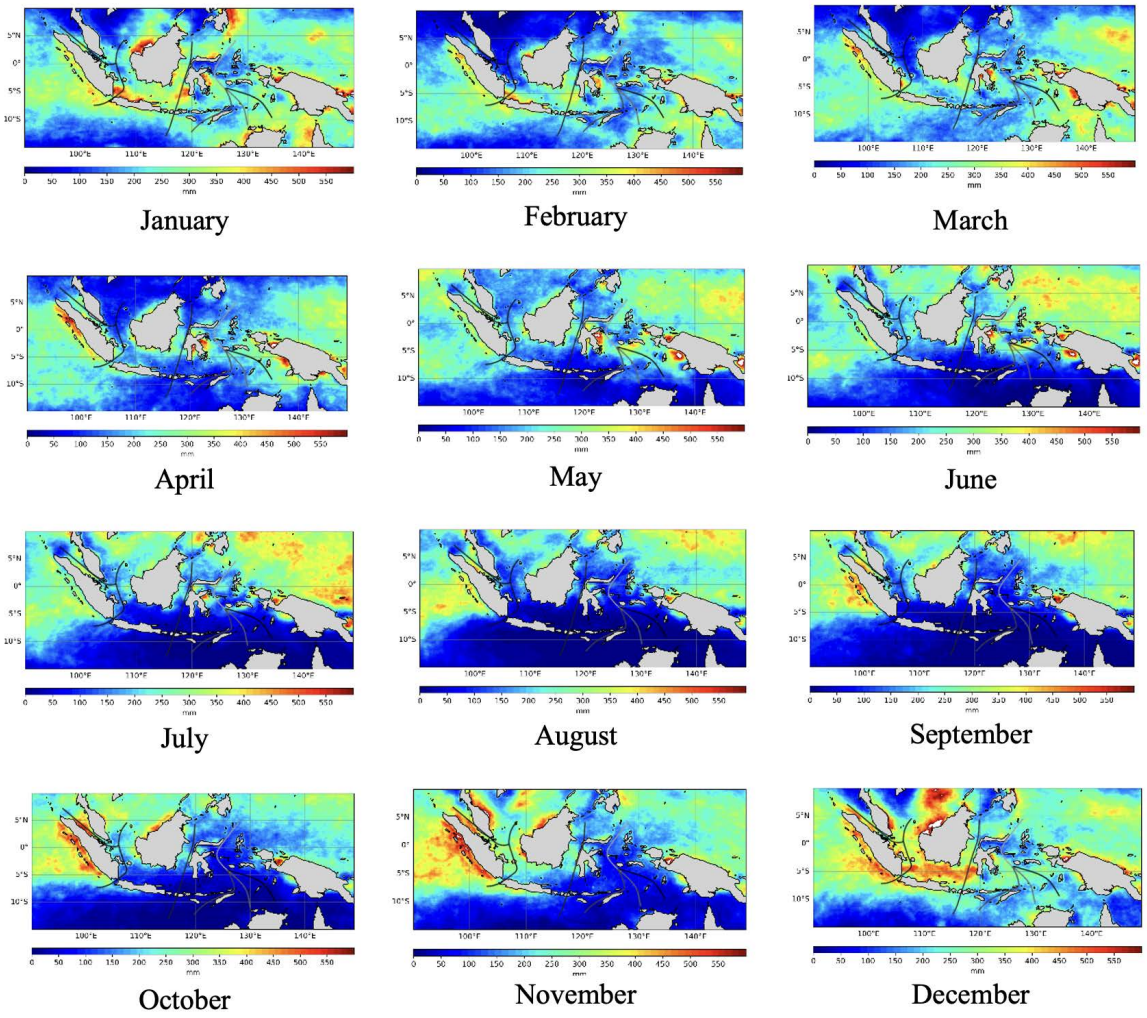

Figure 4. Monthly average precipitation (mm) from January 1993 to December 2023.

the Flores Sea, Java Sea, and Seram Sea, and begin to cross into the Karimata Strait (ALKI-I) at speeds of around 6–7 m/s. The peak season occurs in August, when winds range from 6–7 m/s as they enter the Maluku Sea and blow toward the Pacific Ocean. Stronger winds at the 4th–5th Beaufort scale from the east-southeast also occur over the Flores Sea and southern Java waters, influencing the southern ends of ALKI-I and ALKI-II. These winds continue through September, still prevailing over the Java Sea, Flores Sea, Arafura Sea, and southern Java waters, and remain detectable at the exit of the Sunda Strait into October. The observed patterns are consistent with previous studies by Wicaksana et al. (2015) and Muliati et al. (2018) in the central ALKI-I region, and Lail et al. (2018) in northern ALKI-III.

Figure 4 shows the climatological pattern of rainfall accumulation over Indonesian waters. Overall, rainfall intensity is higher in the southern part of Indonesian waters during DJF (December–February), while the northern part experiences relatively higher intensity during SON (September–November). The climatological rainfall accumulation along ALKI-I generally displays a monsoonal pattern, with peak precipitation during DJF (December–February) ranging from 350–600 mm. This peak is influenced by Asian monsoon winds that transport moist air masses from Asia toward Australia. The northern part of the Malacca Strait records higher rainfall intensity compared to the southern part, likely due to additional rainfall generated by the orographic effect of the Barisan Mountains in northern Sumatra. This finding aligns with Fujita et al. (2010), who noted that the strength of offshore rainfall is determined by the sea's width and surrounding topography. During JJA (June–August), rainfall intensity decreases notably over the Karimata Strait, Java Sea, and Sunda Strait, as the east monsoon winds cross shorter expanses of water, resulting in less humid air masses.

The ALKI-II area exhibited a similar monsoonal rainfall pattern to ALKI-I. The Sulawesi Sea, Makassar Strait, Flores Sea, and Ombai Strait experienced peak rainfall during the Asian monsoon season (DJF) and lower rainfall during the Australian monsoon season (JJA). Rainfall intensity in the JJA period was generally moderate, ranging from 50–100 mm. During DJF, the Makassar Strait recorded higher rainfall intensity, reaching 300–450 mm, while rainfall decreased towards the southern part of ALKI-II waters, particularly in the Ombai Strait, where it ranged around 100–200 mm.

In the ALKI-III region, rainfall variability between the Asian and Australian monsoon periods was notably high. The Banda Sea exhibited a local rainfall pattern, with peak monthly rainfall occurring from May to July, ranging from 200–450 mm. This pattern contrasted with that of the Maluku Sea, where peak rainfall was observed from April to June. The variability in rainfall characteristics across these areas suggests that, in addition to monsoonal influence, local topographic conditions significantly affect convective processes. In ALKI-III C, the Arafura Sea showed a monsoonal rainfall pattern similar to that of ALKI-I and ALKI-II. Rainfall intensity decreased during the transition season (March-April-May, MAM) due to the weakening of Asian monsoon winds that typically carry moist air masses.

Extreme Conditions of Significant Wave Height, Sea Surface Wind, and Precipitation

Figure 5a presents the 90th percentile map of significant wave height, based on 30 years of data. Extreme wave heights reaching approximately 3 m were primarily observed in the open Indian Ocean. In offshore regions surrounding Indonesia, particularly the South China Sea, the Pacific Ocean, western Sumatra, and southern Java waters, extreme waves could reach 2–3 m, which can be classified as moderate to high waves. Extreme wave heights of about 1–2 m were also likely to occur at the mouth of the Malacca Strait, the Natuna Sea, Java Sea, Flores Sea, Maluku Sea, Banda Sea, Arafura Sea, Sawu Sea, and Timor Sea. In contrast, other areas showed relatively calmer conditions, largely due to more sheltered or enclosed topographic features.

As shown in Figure 5b, the spatial pattern of wind speed differs notably from that of significant wave height. Nevertheless, extreme fresh breezes exceeding 10 m/s are observed in the Arafura Sea, as well as in the South China Sea and the Indian Ocean. Moderate to fresh breezes ranging from 8–10 m/s also occur in the Natuna Sea, parts of the Java and Flores Seas, the southern waters off Sumatra and Java, the Banda Sea, the Timor Sea, and south of Bali to the Nusa Tenggara Islands.

Figure 5c shows the climatological extreme rainfall distribution, represented by the 90th percentile from the 20-year dataset. The spatial extent of extreme rainfall is broader than that of average rainfall. Regions close to the equator, particularly around Sumatra and Kalimantan, exhibit higher extreme rainfall, likely driven by tropical air convergence and strong convective processes. In the

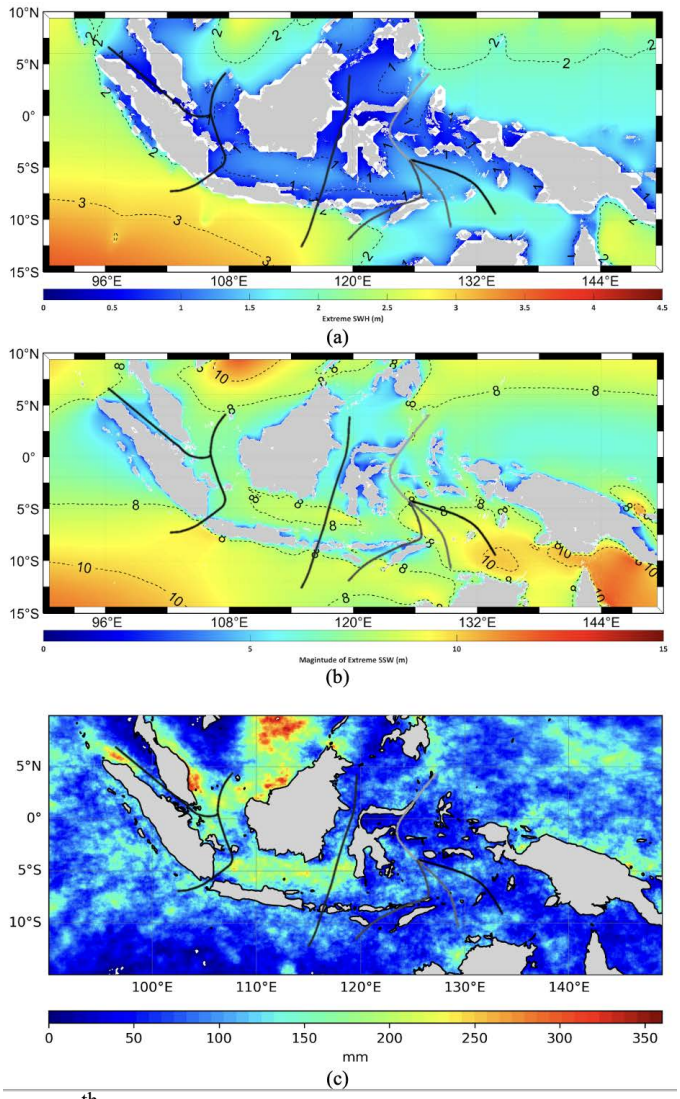

Figure 5. 90th percentile maps of (a) significant wave height, (b) wind speed, and (c) precipitation from January 1993 to December 2023.

Karimata Strait, Java Sea, and Flores Sea, extreme rainfall reaches 150–250 mm. In eastern Indonesian waters, including the Seram Sea, Timor Sea, and Maluku Sea, extreme rainfall is relatively lower, around 50–150 mm. In contrast, western and northern Indonesian waters, particularly the northern Java Sea, Natuna Sea, and South China Sea, record substantially higher extreme rainfall reaching up to 250–350 mm, which is classified by BMKG as very extreme.

Interannual Variability of Significant Wave Height

The Empirical Orthogonal Function (EOF) analysis of SWH data in ALKI-I identified two main patterns of variability, together explaining 79% of the total variance (Figure 6). The first pattern (EOF1) accounts for 44% of the variance and represents the dominant pattern of SWH variability in this region. This mode likely reflects the influence of large-scale climate phenomena, such as the El Nino–Southern Oscillation (ENSO), or major ocean currents that significantly affect sea surface height along ALKI-I. Activation of EOF1 leads to coherent SWH changes across the entire area, highlighting the role of broad-scale oceanographic dynamics. The second pattern (EOF2), explaining 35% of the variance, captures a less dominant but still substantial component of variability. This pattern may be linked to regional oceanographic processes, including seasonal variations, upwelling, or interactions between ocean currents and the local bathymetry near ALKI-I. Unlike EOF1, EOF2 displays a more localized and complex spatial structure, suggesting its influence is

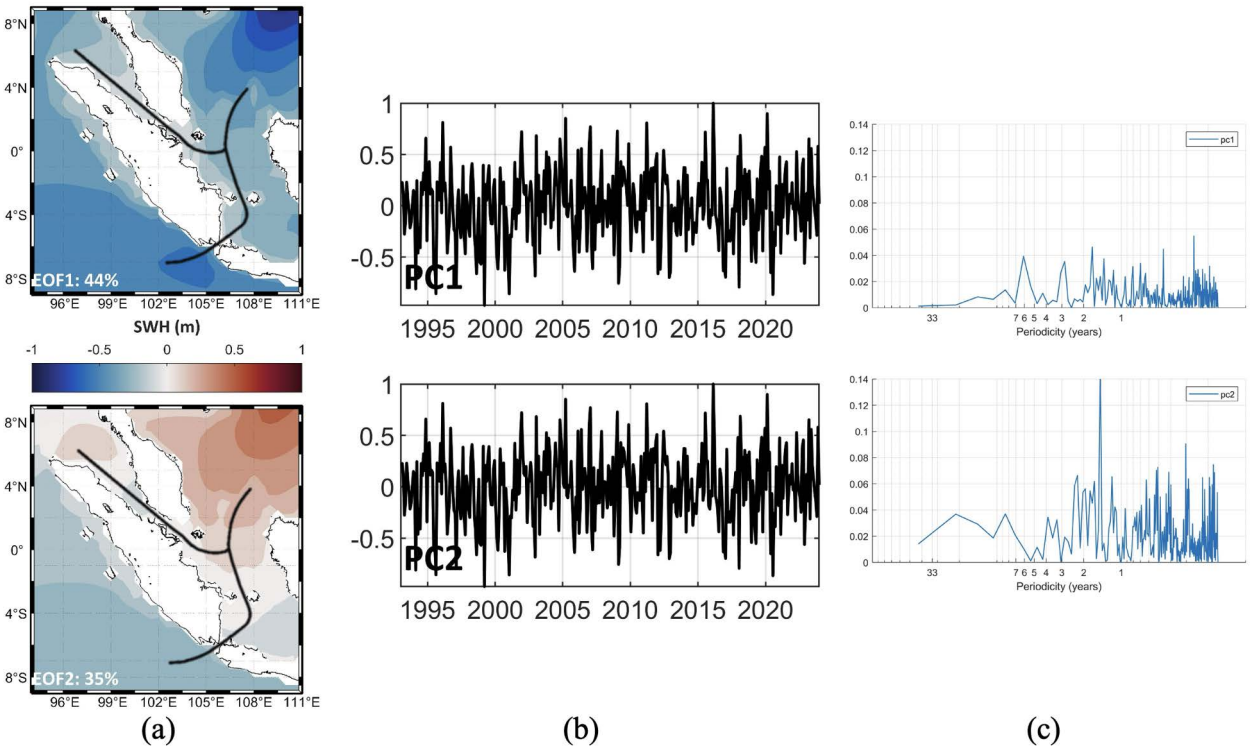

Figure 6. Results of EOF analysis for ALKI-I from January 1993 to December 2023: (a) spatial patterns, (b) temporal variability, and (c) periodicity analysis.

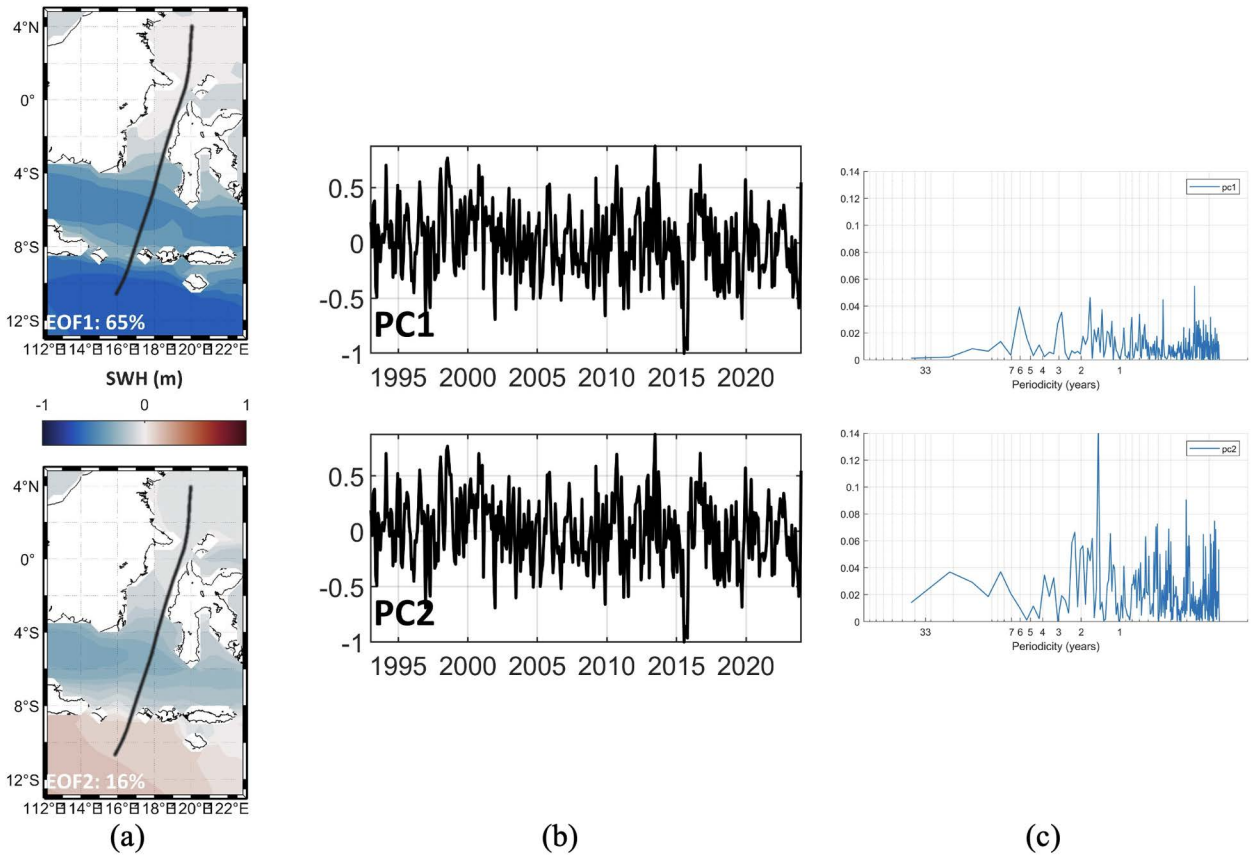

Figure 7. Results of EOF analysis for ALKI-II from January 1993 to December 2023: (a) spatial patterns, (b) temporal coefficients, and (c) periodicity.

spatially heterogeneous but still significant for SWH dynamics in the region.

The EOF analysis of SWH data in ALKI-II reveals two principal patterns of variability explaining a total of 81 % of the variance (Figure 7). EOF pattern 1, contributing 65 %, dominates SWH variability in this region. This pattern is likely associated with large scale oceanographic and atmospheric phenomena such as major ocean currents, broad sea surface temperature anomalies, and global atmospheric pressure systems. In the Indonesian context, it may relate to the Indonesian Throughflow (ITF) transporting water masses from the Pacific to the Indian Ocean, as well as the influence of monsoonal winds and global climate modes like El Niño and La Niña. EOF pattern 2, accounting for 16 % of the variance, captures a secondary but still significant component of variability. This pattern likely reflects regional to local scale processes, including local currents, coastal upwelling, and responses to changes in wind and rainfall. In ALKI-II, EOF 2 may highlight complex interactions between regional circulation and coastal dynamics, influenced by seabed topography and the archipelagic setting of Indonesia.

The results of the EOF analysis for SWH data in ALKI-III reveal two main patterns of variability, representing in total 80% of the data variance (Figure 8). EOF pattern 1, accounting for 54%, is the dominant pattern and likely reflects major drivers such as global climate variability (e.g., El Niño and La Niña) and seasonal fluctuations that broadly affect the ALKI-III region. This pattern is characterized by consistent, large scale variations linked to changes in oceanic and atmospheric circulation. EOF pattern 2 contributes 26% of the variance and captures regional or local variability, potentially associated with specific ocean currents, spatial differences in sea surface temperature, or other localized environmental factors. Although less dominant than EOF 1, EOF 2 remains important for understanding finer scale sea surface height dynamics in the region.

The global impact of the El Niño–Southern Oscillation (ENSO) drives interannual variations in Global Mean Sea Level (GMSL), particularly across the tropical and subtropical Pacific Ocean (Holbrook et al., 2020). Characterized by the periodic emergence of warmer surface waters in the equatorial eastern Pacific every 2–7 years (Figure 10), ENSO represents a major component of global climate variability (Amirudin et al., 2020). Its influence on Indonesian seas is considerable. The Indonesian Throughflow (ITF) serves as the principal oceanic conduit linking the Pacific and Indian Oceans (Edwards et al., 2020), channeling Pacific waters through the Indonesian archipelago. Due to the large

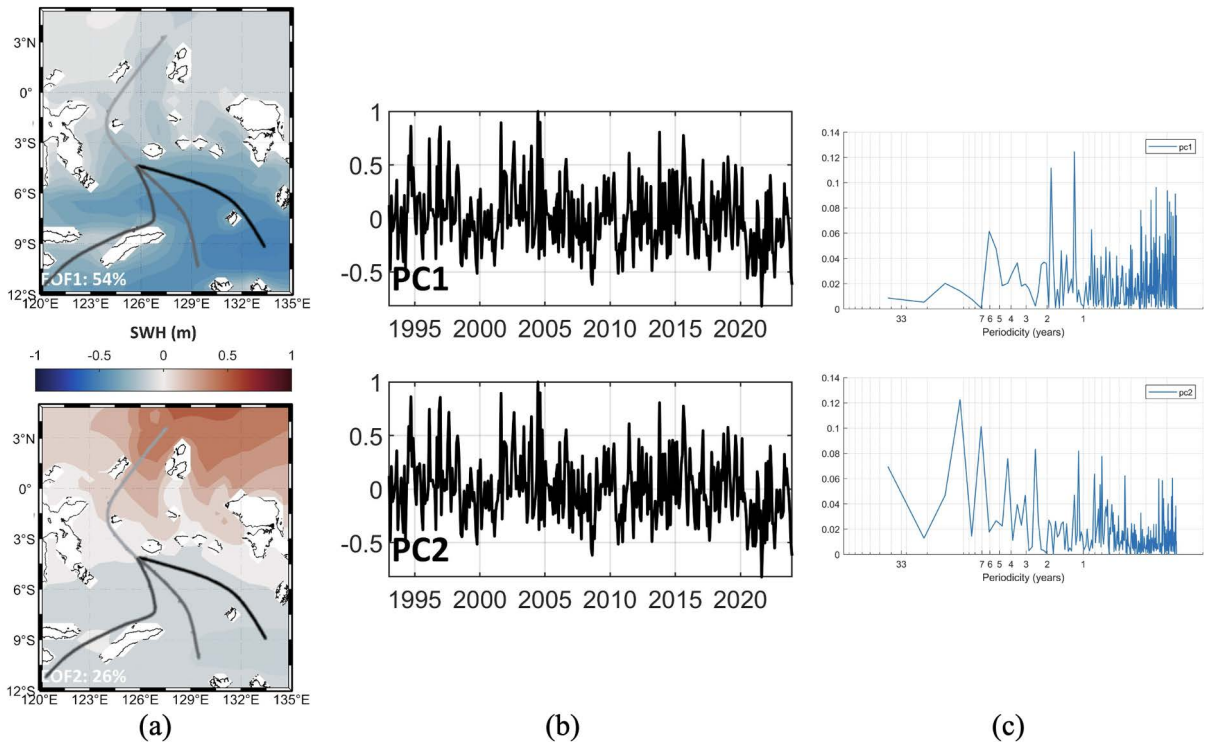

Figure 8. EOF analysis results for ALKI III from January 1993 to December 2023: (a) spatial pattern, (b) corresponding temporal component, and (c) periodicity analysis.

interannual sea level variability associated with ENSO across the western Pacific and eastern Indian Ocean, sea levels around Indonesia are strongly affected by ENSO events. Typically, El Niño episodes lead to reduced sea level and lower sea surface temperatures in Indonesian waters, whereas La Niña brings stronger trade winds, elevated sea levels, and warmer sea surface temperatures (Sanchez-Cabeza et al., 2022).

ENSO events have repeatedly affected Indonesian waters, with the most intense El Niño and La Niña episodes recorded in 1997–1998 and 2011, respectively (Figure 11). Another notable feature is the pronounced sea level decline observed since 2013, which coincided with a recent El Niño episode. In contrast, significant positive sea level anomalies were primarily observed in the Flores Sea and northern Java Sea during 2010 and 2013 (Figure 12). The characteristics of sea surface height (SSH) in Indonesian waters exhibit strong geographic and bathymetric variability, following clear seasonal patterns. In open and deeper oceanic areas, particularly within ALKI-III, SSH variations show higher sensitivity to seasonal cycles, extreme SSH events, and El Niño–La Niña phases (Dangendorf et al., 2024). In contrast, closed seas, narrow straits and shallow shelf regions such as those along ALKI-I and ALKI-II tend to display less pronounced variability. Across the Indonesian seas, SSH typically ranges from 0–4.5 m. The minimum sea level anomaly (SLA) patterns occur over western Indonesian waters between April and August, whereas the highest SLA patterns are observed from September to March, broadly coinciding with the dry season (April–October) and the wet season (September–March).

The difference in SSH between the tropical northwest Pacific (NWP) region and the southeastern Indian Ocean (SEI) region effectively represents ITF transport. Large-scale surface winds play a crucial role in sustaining these SSH differences across the tropical Pacific and Indian Oceans. The climatological surface circulation associated with the Hadley and Walker circulations, located east of the tropical Pacific, acts to accumulate surface water (Fujita et al., 2010). This leads to higher SSH in the NWP region compared to the relatively lower SSH in the SEI region. Because the SSH in the SEI region is affected by the Indian Monsoon, seasonal reversals of surface winds contribute to seasonal variations in the ITF. Beyond the climatic perspective, surface wind modulations on interannual and decadal timescales can induce ITF fluctuations by changing the SSH differences between the NWP and SEI regions. However, basin scale surface wind anomalies driven by ENSO and Indian Ocean Dipole (IOD) events, despite the usual occurrence of positive IOD alongside El Niño and negative IOD with La Niña, show limited effect on SSH differences between the NWP and SEI regions. Furthermore, the subtle effects of interannual wind variability on SSH anomalies are further diminished during recent interdecadal periods, particularly between 1993–2000 and 2000–2006 (Figures 10–13). These findings suggest limited influence on SSH differences across the Indonesian archipelagic straits during these interdecadal periods.

In contrast to the earlier assumption of similar behavior on interannual and decadal timescales, surface wind variations in both basins exhibit relative independence over a longer period (1959 to 2009) (Nidheesh et al., 2013). These studies also indicate distinct dominant spatial patterns of simulated SSH anomalies (SSHA) in ocean general circulation models across interannual and decadal timescales. The principal SSHA modes on interannual timescales display comparable loading with the same polarity across the Indonesian Archipelago straits, resulting in largely unchanged SSH differences between the NWP and SEI regions (Kara, 2016). By contrast, at the decadal timescale, the dominant mode shows significant loading in the NWP region with a less pronounced effect in the SEI region. Therefore, differences in SSH within the Indonesian Archipelago straits linked to this decadal main mode may represent a primary driver of decadal ITF variations, suggesting that the NWP and SEI regions contribute differently to these decadal changes.

Safety of Shipping and Maritime Transportation

Several key points emerge regarding the current state of safety management in Indonesia's Archipelagic Sea Lanes. Existing shipping safety arrangements in Indonesia require enhancement, particularly in terms of vessel navigation capabilities (Fatmawati et al., 2023). This highlights the need to address operational and regulatory challenges to ensure the safety of commercial maritime activities within the region. Furthermore, ships transiting Indonesian waters must adhere to internationally recognized navigational rules to minimize the risk of accidents (Sebastian et al., 2014).

The Archipelagic Sea Lanes, as specifically defined routes through the Indonesian archipelago (Lestari, 2020), play a vital role in ensuring the

unimpeded passage of foreign vessels engaged in shipping and aviation operations. As outlined in the Semaphore, Indonesia bears a critical obligation to guarantee the safe and expeditious transit of ships through its waters without hindrance or coercion (Forward, 2009), underscoring the government's role in maintaining navigational safety. In addition, substantial technical and hydrographic efforts are necessary to support maritime safety (Nugroho, 2023), as these initiatives contribute to a better understanding of local marine conditions and operational security.

The international recognition of these sea lanes further demonstrates their global importance. Through diplomatic engagement and collaboration under the International Maritime Organization (IMO), maritime nations, including Indonesia, have secured largely unrestricted access to archipelagic waters, reflecting the sea lanes' significance for global maritime trade. Nevertheless, gaps remain within the legal framework governing foreign vessel transit, which, although clear in addressing innocent passage, still lacks specific provisions to manage potential infringements by foreign ships.

Another important aspect relates to informed and safe decision-making based on environmental conditions. Recognizing the characteristics of local weather, particularly wave energy, is crucial; when used as a parameter for navigation, calm seas can support increased cruise activities, while strong winds and high waves require careful planning. In such conditions, it is necessary to ensure that ships have suitable dimensions and design to navigate safely (Anggara et al., 2018).

The Indonesian Archipelagic Sea Lanes serve as vital corridors for global maritime trade, highlighting the need to ensure both safe and efficient navigation. Despite robust international frameworks and national commitments, gaps in implementation remain. Addressing these challenges requires integrated efforts to modernize maritime infrastructure, enhance hydrographic data quality, and improve maritime domain awareness. Strengthening these aspects will reinforce Indonesia's role as a reliable maritime nation and help safeguard the security and continuity of international shipping through its waters.

CONCLUSSIONS

The variability of significant wave height (SWH) along the Indonesian Archipelagic Sea Lanes (ALKI) shows distinct patterns across the three routes. In ALKI-I, SWH typically ranges from 1–2.5 m, with higher waves observed in the northern part during the Asian Monsoon season (December–February, DJF). In ALKI-II, wave conditions remain relatively calm throughout the year, generally ranging from 1–1.5 m. Meanwhile, ALKI-III experiences higher waves in the north during DJF and in the south during the Australian Monsoon (June–August, JJA), with SWH ranging from 1–2 m. In open ocean areas such as the Indian Ocean, SWH can increase further, as reflected in the extreme condition analysis showing outer Indonesian waters occasionally reaching 2–3 m.

Wind variability in Indonesian waters is also shaped by the monsoonal cycle. During the Asian Monsoon, ALKI-I is characterized by winds corresponding to the 4th Beaufort scale, while ALKI-II and ALKI-III experience stronger winds exceeding 8 m/s and 9 m/s, respectively. In the Australian Monsoon, winds of the 4th and 5th Beaufort scale occur in the southern parts of all ALKI routes. The most extreme wind speeds, over 10 m/s, are recorded in the South China Sea, Arafura Sea, and Indian Ocean.

Rainfall distribution follows a similarly seasonal pattern. In DJF, precipitation in ALKI-I reaches 350–600 mm, while ALKI-II records values around 300–450 mm. ALKI-III, by contrast, sees peak rainfall of approximately 200–450 mm between April and July, though the Arafura Sea shows a pattern similar to ALKI-I and ALKI-II. The highest 90th percentile rainfall values, classified as very extreme by BMKG, are concentrated near the mouth of the Malacca Strait, Natuna Sea, and South China Sea (250–350 mm). Additional areas of extreme rainfall, reaching 150–250 mm, include the Karimata Strait, Java Sea, and Flores Sea.

Indonesia's strategic position as a major maritime nation traversed by these sea lanes brings significant responsibility for ensuring the safety of shipping and maritime transportation. This responsibility can be fulfilled by deepening the understanding of local metocean conditions, strengthening legal frameworks, enforcing regulations, and improving operational supervision.

Compared to previous studies, the present results may slightly underestimate wave and wind conditions in certain outer regions, which are more directly influenced by open ocean dynamics. This limitation may be attributed to the reliance on secondary data, which may not fully capture extreme events such as tropical cyclones, internal waves, squalls, or tsunamis. Therefore, stakeholders are

advised to exercise greater caution when selecting vessels and determining navigation routes, especially during high-risk periods such as the Asian Monsoon season from December to February. Moreover, due to the potential for severe weather conditions to intensify wind and wave activity beyond normal levels, it is strongly recommended to supplement planning with more specific metocean studies and reliable weather forecasts to ensure safer and more informed maritime operations.

REFERENCES

Abdullah, F. A. R., Suprijo, T., Diastomo, H., and Napitupulu, G., 2022. Numerical Modelling of Wave Attenuation in Pile Breakwater. In IOP Conference Series: *Earth and Environmental Science*, 1047 (1): 012029. IOP Publishing. https://doi.org/10.1088/1755-1315/1047/1/012029

Akbar, M. A., Sosaidi, D. S., Napitupulu, G., and Tahir, A. A. R., 2024. Response of Upwelling Parameter Before, During, and After Tropical Cyclone (Case Study: Tropical Cyclone Marcus). *Jurnal Meteorologi dan Geofisika*, 25 (1): 25-33. https://doi.org/10.31172/jmg.v25i1.1071

Aldrian, E., and Susanto, R. D., 2003. Identification of three dominant rainfall regions within Indonesia and their relationship to sea surface temperature. *International Journal of Climatology*, 23: 1435–1452. https://doi.org/10.1002/joc.950

Amirudin, A. A., Salimun, E., Tangang, F., Juneng, L., and Zuhairi, M., 2020. Differential influences of teleconnections from the Indian and Pacific Oceans on rainfall variability in Southeast Asia. *Atmosphere*, 11 (9): 886. https://doi.org/10.3390/atmos11090886

Anggara, P. D., Alam, T. M., Adrianto, D., and Pranowo, W. S., 2018. The wave characteristics in Natuna Sea and its adjacent for naval operation base purposes. *IOP Conference Series: Earth and Environmental Science*, 176: 012003. https://doi.org/10.1088/1755-1315/176/1/012003

Apriyanto, D. P., Jaya, I. N. S., and Puspaningsih, N., 2019. Examining the object-based and pixel-based image analyses for developing stand volume estimator model. Indonesian *Journal of Electrical Engineering and Computer Science*, 15 (3): 1586–1596. http://doi.org/10.11591/ijeecs.v15.i3.pp1586-1596

Batara, H., 2023. Optimizing the Development of Maritime Defense In The Natuna Sea in Realizing Indonesia As The World Maritime Axis. *Journal of Industrial Engineering & Management Research*, 4 (2): 93–101. https://doi.org/10.7777/jiemar.v4i2.468

Bayong Tjasyono, H. K., Gernowo, R., Sri Woro, B. H., and Ina, J., 2008. The character of rainfall in the Indonesian monsoon. *The International Symposium on Equatorial Monsoon System*. Yogyakarta.

Dangendorf, S., Sun, Q., Wahl, T., Thompson, P., Mitrovica, J. X., and Hamlington, B., 2024. Probabilistic reconstruction of sea-level changes and their causes since 1900. *Earth System Science Data Discussions*, 2024: 1–37. https://doi.org/10.5194/essd-16-3471-2024

Edwards, T., Yukio, M., and others., 2020. The Indonesian throughflow and its impact on biogeochemistry in the Indonesian seas. *ASEAN Journal on Science and Technology for Development*, 37 (1): 2. https://doi.org/10.29037/ajstd.596

Fatmawati, L, S., Rahman, R. A., and Yusran, N. K., 2023. Rights and Duties of Foreign Ships to Indonesian Archipelagic Sea Lanes Passage. *Diponegoro Law Review,* 8 (1): 25-40. https://doi.org/10.14710/dilrev.8.1.2023.25-40

Forward, C., 2009. Archipelagic sea-lanes in Indonesia-their legality in international law. *Austl. & NZ Mar. LJ*, 23: 143.

Fujita, M., Kimura, F., and Yoshizaki, M., 2010. Morning precipitation peak over the Strait of Malacca under a calm condition. *Monthly Weather Review*, 138 (4): 1474–1486. https://doi.org/10.1175/2009MWR3068.1

Government of Indonesia, 2021. Government Regulation Number 31 of 2021 concerning the Implementation in the Field of Shipping. Retrieved from https://peraturan.bpk.go.id/Details/161880/pp-no-31-tahun-2021.

Holbrook, N. J., Claar, D. C., Hobday, A. J., McInnes, K. L., Oliver, E. C. J., Gupta, A. Sen, Widlansky, M. J., and Zhang, X., 2020. ENSO-driven ocean extremes and their ecosystem impacts. *El Niño Southern*

Oscillation in a Changing Climate: 409–428. https://doi.org/10.1002/9781119548164.ch18

Hutagalung, S. M., 2017. Penetapan Alur Laut Kepulauan Indonesia (ALKI): Manfaatnya dan Ancaman Bagi Keamanan Pelayaran di Wilayah Perairan Indonesia. *Jurnal Asia Pacific Studies*, 1 (1): 75–91.

BMKG, 2024. Prakiraan Cuaca Maritim. https://maritim.bmkg.go.id/ [Accessed on 25 March 2024].

BMKG, 2024. Intensitas Curah Hujan Harian Indonesia. https://web-meteo.bmkg.go.id//media/data/bmkg/mfy/daily_obs_rainfall_indonesia.png [Accessed on 25 March 2024].

Izaguirre, C., Losada, I. J., Camus, P., Vigh, J. L., and Stenek, V., 2021. Climate change risk to global port operations. Nature Climate Change, 11 (1): 14–20. https://doi.org/10.1038/s41558-020-00937-z

Kara, G., 2016. Analysis of Meteorological Factors Affecting on Maritime Transport Systems. *Proceedings Book*: 693.

Kartadikaria, A. R., Napitupulu, G., Rangga, K., Radjawane, I. M., and Abdullah, F. A. R., 2024. Ketidakseragaman Sebaran Spasial Variabilitas Musiman Eddy di Perairan Barat Laut Indonesia. *Jurnal Kelautan Tropis*, 27 (1): 1-16. https://doi.org/10.14710/jkt.v27i1.20810

Labania, H. M. D., Mudin, Y., Rahman, A., Sabhan, and Pranowo, W. S., 2021. Analysis of seasonal variability of wave height in Makassar Strait. *Journal of Physics: Conf. Series*, 1763: 012031. https://doi.org/10.1088/1742-6596/1763/1/012031

Lail, A., Monang, S. Setiadi J., and Pranowo, W. S., 2018. Characteristics of Ocean Waves for Wharf Construction Information (Lanal Tahuna Case Study). *Jurnal Hydropilar,* 4 (2): 69-76.

Lestari, M. M., 2020. What Is the Right, Archipelagic Sea Lanes and Passage? (According to UNCLOS 1982 and Practice). *Indonesian J. Int'l L.*, 18: 209.

Monika, F., Baiquni, M., and Hadi, M. P., 2022. Foreign vessels' mobility crossing the Archipelagic Sea Lanes in the Karimata Strait. *Aquaculture, Aquarium, Conservation & Legislation*, 15 (4): 1712–1730.

Monios, J., and Wilmsmeier, G., 2020. Deep adaptation to climate change in the maritime transport sector–a new paradigm for maritime economics? *Maritime Policy & Management*, 47 (7): 853–872. https://doi.org/10.1080/03088839.2020.1752947

Muliati, Y., Tawekal, R. L., Wujanto, A., Kelvin, J., and Pranowo, W. S., 2018. Application of SWAN Model for Hindcasting Wave Height in Jepara Coastal Waters, North Java, Indonesia. *International Journal of GEOMATE,* 15 (48): 114 – 120.

Muliati, Y., Tawekal, R. L., Wujanto, A., Kelvin, J., and Pranowo, W. S., 2019. Wind Wave Modeling in Natuna Sea: A Comparison Among SWAN, SEAFINE, and ERA-Interim. *International Journal of GEOMATE,* 16 (54): 176 – 184.

Nagi, A., Napitupulu, G., Setyobudiandi, I., and Kawaroe, M., 2023. Utilization of the coastal area of Miangas Island as the outermost small island of Indonesia. *Akuatikisle: Jurnal Akuakultur, Pesisir dan Pulau-Pulau Kecil*, 7 (1): 85-92. https://doi.org/10.29239/j.akuatikisle.7.1.85-92

Nainggolan, P. P., 2016. Indonesia dan Ancaman Keamanan di Alur Laut Kepulauan Indonesia (ALKI). *Kajian*, 20 (3): 183–200.

Napitupulu, G., 2024. Monthly variability of wind-induced upwelling and its impact on chlorophyll-a distribution in the Southern and Northern parts of the Indonesian Archipelago. *Ocean Dynamics*, 74 (10): 859-878. https://doi.org/10.1007/s10236-024-01640-9

Napitupulu, G., 2025. Eddy-induced modulation of marine heatwaves and cold spells in a tropical region: a case study in the Natuna Sea area. *Ocean Dynamics*, 75 (3): 28. https://doi.org/10.1007/s10236-025-01673-8

Napitupulu, G., Fekranie, N. A., Nurdjaman, S., Suprijo, T., and Subehi, L., 2022c. Analysis of Upwelling Variations Caused by ENSO Intensification in the Southern Makassar Strait. In *International Conference on Radioscience, Equatorial Atmospheric Science and Environment*: 437-448. Singapore: Springer Nature Singapore. https://doi.org/10.1007/978-981-19-9768-6_41

Napitupulu, G., Nagi, A., Nurdjaman, S., Radjawane, I. M., Rachmayani, R.,

Ramadhan, M. R., ... and Kelvin, F. M., 2025. Impact of marine heatwaves and cold spells on coral reef ecosystem in a tropical region: a case study of Lombok Waters, Indonesia. *Marine Systems & Ocean Technology*, 20 (1): 16. https://doi.org/10.1007/s40868-024-00160-x

Napitupulu, G., Nuruddin, M. F., Fekranie, N. A., and Magdalena, I., 2021. Analysis of wind-generated wave characteristics by SWAN model in Balikpapan Bay. In IOP Conference Series: *Earth and Environmental Science,* 930 (1): 012067. IOP Publishing. https://doi.org/10.1088/1755-1315/930/1/012067

Napitupulu, G., Radjawane, I. M., Azuga, N. A., Pratama, K. R., Fekranie, N. A., and Park, H., 2022b. Identification of Seasonal Water Mass Characteristics in West Sumatra Waters. In *International Conference on Radioscience, Equatorial Atmospheric Science and Environment*: 531-543. Singapore: Springer Nature Singapore. https://doi.org/10.1007/978-981-19-9768-6_49

Napitupulu, G., Tarya, A., Pratama, I. G. M. Y., and Winardhie, I. S., 2022a. Variability Analysis of Significant Wave Heights and Wind Waves in Riau Archipelago Sea part ALKI 1. *Jurnal Pesisir dan Laut Tropis*, 10 (3): 341-355. https://doi.org/10.35800/jplt.10.3.2022.44933

Nidheesh, A. G., Lengaigne, M., Vialard, J., Unnikrishnan, A. S., and Dayan, H., 2013. Decadal and long-term sea level variability in the tropical Indo-Pacific Ocean. *Climate Dynamics*, 41: 381–402. https://doi.org/10.1007/s00382-012-1463-4

Ningsih, N. S., Azhari, A., and Al-Khan, T. M., 2023. Wave climate characteristics and effects of tropical cyclones on high wave occurrences in Indonesian waters: Strengthening sea transportation safety management. *Ocean & Coastal Management*, 243: 106738. https://doi.org/10.1016/j.ocecoaman.2023.106738

Nugroho, S. S., 2023. Is it Illegal for Foreign Vessels to Transit Through Indonesian Waters without Utilizing The Archipelagic Sea Lanes?. *Jurnal Bina Mulia Hukum*, 8 (1): 78-91. https://orcid.org/0000-0001-7472-9126

Nurdjaman, S., Nasution, M. I., Johan, O., Napitupulu, G., and Saleh, E., 2023. Impact of climate change on coral reefs degradation at West Lombok, Indonesia. *Jurnal Kelautan Tropis*, 26 (3): 451-463. https://doi.org/10.14710/jkt.v26i3.18540

Prasetyo, K. A., Prakoso, L. Y., and Sianturi, D., 2020. Marine Defense Strategy the Indonesian Government In The Construction of Laws On Indonesian Archipelagic Sea Lanes. *Maritime Defense Strategy Study Program Journal*, 6 (3). http://dx.doi.org/10.37500/IJESSR.2021.4320

Radjawane, I. M., Basuki, I. N., and Napitupulu, G., 2023 Pelacakan Mundur Partikel Sampah Laut dengan Metode Euler-Lagrange di Pelabuhan Ratu. *Limits: Journal Of Mathematics and its Applications*, 20 (3): 371-391. http://dx.doi.org/10.12962%2Flimits.v20i3.18676

Radjawane, I. M., Mughny, G. P., and Napitupulu, G., 2024. Karakteristik Estuari di Muara Angke pada Musim Timur. *Jurnal Kelautan Tropis*, 27 (1): 28-38. https://doi.org/10.14710/jkt.v27i1.20679

Ramadhan, M. A., Anggraeny, F. T., and Putra, C. A., 2024. Klasifikasi Curah Hujan Harian Menggunakan Metode K-Nearest Neighbor. *JATI (Jurnal Mahasiswa Teknik Informatika)*, 8(3): 3863-3869. https://doi.org/10.36040/jati.v8i3.9817

Republic of Indonesia, 1985. Law No. 17 of 1985 on the Ratification of the United Nations Convention on the Law of the Sea. Retrieved from https://peraturan.bpk.go.id/Details/46968/uu-no-17-tahun-1985.

Republic of Indonesia, 2008. Law No. 17 of 2008 on Shipping. Retrieved from https://peraturan.bpk.go.id/Details/39060.

Republic of Indonesia, Ministry of Transportation, 2015. Minister of Transportation Regulation No. 20 of 2015 concerning Shipping Safety Standard. Retrieved from https://peraturan.bpk.go.id/Details/103399/permenhub-no-20-tahun-2015.

Royal Meteorological Society, The Beaufort Wind Scale <https://www.rmets.org/metmatters/beaufort-wind-scale> [Accessed on 25 March 2024].

Sanchez-Cabeza, J.-A., Herrera-Becerril, C. A., Carballo, J. L., Yáñez, B., Álvarez-Sánchez, L. F., Cardoso-Mohedano, J.-G., and Ruiz-Fernández, A. C., 2022. Rapid surface water

warming and impact of the recent (2013–2016) temperature anomaly in shallow coastal waters at the eastern entrance of the Gulf of California. *Progress in Oceanography*, 202: 102746. https://doi.org/10.1016/j.pocean.2022.102746

Sebastian, L. C., Supriyanto, R. A., and Arsana, I. M. A., 2014. Indonesia and the Law of the Sea: Beyond the archipelagic outlook. INDONESIA AT HOME AND ABROAD, 67 pp.

Suprijo, T., Napitupulu, G., Ginting, J. W., Simanjuntak, E. M., Abdullah, F. A., and Khadami, F., 2024. Transformasi Gelombang Reguler Akibat Pemecah Gelombang Tiang Pancang Dua Baris Selang-Seling. *Jurnal Teknik Hidraulik*, 15 (2): 99-112. https://doi.org/10.32679/jth.v15i2.787

Wicaksana, S., Sofian, I., Pranowo, W. S., Kuswardani, A. R. T. D., Saroso, and Sukoco, N. B., 2015. Karakteristik Gelombang Signifikan di Selat Karimata dan Laut Jawa Berdasarkan Rerata Angin 9 Tahunan (2005-2013). *Omni-Akuatika*, 11 (2): 33-40. http://dx.doi.org/10.20884/1.oa.2015.11.2.37

Xing, W., and Zhu, L., 2021. A functional approach to reassessing the legal status and navigational rights of ships and ship-shaped structures. *Transport Policy*, 106: 120–130. https://doi.org/10.1016/j.tranpol.2021.03.025

Yamanaka, M. D., Ogino, S.-Y., Wu, P.-M., Jun-Ichi, H., Mori, S., Matsumoto, J., and Syamsudin, F., 2018. Maritime continent coastlines controlling Earth's climate. *Progress in Earth and Planetary Science*, 5 (1): 1–28. https://doi.org/10.1186/s40645-018-0174-9

BEARING CAPACITY AND SETTLEMENT BEHAVIOUR OF COASTAL SOIL FOR THE PLANNED BALONGAN PORT DEVELOPMENT, WEST JAVA

DAYA DUKUNG DAN PERILAKU PENURUNAN TANAH PESISIR UNTUK RENCANA PENGEMBANGAN PELABUHAN BALONGAN, JAWA BARAT

Adam Raka Ekasara[1*], Purnomo Raharjo[2], Susilowati[1]

[1] Geological Engineering, Universitas Pembangunan Nasional "Veteran" Yogyakarta, Sleman

[2] Marine Geological Institute, Bandung

*Corresponding author: adam.raka@upnyk.ac.id

(Received 06 May 2025; in revised from 06 May 2025; accepted 28 June 2025)

DOI : 10.32693/bomg.40.1.2025.943

ABSTRACT: The planned development of Balongan Port in West Java requires a comprehensive geotechnical evaluation to support foundation planning at the proposed site, which is underlain by soft, clay-rich sediments. This study aims to assess the bearing capacity of the subsurface and predict potential settlement behaviour by integrating field and laboratory investigations. Standard Penetration Test (SPT) data from two boreholes, BH-3 (14 m) and BH-4 (18 m), and were complemented by laboratory analyses of soil physical and mechanical properties. The site is primarily composed of high-plasticity clay, known for its low strength, high compressibility, and variable geotechnical characteristics. Calculations based on SPT results yielded allowable loads of 53.1 tons at BH-3 and 39.0 tons at BH-4, respectively, while laboratory analyses indicated significantly higher bearing capacities of 265.9 tons and 884.4 tons, respectively. Settlement predictions based on SPT and laboratory data were 0.61 cm and 2.07 cm, with an estimated 90% consolidation period of about 12.9 years. These findings emphasize the variability and compressibility of the soft clay strata as well as the importance of employing multiple assessment methods. The study provides essential input for foundation planning and highlights the need for integrated geotechnical assessment methods to ensure the safety, reliability, and long-term performance of pile-supported structures at the proposed port site.

Keywords: Pile foundation, SPT, bearing capacity, settlement prediction, Balongan Port

ABSTRAK: *Rencana pengembangan Pelabuhan Balongan di Jawa Barat memerlukan evaluasi geoteknik yang komprehensif untuk mendukung perencanaan fondasi pada lokasi yang diusulkan, yang didominasi oleh sedimen lempung lunak. Studi ini bertujuan untuk menilai daya dukung tanah dan memprediksi perilaku penurunan melalui integrasi data uji lapangan dan laboratorium. Data Uji Penetrasi Standar (SPT) diperoleh dari dua titik bor, yaitu BH-3 (14 m) dan BH-4 (18 m), dan dilengkapi dengan analisis laboratorium terhadap sifat fisik dan mekanik tanah. Lokasi yang dikaji terutama terdiri dari lempung plastisitas tinggi yang dikenal memiliki kekuatan rendah, daya mampat tinggi, serta karakteristik geoteknik yang bervariasi. Perhitungan berdasarkan data SPT menunjukkan beban izin sebesar 53,1 ton (BH-3) dan 39,0 ton (BH-4), sedangkan analisis laboratorium menghasilkan nilai yang jauh lebih tinggi yaitu 265,9 ton dan 884,4 ton secara berturut-turut. Prediksi penurunan berdasarkan data SPT dan laboratorium masing-masing sebesar 0,61 cm dan 2,07 cm, dengan estimasi waktu konsolidasi 90% sekitar 12,9 tahun. Temuan ini menyoroti variabilitas dan kemampatan tanah lempung lunak, serta pentingnya penggunaan metode asesmen yang beragam. Studi ini memberikan masukan penting bagi*

perencanaan fondasi dan menekankan perlunya pendekatan geoteknik yang terintegrasi guna menjamin keamanan, keandalan, dan kinerja jangka panjang struktur fondasi tiang pada lokasi pelabuhan yang direncanakan.

Kata Kunci: *Fondasi tiang pancang,* SPT*, daya dukung tanah, prediksi penurunan tanah, Pelabuhan Balongan*

INTRODUCTION

The development of maritime infrastructure is essential for supporting regional logistics, economic integration, and national connectivity. A strategic coastal zones identified for a new port facility is located in the Balongan area of Indramayu Regency, West Java. The area lies near major transportation routes, including toll roads and railway lines, providing logistical advantages for future port operations.

However, the subsurface conditions of the Balongan coastal plain apredominantly composed of soft, clay-rich alluvial and marine sediments. Such soils are known for their low bearing capacity, high compressibility, and long consolidation periods, posing major geotechnical challenges for foundation design, particularly for heavy port structures such as container yards, piers, and storage terminals (Bo et al., 2015; Shah, 2021). Inadequate consideration of these conditions during early planning stages may result in excessive settlement, differential movement, or even structural instability in the long term.

To support the planning and feasibility assessment of the proposed Balongan Port, a preliminary geotechnical study was conducted to evaluate subsurface conditions, bearing capacity, and potential settlement behaviour of pile foundations. The investigation involved Standard Penetration Tests (SPT) at two borehole locations, complemented by laboratory testing of soil physical and mechanical properties. The combined approach is intended to provide reliable and practical input for decision-making in early-stage design and land-use planning for the proposed site.

This paper presents the findings of that investigation, discusses the implications of the subsurface characteristics on foundation behaviour, and offers recommendations for future geotechnical evaluation and engineering design strategies

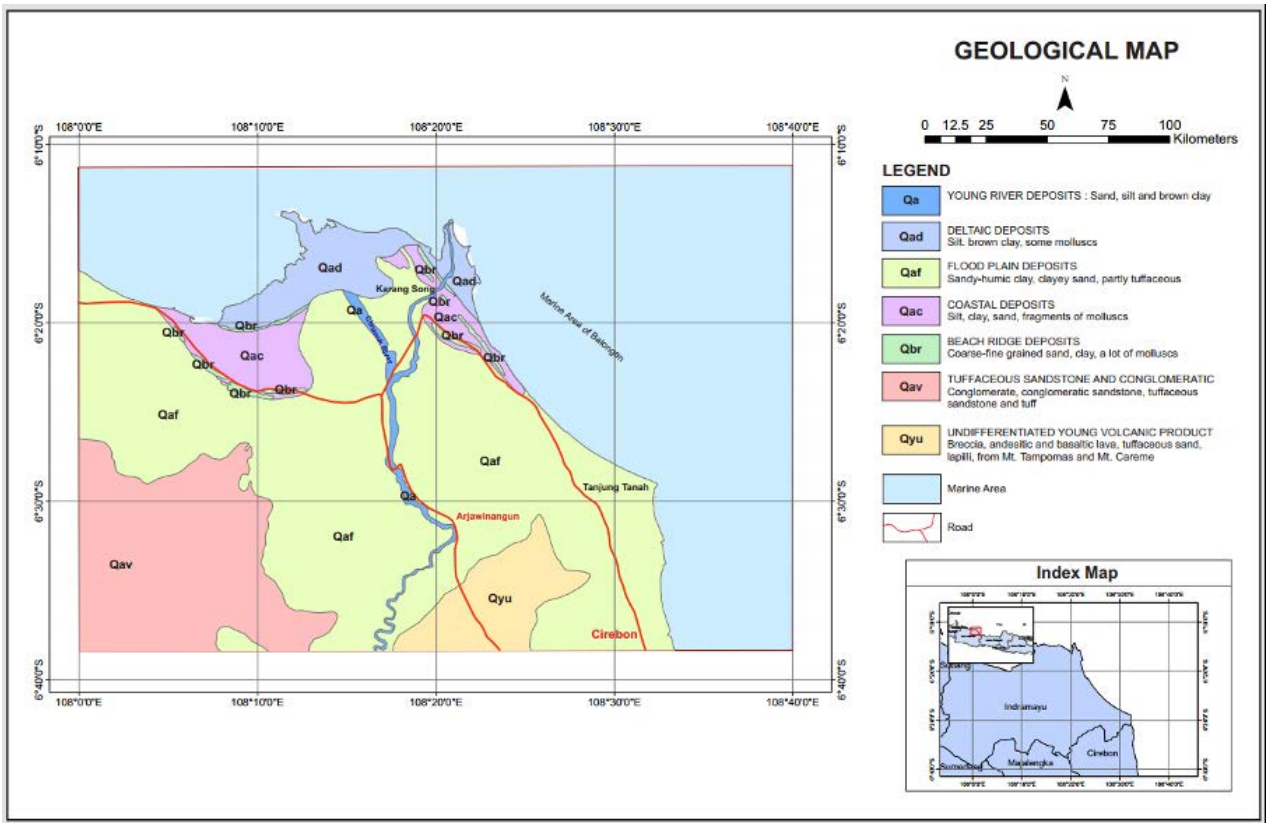

Figure 1. Geological map of the Balongan coastal area, West Java

appropriate for soft clay-dominated port development sites.

Geological Setting

The morphology of the study area is generally characterized as coastal environment. The morphological characteristics of the Balongan coastal area consist of sandy beaches and a delta. The sandy beach morphology stretches from the tip of Tanjung Tanah to the Karang Song area, which is strongly influenced by marine energy processes, including both waves and currents.

The study area (Figure 1) is an alluvial plain composed of beach ridge deposits, floodplain deposits, beach deposits, delta deposits, and river deposits (Achdan & Sudana, 1992). At the mouth of the Cimanuk River, there are delta deposits consisting of a mixture of terrestrial and marine sediments. These sediment distributions form an alluvial fan, resembling a birdfoot delta. Along the coastline, various forms of aquaculture have been developed, including shrimp ponds, salt ponds, and settlements (Ilahude and Usman, 2009).

The beach ridge deposits consist of coarse to fine sand and clay, and are rich in mollusks. The height of the ridges reach up to 5 meters. These ridges are generally limited to the coastal area, with some of them positioned parallel to one another, while others radiate from a single point. This area is home to settlements and serves as a transportation route. Part of the Jakarta–Cirebon highway runs along these beach ridges.

The floodplain deposits consist of sandy clay, humus clay, and range in color from brownish-gray to black. Southward, these deposits become more compact, and their color gradually shifts to a reddish hue. This unit overlying older strata is characterized by erosional surfaces, as observed in the Cibogor River and the upstream section of Kali Kandanghaur. These deposits extend broadly into the Cirebon and Arjawinangun areas as alluvium.

The delta deposits consist of silt and clay, with a brownish-black color, containing small amounts of mollusks, ostracods, planktonic foraminifera, and benthic foraminifera. This unit is typically found in areas designated for the cultivation of milkfish, shrimp ponds, and mangrove forests.

The river deposits consist of sand, silt, and clay, with a brown color, and are predominantly found along the Cimanuk River.

METHODS

Preliminary Stage

The preliminary stage of this research involved a comprehensive review of literature and secondary data to support early-stage geotechnical evaluation for the proposed Balongan Port site. This included the compilation and analysis of regional geological information, topographic and thematic maps, as well as previously published studies relevant to coastal soft soil behaviour, pile foundation design, and port infrastructure on lowland marine deposits. Some important secondary data include:

1. Geological maps at a scale of 1:100,000, particularly the Indramayu Sheet compiled by Achdan and Sudana (1992), which provide stratigraphic and lithological context for the site.
2. Topographic maps and satellite imagery to assess site accessibility, surface morphology, and potential drainage patterns.
3. Location map of the drilling points

This stage was critical in determining the representative locations for borehole drilling and field testing. Borehole locations BH-3 and BH-4 were selected based on a combination of geological considerations, site accessibility, and anticipated variability in subsurface conditions. The information gathered during the preliminary stage served as the foundation for designing the subsequent field investigation program and for contextualizing the geotechnical data within the broader geological framework of the site.

Data Collection Stage

The data collection stage consisted of systematic field investigations and laboratory testing aimed at characterize the geotechnical properties of the proposed Balongan Port site. This stage was conducted in accordance with internationally recognized geotechnical standards to ensure the quality, accuracy, and reproducibility of the data.

1. Field Investigation

Subsurface exploration was conducted through rotary core drilling at two borehole (BH-3 and BH-4) locations (Figure 2), reaching depths of 50 meters. These locations were selected during the preliminary study based on geological context and accessibility. Drilling employed a single-tube rotary system suitable for retrieving cohesive soil samples in soft ground conditions. Undisturbed soil samples were extracted at selected depths using Shelby tubes,

following the ASTM D1587 standard, to preserve the in-situ structure of the soft clay for laboratory testing.

SPT were performed at 2 meter intervals throughout the borehole depth, following ASTM D1586. The N-values obtained from SPT were used to assess soil strength profiles and to estimate the allowable bearing capacity of pile foundations using empirical correlations.

Where W is the weight of water and Ws is the weight of the dry soil after oven drying.

b. Bulk density (ASTM D7263)

Wet bulk density (γ_b) is the ratio of the weight of the soil particles, including water and air (W), to the volume of the soil (V). It can be expressed using the following formula:

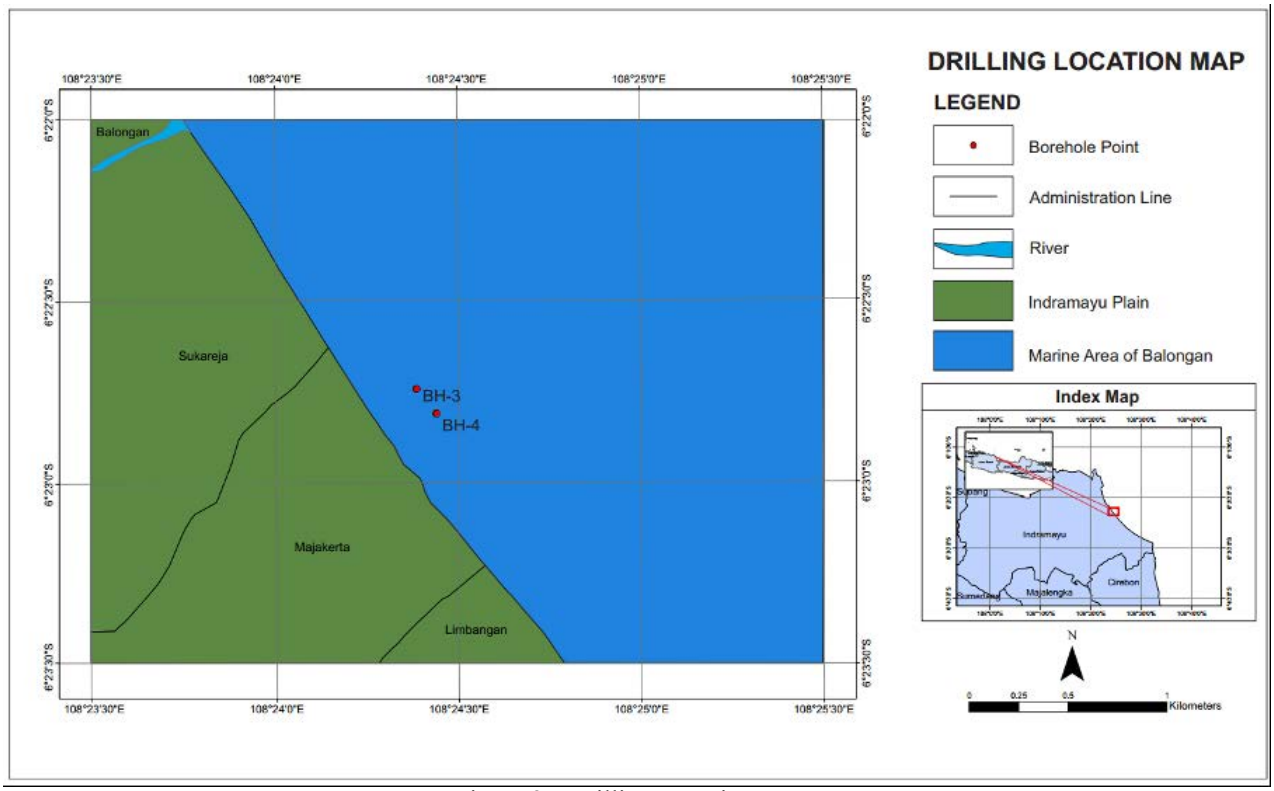

Figure 2. Drilling Location Map

2. Laboratory testing

Laboratory tests were carried out on both undisturbed and disturbed soil samples obtained from field drilling. The tests were conducted at the Soil Testing Laboratory of Politeknik Negeri Bandung. The following tests were performed:

a. Water content (ASTM D2216)

The water content test is used to determine the percentage of water in the sample. This test was conducted twice for each undisturbed sample (UDS).

Water content (W_c) can be calculated using the following equation:

$$w_c = \frac{W_w}{W_s}\ x\ 100\%$$

$$\gamma_b = \frac{W}{V}$$

Dry Bulk Density (γ_d) is the ratio of the weight of the soil particles (Ws) to the total volume of the soil (V). It can be expressed using the following formula:

$$\gamma_d = \frac{W_s}{V}$$

Solid Particle Density (γs) is the ratio of the weight of the solid soil particles (Ws) to the volume of the solid soil particles (Vs). It can be expressed using the following formula:

$$\gamma_s = \frac{W_s}{V_s}$$

c. Specific Gravity (ASTM D854)

The Specific Gravity (GS) test is conducted twice for each UDS. The purpose of this test is to obtain the value of Gs. Specific gravity (or specific weight) is the ratio between the mass (or weight) of dry soil particles (γ_s) and the mass (or weight) of distilled water occupying the same volume as the soil particles (γ_w). The parameter was computed as:

$$G_s = \frac{\gamma_s}{\gamma_w}$$

d. Atterberg Test (ASTM D4318)

Atterberg provided a method to describe the consistency limits of fine-grained soils by considering their water content. These limits include the liquid limit (LL), plastic limit (PL), shrinkage limit (SL), and plasticity index (LI).

Furthermore, Atterberg (1911, as cited in Hardiyatmo, 2002) divided the plasticity index limits and soil types (Table 1).

e. Direct Shear Test (ASTM D3080)

Table 1. Plasticity index limits

PI	Soil property	Soil types	Cohesion
0	Non-plastic	Sand	Non-cohesive
< 7	Slightly plastic	Silt	Partially cohesive
7-17	Medium plastic	Silty Clay	Cohesive
>17	Highly plastic	Clay	Cohesive

This test is conducted to examine UDS specimens obtained from drilling. The purpose of this test is to determine the cohesion parameter (c) and the internal friction angle (Φ). The testing is carried out using three test samples for each undisturbed sample, with different loading conditions applied to each.

f. Consolidation Test (ASTM D2435)

This test is conducted to obtain the compression parameters for the magnitude of settlement from a consolidation parameter, to estimate the rate of settlement.

All test procedures adhered to standard protocols, and multiple trials were conducted to verify data reliability. Results from field and laboratory data were integrated to evaluate the geotechnical behaviour of the subsurface materials and to support bearing capacity and settlement analyses.

Data Processing Stage

The data processing stage focused on interpreting the results of field and laboratory investigations to evaluate the geotechnical performance of the proposed port site. Two primary aspects were analyzed in this stage: (1) allowable bearing capacity of pile foundations, and (2) settlement estimation of soft clay layers. Analyses were conducted using both empirical correlations from SPT data and numerical calculations based on soil properties derived from laboratory tests.

Bearing Capacity Based on SPT Values

The ultimate bearing capacity of a pile (Q_u) is the sum of the ultimate tip resistance (Q_b) and the skin friction resistance (Q_s) between the pile shaft and the surrounding soil, expressed by the following equation (Meyerhof, 1976):

$$Q_u = Q_b + Q_s$$
$$= A_b f_b + A_s f_s$$

Where:

A_b = Cross-sectional area of the pile tip (m² or ft²)

A_s = Surface area of the pile shaft (m² or ft²)

f_b = Average unit tip resistance (kN/m² or tons/m²)

f_s = Average unit skin friction (kN/m² or tons/m²)

The ultimate bearing capacity of a pile can be calculated empirically based on the SPT N-values. The tip resistance of the pile was calculated from SPT N-values using Meyerhof's equation;

$$Q_b = A_b (40N”) L_b/B \leq A_b (380N”)$$

Where:

N” = The statistical average value of the SPT numbers in the area approximately 8B above to 3B below the pile tip.

B = The width or diameter of the pile.

L_b/B = The ratio of the average depth of a point.

The skin friction resistance of the pile was calculated from SPT N-values using Meyerhof's equation (Bowles, 1993), which is:

$$Q_s = X_m N p L_i$$

Where:
X_m = 0.1 for small displacement pile
L_i = Thickness/length of the soil layer (m)
P = Perimeter of the pile (m)
N = Average SPT blow count (statistical mean)

Bearing Capacity Based on Laboratory Test Result

To determine the bearing capacity based on laboratory parameters, several factors need to be considered (Meyerhof, 1963, as cited in Hardiyatmo, 2010), as follows:

1. Overburden Pressure at the Foundation Base

$$P_o = D_f \gamma$$

Where:
P_o = Overburden pressure
D_f = Foundation depth
γ = Unit weight of the soil

2. Foundation Shape Factor

The value of s_c for any φ is:

$$s_c = 1 + 0.2 (B/L) tg^2 (45 + \phi/2)$$

The value of $s_q = s_\gamma$ for $\varphi \geq 10^o$ is:

$$s_q = s_\gamma = 1 + 0.1 (B/L)) tg^2 (45 + \phi/2)$$

The value of $s_q = s_\gamma$ for $\varphi = 0^o$ is 1

Where:
B = Diameter of the foundation (m)
L = Length of the foundation base (m)
φ = Internal friction angle
B/L = 1 (if the foundation is a pile)

3. Foundation Depth Factor

The value of d_c for any depth is:

$$d_c = 1 + 0.4 (D/B)$$

The value of $d_q = d_\gamma$ for any depth is:

$$d_q = 1 + 2 (D/B) \tan \phi (1-\sin \phi)^2$$

The value of d_γ for $\varphi = 0^o$ is 1.

Where:
D = Depth of the foundation (m)
B = Diameter of the foundation (m)

If D/B is greater than 1, then D/B should be replaced with arc-tan (D/B)

4. Load Inclination Factor

The value of $i_c = i_q$ for any φ is:

$$i_c = i_q = [1-(\delta^o/90^o)]^2$$

The value of i_γ for $\varphi \geq 10^o$ is:

$$i_\gamma = [1-(\delta^o/\phi)]^2$$

The value of i_γ for $\varphi = 0^o$ is 1

Where:
δ = Load inclination angle relative to the vertical axis.

By considering the shape of the foundation, the load inclination, and the shear strength of the soil beneath the foundation base, Meyerhof provided the following bearing capacity equation (Hardiyatmo, 2010):

$$Q_u = s_c d_c i_c cN_c + s_q d_q i_q P_o N_q + s_\gamma d_\gamma i_\gamma 0.5 B'\gamma N_\gamma$$

Where:
Q_u = Ultimate bearing capacity
N_c, N_q, N_γ = Bearing capacity factors for strip foundation
s_c, s_q, s_γ = Foundation shape factors
d_c, d_q, d_γ = Foundation depth factors
i_c, i_q, i_γ = Load inclination factors
B' = Effective foundation width
P_o = Overburden pressure at the foundation base
D_f = Foundation depth
γ = Unit weight of the soil

Settlement Analysis

Settlement was evaluated using two approaches: (1) calculations based on field-test-derived allowable bearing capacity, and (2) calculations based on laboratory-derived soil parameters. For allowable bearing capacity, Prakash et al. (1990, as cited in Budiono and Rahardjo, 2008) proposed:

$$S_t = (B/100) + ((Q_a L)/(A_p E_p))$$

Where:
S_t = Amount of settlement (m)
B = Pile diameter (m)
Q_a = Allowable bearing capacity (ton)
L = Pile length (m)
A_p = Pile cross-sectional area (m^2)
E_p = Elastic modulus

For the settlement calculation based on laboratory test analysis data, Terzaghi (as cited in Hardiyatmo, 2010) provides the following equation:

$$\sum Sc_{n} = \sum \left(\frac{Cc}{1+e_0}.H.\log\left(\frac{P_0+\Delta P}{P_0}\right)\right)$$

Where:

S_c = Settlement (cm or mm)
C_c = Compression index (from laboratory consolidation tests)
H = Thickness of the compressible soil layer (m)
e_0 = Initial void ratio (from laboratory tests)
P_0 = Initial effective stress (kN/m²)
ΔP = Change in effective stress due to the applied load (kN/m²)

The magnitude of settlement that still meets the allowable bearing capacity criteria is less than 1 inch or 2.54 cm (Meyerhof, 1956, as cited in Hardiyatmo, 2010). Generally, clay soils experience much greater settlement compared to sand layers. Settlement is closely related to the thickness of the soft soil layer; the thicker the soft soil, the higher the settlement that will occur (Jusi et al., 2024).

RESULTS

Water Content

The laboratory water content results are presented in Table 2. The highest water content value at BH3 (88.41%) occurs at a depth of 30.00-35.55 m, while the lowest value (36.85%) is found at a depth of 20.00-20.55 m. The highest water content value at BH4 (94.97%) occurs at a depth of 15.00-15.55 m, while the lowest value (28.37%) is observed at a depth of 20.00-20.55 m. Both highest and lowest values are in clay lithology.

Table 2. Laboratory test results for water content

Depth	BH3	BH4
	w_c	
(m)	(%)	
2.00 - 2.55	62.17	81.21
5.00 - 5.55	85.74	90.69
10.00 - 10.55	80.84	78.27
15.00 - 15.55	67.85	94.97
20.00 - 20.55	36.85	28.73
25.00 - 25.55	42.47	34.37
30.00 - 30.55	88.41	35.93
35.00 - 35.55	65.81	35.75
40.00 - 40.55	65.81	42.46

Unit Weight

The laboratory unit weight results are shown in Table 3. The highest unit weight value at BH3 (1.950 ton/m³) occurs at a depth of 40.00-40.55 m, while the lowest value (1.527 ton/m³) is found at a depth of 2.00-2.55 m. The highest unit weight value at BH4 (1.908 ton/m³) is at a depth of 40.00-40.55 m, while the lowest value (1.513 ton/m³) is at a depth of 10.00-10.55 m.

Table 3. Laboratory test results for unit weight

Depth	BH3	BH4
	γ_{sat}	
(m)	(ton/m^3)	
2.00 - 2.55	1.565	1.518
5.00 - 5.55	1.576	1.519
10.00 - 10.55	1.527	1.513
15.00 - 15.55	1.896	1.835
20.00 - 20.55	1.8	1.862
25.00 - 25.55	1.867	1.713
30.00 - 30.55	1.818	1.815
35.00 - 35.55	1.93	1.895
40.00 - 40.55	1.95	1.908

Specific Gravity

The results of the calculations show that the specific gravity of the soil/sediment at BH3 ranges from 2.13 to 2.83, while the specific gravity of the soil/sediment at BH4 ranges from 2.41 to 2.64 (Table 4).

Table 4. Laboratory test results for specific gravity

Depth	BH3	BH4
	Gs	
(m)	-	
2.00 - 2.55	2.52	2.52
5.00 - 5.55	2.48	2.48
10.00 - 10.55	2.45	2.45
15.00 - 15.55	2.46	2.46
20.00 - 20.55	2.57	2.57
25.00 - 25.55	2.83	2.83
30.00 - 30.55	2.13	2.13
35.00 - 35.55	2.66	2.66
40.00 - 40.55	2.51	2.51

Atterberg Limits

The plastic limit values in the study area vary with depth. At BH3, the range is between 28.87% and 36.46%, while at BH4, the range is between 28.88% and 43.42%. The plasticity index values in the study area also vary with depth. At BH3, the plasticity index ranges from 27.87% to 49.83%, while at BH4, the range is from 37.33% to 64.89%. According to Atterberg's classification, the soil in the study area can be categorized as having high plasticity and cohesive properties.

Based on the Unified Soil Classification System (USCS), it can be observed that most of the soils in the study area are inorganic clays with high plasticity (CH). However, some samples are classified as organic clays with high plasticity (OH).

Table 5. Laboratory test results for Atterberg test and soil classification

Depth	BH3				BH4				BH3	BH4
	Wn	PL	LL	PI	Wn	PL	LL	PI	Classification	
(m)	(%)								-	
2.00 - 2.55	62.17	32.03	59.9	27.87	81.21	43.14	93.17	50.03	CH	CH
5.00 - 5.55	85.74	36.96	75.13	38.17	90.69	31.03	86.89	55.85	CH	CH
10.00 - 10.55	80.84	35.52	76.37	40.85	78.27	32.76	97.64	64.89	CH	SM
15.00 - 15.55	67.85	35.58	64.11	28.53	94.97	43.42	87.39	43.97	CH	SM
20.00 - 20.55	-	-	-	-	28.73	32.08	67.64	35.56	SM	CH
25.00 - 25.55	42.47	36.46	86.29	49.83	34.37	31.81	90.89	59.08	CH	CH
30.00 - 30.55	88.41	32.56	88.95	56.39	35.93	38.12	94.61	56.49	CH	CH
35.00 - 35.55	65.81	28.87	68.88	40.01	35.75	32.15	82.32	50.17	CH	CH
40.00 - 40.55	65.81	30.93	74.88	43.95	42.46	28.88	66.2	37.33	CH	CH

Consolidation Test Results

From the Table 6, the average compression index value at BH3 is 0.382, with an average coefficient of consolidation (Cv) of 0.006 cm²/s. At BH4, the average compression index is 0.321, with an average coefficient of consolidation (Cv) of is 0.007 cm²/s.

Table 6. Laboratory test results for consolidation test

Depth	BH3 Cv	BH4 Φ	BH3 c	BH4 Φ	BH3 Cc	BH4 Cv (cm^2/ s)	BH3 Cc	BH4 Cv (cm^2/ s)
(m)	(kPa)	(°)	(kPa)	(°)				
2.00 - 2.55	2.52	2.52	0.20	7.07	3.24	5.51	0.431	0.008
5.00 - 5.55	2.48	2.48	0.20	3.42	8.83	5.71	0.750	0.006
10.00 - 10.55	2.45	2.45	10.69	6.45	10.59	5.13	0.840	0.004
15.00 - 15.55	2.46	2.46	30.40	6.92	20.69	13.31	0.229	0.005
20.00 - 20.55	2.57	2.57	69.63	20.70	68.75	30.59	0.256	0.007
25.00 - 25.55	2.83	2.83	68.65	19.50	66.59	14.56	0.155	0.005
30.00 - 30.55	2.13	2.13	96.60	0.22	96.11	11.39	0.350	0.003
35.00 - 35.55	2.66	2.66	107.88	22.71	77.28	9.18	0.170	0.008
40.00 - 40.55	2.51	2.51	94.15	18.20	106.90	18.93	0.240	0.007

Bearing Capacity Calculation Based on SPT Values

Depth (D) / (L_b) = 18 meters
Diameter (B) = 0.4 meters
N SPT = 14
Average N SPT (N") = 21.65
Safety Factor (F_s) = 3

Area (A_b) = (π B²) / 4
= ((3.14) (0.4)²) / 4
= 0.1256 m²

Perimeter (P) = π B
= (3.14) (0.4)
= 1.256 m

End Bearing Resistance
$Q_b = A_b ((40) N") (L_b / B) \leq A_b ((380) (N)) = 1033.46$

Skin Friction Resistance
$Q_s = X_m N p L_i = 135.77$

Ultimate Bearing Capacity (Q_u)
$Q_u = Q_b + Q_s = 116.92$ tons

Allowable Bearing Capacity (Q_{all})
$Q_{all} = Q_u / F_s = 38.97$ tons

Bearing Capacity Calculation Based on Soil Physical Properties

Depth (D) = 18 meters
Diameter (B) = 0.4 meters
N SPT = 14 N
Safety Factor = 3

Area (A_b) = (π (B²)) / 4
= ((3.14) (0.4)²) / 4
= 0.1256 m²

Perimeter (P) = π B
= (3.14) (0.4)
= 1.256 m

Soil Properties:
$\gamma = 1.862$ g/cm³ = 18.261 kN/m³
$\phi = 30.592°$
c = 0.701 kg/cm² = 68.747 kN/m²
Nc = 32.67; Nq = 20.63; Nγ = 18.56

Overburden Pressure (P_o) = $D_f \gamma$
= (18) (18.261)
= 328.691 kN/m²

Foundation Shape Factor
sc = 1 + 0.2 (B/L) $\tan^2(45 + \phi/2)$
= 1 + 0.2 (1) $\tan^2(45 + 30.592/2)$
= 1.4

sq = 1 + 0.1 (B/L) $\tan^2(45 + \phi/2)$
= 1 + 0.1 (1) $\tan^2(45 + 30.592/2)$
= 1.637

Foundation Depth Factor
dc = 1 + 0.4 (D/B)
= 1 + 0.4 arc tan(D/B)
= 1 + 0.4 arc tan(18/0.4)
= 1.628

$d_q = d_\gamma = 1 + 2$ (D/B) $\tan(\phi)$ $(1 - \sin(\phi))^2$
= 1 + 2(18/0.4) tan(30.592) $(1 - \sin(30.592))^2$
= 1.91

Load Inclination Factor
$i_c, i_q, i_\gamma = 1$

Ultimate Bearing Capacity (Q_u)
$Q_u = s_c\, d_c\, i_c\, c\, N_c + s_q\, d_q\, i_q\, P_o\, N_q +$
$s_\gamma\, d_\gamma\, i_\gamma\, 0.5\, B'_\gamma\, N_\gamma$
= 7977.88 kN/m² = 797.79 tons

Allowable Bearing Capacity (Q_{all})
$Q_{all} = Q_u / F_s$
= 797.79 / 3
= 265.93 tons

Port Design Calculation
Port Length (L): 285 m
Port Width (B): 161 m
Port Area (A): (285) (161) = 45,885 m²
Pile Diameter: 0.4 m
Pile Length (L_{pile}): 18 m
Pile Area (A_{pile}): 0.1256 m²
Slab Thickness (T): 0.3 m
Concrete Density ($\gamma_{concrete}$): 2.4 ton/m³
Pile Spacing: 5 m
Number of piles (J): (58) (4) = 232 piles
Vertical Load Assumption (V): 1000 ton
Slab Load Calculation:
T L B $\gamma_{concrete}$ = 33,037 ton
Pile Load Calculation:
J A_{pile} L_{pile} $\gamma_{concrete}$ = 979.08 ton
Total Load Calculation:
V_{tot} = 33,037 + 979.08 = 34,016 ton
Load per Unit Area (q):
V_{tot}/ A = 34,016/45,885 = 0.741 ton/m^2

Settlement Calculation

The settlement calculation is performed to determine the amount of settlement if a port is constructed with a pile depth of 18 m and a diameter of 0.4 m. This calculation uses two methods;

1. Based on Field Test Results

The first calculation uses the minimum allowable bearing capacity (Qa) obtained from the field test results. Using this approach, the calculated settlement is 0.61 cm.

2. Based on Laboratory Test Results

The second calculation uses the settlement value derived from the laboratory tests. In this case, the calculated settlement is 1.2445 cm.

These results indicate the estimated settlement for the proposed pile foundation at the site based on the two different testing methods.

The combined data from field and laboratory investigations confirm that the Balongan site exhibits geotechnical conditions typical of soft coastal clay, which is characterized by low strength, high compressibility, and extended consolidation periods. The results emphasize the need for integrated design approaches that combine empirical and laboratory methods to more accurately evaluate foundation behaviour and performance.

DISCUSSIONS

Overall, the subsurface profiles at are predominantly composed of clay lithology. At BH-3, the depth from 0.00 to 16.45 meters consists of grayish-green clay, and from this depth to 50.00 meters, brownish-gray clay is found. Similarly, at BH-4, the depth from 0.00 to 18.45 meters consists of grayish-green clay, and from 18.45 meters to 50.00 meters, brownish-gray clay is encountered. In relation to the regional geology, grayish-green clay is

classified as coastal deposits, while brownish-gray clay is classified as river deposits.

Correlation with the SPT values (Figure3) indicates a clear relationship between BH-3 and BH-4. The depth from 0.00 to 11.00 meters consists of clay with a very soft to soft consistency, with an SPT value interval ranging from 1/30 to 4/30. From 11.00 meters to 18.00 meters, the clay has a medium to very stiff consistency, with SPT values ranging from 5/30 to 30/30. From 18.00 meters to 50.00 meters, the clay becomes hard, with SPT values ranging from 35/30 to 61/30.

From the graphs (Figures 4 and 5), as well as Table 7 and Table 8, it can be observed that the maximum load capacity from the SPT values tends to be lower compared to the maximum load capacity based on physical and mechanical property values. In the latter, a sharp increase can be seen after reaching a depth of 18.00 meters. This can be explained by a significant increase in the internal friction angle and a change in the consistency of the SPT values from stiff to hard.

The substantial difference between the SPT values and the physical—mechanical property values could be attributed to several factors (Mitchell & Soga, 2005; Fernando et al., 2021), including the potential influence of external factors on the soil before analysis or inaccuracies during the laboratory analysis process (Agustian et al., 2024). On the other hand, the SPT values tend to be more accurate since they are directly tested in the field (Allen & Psarris, 2024).

Given this explanation, the allowable bearing capacity through the SPT values is considered more reliable as a reference. In addition, the SPT has proven reliable for sandy soil and well suited for cohesive soils (Truong & Duong, 2020).

The magnitude of soil settlement (Table 9) was calculated from the SPT values and laboratory analysis. The potential settlement of the soil or sediment, based on field testing with the SPT, is 0.61 cm. The planned port dimensions have been calculated, and the total load acting on the port is 0.741 tons/m². The total settlement of the soil layer beneath the foundation base, based on the laboratory test data, is 2.07 cm, with a consolidation time of 90% occurring over 12.91 years (Table 10). This settlement still meets the criteria for the allowable bearing capacity.

The settlement that still meets the allowable bearing capacity criteria is less than 1 inch or 2.54 cm (Meyerhof, 1956; Hardiyatmo, 2010). Therefore, the calculation results above still comply with the allowable bearing capacity criteria, meaning the settlement that will occur is very small.

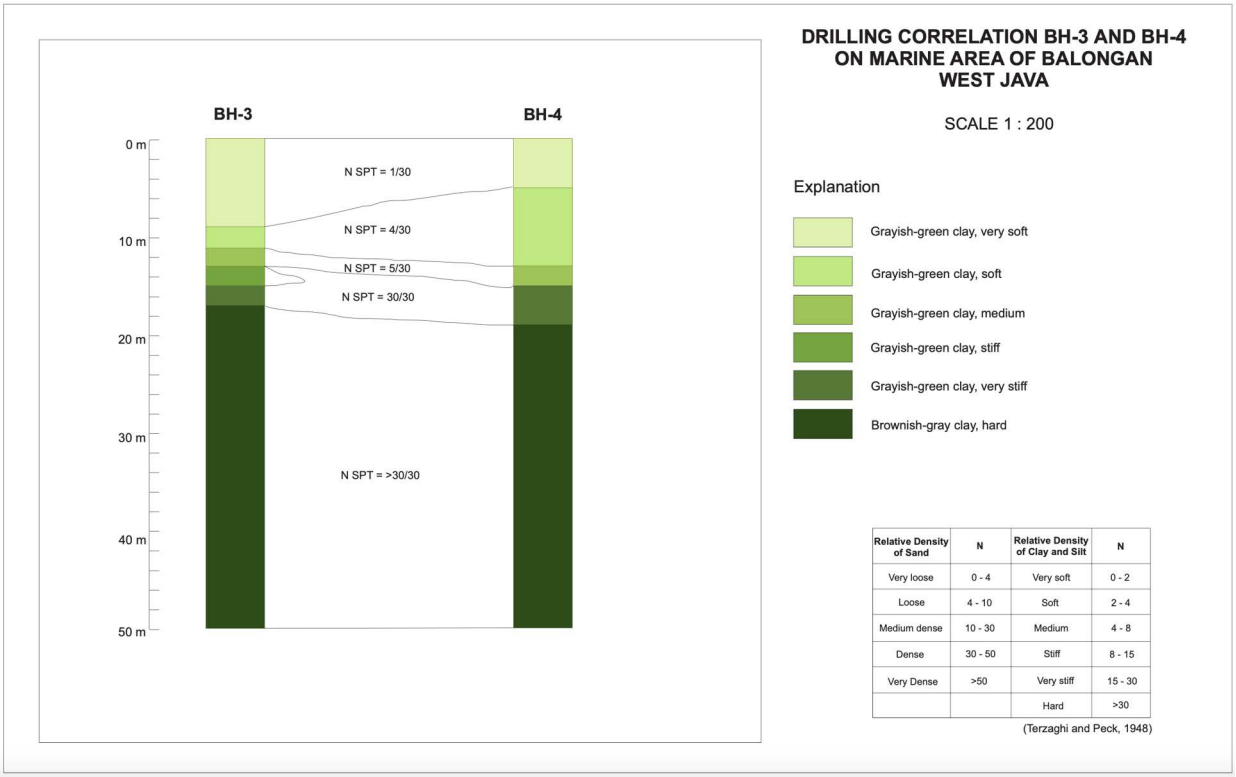

Figure 3. Drilling data correlation for BH-3 and BH-4 (Raharjo P., 2006)

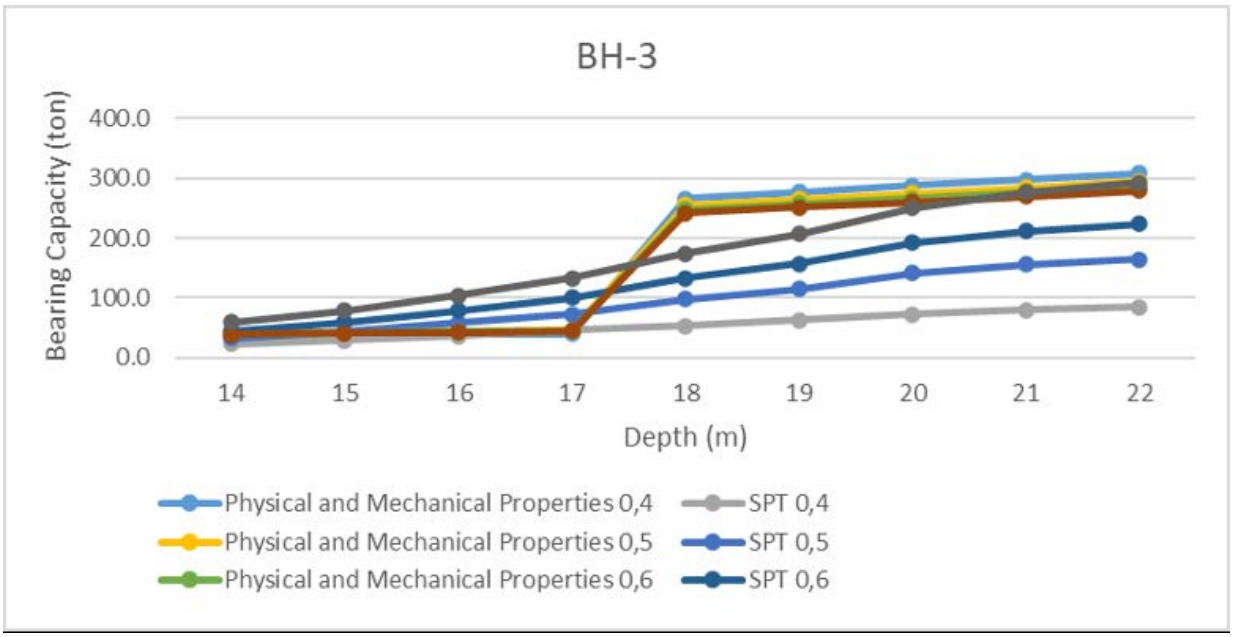

Figure 4. The graph of the allowable bearing capacity (BH3) versus depth

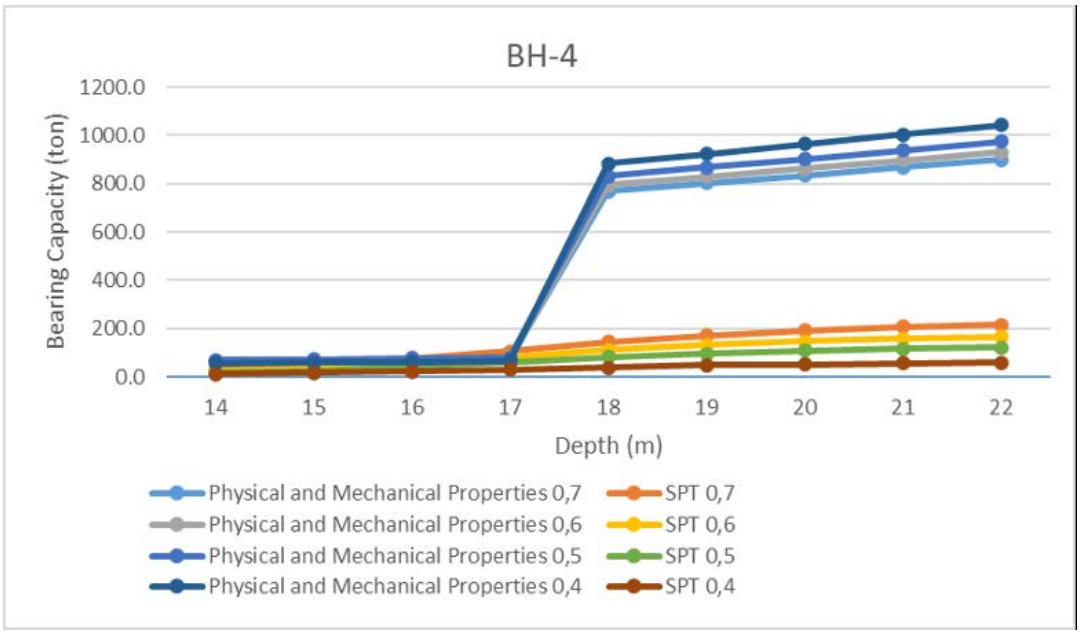

Figure 5. The graph of the allowable bearing capacity (BH4) versus depth

These findings underline the importance of employing a dual approach in geotechnical evaluation, integrating empirical field data with laboratory-derived parameters (Zdravković et al., 2021). Relying solely on either method may lead to underdesign or overdesign. To ensure reliable and efficient foundation performance, designers should consider combining both methods, complemented by probabilistic analysis or safety margins based on site conditions.

In addition, for areas subjected to high structural loads, such as quay walls or cargo terminals, ground improvement techniques may be necessary (Ruggeri et al., 2019). Preloading with vertical drains, vacuum consolidation, or staged construction can accelerate consolidation and reduce settlement-related risks (Indraratna et al., 2012; Zhang et al., 2018). Long-term instrumentation and monitoring are also recommended to validate design assumptions and accommodate post-construction behaviour.

Table 7. Maximum load capacity of BH3

Depth (m)	Maximum Load Capacity (Qall)							
	Diamater 0.4 m		Diamater 0.5 m		Diamater 0.6 m		Diameter 0.7 m	
	Physical & Mechanical Properties (ton)	N SPT (ton)	Physical & Mechanical Properties (ton)	N SPT (ton)	Physical & Mechanical Properties (ton)	N SPT (ton)	Physical & Mechanical Properties (ton)	N SPT (ton)
14.00	35.664	22.989	40.488	33.170	39.688	45.124	39.117	58.852
15.00	37.219	29.591	42.387	43.290	41.529	59.509	40.917	78.248
16.00	38.774	35.869	44.286	57.931	43.371	79.197	42.717	103.690
17.00	40.330	45.589	46.185	73.236	45.212	100.972	44.517	133.071
18.00	265.929	53.068	254.697	98.240	247.256	133.546	241.980	174.071
19.00	276.432	63.372	264.566	115.192	256.701	157.516	251.123	206.269
20.00	286.934	72.150	274.435	141.282	266.147	191.881	260.266	249.927
21.00	297.436	80.311	284.303	155.462	275.593	211.721	269.409	276.369
22.00	307.939	84.382	294.172	164.401	285.038	223.739	278.552	291.895

Table 8. Maximum load capacity of BH4

Depth (m)	Maximum Load Capacity (Qall) (ton)							
	Diamater 0.4 m		Diamater 0.5 m		Diamater 0.6 m		Diameter 0.7 m	
	Physical & Mechanical Properties (ton)	N SPT (ton)	Physical & Mechanical Properties (ton)	N SPT (ton)	Physical & Mechanical Properties (ton)	N SPT (ton)	Physical & Mechanical Properties (ton)	N SPT (ton)
14.00	56.475	11.669	68.105	17.134	66.201	23.616	64.849	31.118
15.00	59.546	16.791	72.001	25.058	69.959	34.951	68.507	46.473
16.00	62.617	22.270	75.896	44.435	73.716	60.164	72.165	78.175
17.00	65.688	30.833	79.792	58.417	77.473	80.060	75.824	105.023
18.00	884.393	38.974	830.292	82.112	794.540	111.452	769.274	145.099
19.00	923.651	47.148	866.485	96.061	828.688	131.163	801.959	171.561
20.00	962.910	51.977	902.679	107.929	862.836	147.120	834.644	192.181
21.00	1002.168	56.385	938.872	116.151	896.984	158.546	867.329	207.328
22.00	1041.426	57.837	975.065	120.909	931.132	164.706	900.013	215.040

Table 9. Calculation of settlement value

Layer	Equilibrium Point	N	M	I	I	L	B	A	A/A1	ΔP (t/m^2)	ΔP (kg/m^2)	Po (t/m^2)	Po (kg/m^2)	Sc (m)	Sc (cm)
1	20	7.13	4.03	0.248	0.992	297	173	51381	0.893	0.657	656.744	37.24	37240	0.0124	1.24
2	24	5.94	3.35	0.247	0.988	305	181	55205	0.831	0.609	608.787	40.67	40666	0.0026	0.26
3	28	5.09	2.88	0.243	0.972	313	189	59157	0.776	0.559	558.916	47.72	47722	0.0018	0.18
4	32	4.45	2.52	0.24	0.96	321	197	63237	0.726	0.516	516.401	54.98	54982	0.0014	0.14
5	36	3.96	2.24	0.237	0.948	329	205	67445	0.680	0.478	478.129	62.40	62402	0.0015	0.15
6	40	3.56	2.01	0.232	0.928	337	213	71781	0.639	0.440	439.770	70.01	70008	0.0010	0.10
	Quantity														2.07

Table 10. Results of settlement duration calculation

%	T	Hdr	$(Hdr)^2$	Cv	t_s	t_m	t_{hour}	t_{day}	t_{year}
10	0.008	2400	5760000	0.012	3840000	64000	1066.67	44.44	
20	0.031	2400	5760000	0.012	14880000	248000	4133.33	172.22	
50	0.197	2400	5760000	0.012	94560000	1576000	26266.67	1094.44	3.00
90	0.848	2400	5760000	0.012	407040000	6784000	113066.67	4711.11	12.91

This study has certain limitations. The number of boreholes was limited to two, and the lateral variability of subsurface conditions across the broader site could not be fully assessed. Furthermore, advanced in-situ testing such as cone penetration testing (CPT), pressuremeter tests, or dilatometer tests was not conducted, which could have provided a more detailed and continuous soil strength profile (Robertson, 2012; Singh et al., 2016). Future investigations should incorporate these methods and increase spatial coverage to reduce uncertainty in geotechnical characterization.

CONCLUSSIONS

This geotechnical study offers valuable insights into the subsurface conditions and foundation behaviour at the proposed Balongan Port site in West Java. The site is predominantly underlain by soft, high-plasticity clay with low shear strength and high compressibility, which presents significant challenges for the design of deep foundations, especially for pile-supported port infrastructure.

Allowable bearing capacities derived from Standard Penetration Test (SPT) data were substantially lower than laboratory-based analyses, confirming the conservative nature of empirical methods and highlighting the need for integrated assessment. Settlement predictions from both SPT and laboratory methods fell within acceptable serviceability limits, but the projected time to reach 90% primary consolidation, approximately 12.9 years, raises concerns regarding long-term performance and the potential need for ground improvement interventions.

The study recommends that future foundation design at the Balongan site incorporate both field and laboratory data, and that designers consider consolidation control strategies such as preloading with vertical drains or vacuum consolidation. Long-term settlement monitoring should also be implemented as part of the construction and operational phase.

Despite limitations in spatial coverage and advanced in-situ testing, this study establishes a technical foundation for further investigation and design refinement. The findings contribute to early-stage decision-making and risk management strategies for developing safe, reliable, and sustainable port infrastructure in soft soil environments.

ACKNOWLEDGEMENTS

The authors would like to express their sincere gratitude to the Marine Geological Institute (MGI) for granting permission to use geotechnical data that served as the foundation of this study. We gratefully acknowledge Najib, Ph.D., and Devina Trisnawati, M.Eng., for their insightful comments which significantly enhanced the analytical depth and clarity of our interpretation.

REFERENCES

Achdan, A., & Sudana, D., 1992. *Peta Geologi Indramayu dan Sekitarnya. Skala 1:100.000.* Pusat Penelitian dan Pengembangan Geologi, 1p.

Agustian, Y., Komarudin, U., & Ardiansyah, N. P. 2024. Sample Disturbance and Its Impact on Soil Properties in Laboratory Soil Mechanics Testing: A Literature Review. *MEDIA KOMUNIKASI TEKNIK SIPIL*, 30(1), 36–46. https://doi.org/10.14710/mkts.v30i1.58043

Allen, K., & Psarris, P., 2024. *Just how accurate are the correlations between SPT N-Value and basic geotechnical strength parameters?*, https://australiangeomechanics.org/papers/just-how-accurate-are-the-correlations-between-spt-n-value-and-basic-geotechnical-strength-parameters/, accessed at 2025-04-06.

Bo, M., Arulrajah, A., Sukmak, P., & Horpibulsuk, S., 2015. Mineralogy and geotechnical properties of Singapore marine clay at Changi. *Soils and Foundations*, 55, pp. 600-

613. https://doi.org/10.1016/J.SANDF.2015.04.011.

Bowles, J., 1993. *Analisis dan Desain Pondasi Jilid 2.* Penerbit Erlangga, 474p.

Budiono, K., & Rahardjo, P., 2008. Studi Penurunan Sedimen Kuarter di Cirebon, Propinsi Jawa Barat. *Jurnal Geologi Kelautan, vol. 6 no. 1*, 53-68.

Fernando, H., Nugroho, S. A., Suryanita, R., & Kikumoto, M., 2021. Prediction of SPT value based on CPT data and soil properties using ANN with and without normalization. *International Journal of Artificial Intelligence Research*, 5(2). https://doi.org/10.29099/ijair.v5i2.208

Hardiyatmo, H., 2002. *Mekanika Tanah I.* Gajah Mada University Press, 490p.

Hardiyatmo, H., 2010. *Analisis Perancangan Pondasi Bagian 1.* Gajah Mada University Press 591p.

Ilahude, D, & Usman, E., 2009. Pendekatan Secara Empirik Terhadap Gejala Perubahan Garis Pantai Daerah Indramayu Dan Sekitarnya. *Jurnal Geologi Kelautan, vol. 7 no. 2* 99-110.

Indraratna, B., Rujikiatkamjorn, C., Balasubramaniam, A. S., & McIntosh, G., 2012. Soft ground improvement via vertical drains and vacuum assisted preloading. *Geotextiles and Geomembranes*, 30, 16–23. https://doi.org/10.1016/j.geotexmem.2011.01.004

Jusi, U., Pratikso, & Maizir, H., 2024. Numerical Model Analysis Of Subgrade Settlement With Foam Mortar Reinforcement Based On Thickness Variation. *Journal of Applied Engineering Science*, 22(4), 810–818. https://doi.org/10.5937/JAES0-53365

Meyerhof, G.G., 1976. Bearing Capacity and Settlement of Pile Foundations. *ASCE Journal of Geotechnical Eng. Div. vol 102 No.GT3, pp. 197-228.*

Raharjo P., Rahmat B., Budiono K., Saputra M. D., Hadi S., Rahardiawan R., 2006. *Studi Kelautan dan Penyusunan* Basic Design *dalam Rangka Pengembangan Dermaga LPG/Propylene* PT Pertamina UP VI Balongan. Pusat Pengembangan Geologi Kelautan. Internal Report. Unpublished.

Robertson, P.K., 2012. The James K. Mitchell Lecture: Interpretation of In-Situ Tests—Some Insights. In: Coutinho, R.Q. and Mayne, P.W., Eds., *Geotechnical and Geophysical Site Characterization 4*, Routledge, Abingdon, 3-2.

Ruggeri, P., Fruzzetti, V. M. E., & Scarpelli, G., 2019. Renovation of quay walls to meet more demanding requirements: Italian experiences. *Coastal Engineering*, 147, 25–33. https://doi.org/10.1016/j.coastaleng.2019.01.003

Mitchell, J. K. and Soga, K., 2005. *Fundamentals of Soil behaviour*, vol. 158, no. 1.

Shah, A., 2021. Study of Maliya Marine Clay for a Highway Embankment. Lecture Notes in Civil Engineering. https://doi.org/10.1007/978-981-16-3383-6_39.

Singh, D., Jha, J. N., & Gill, K. S., 2016. Strength Evaluation of Soil Subgrade Using In-situ Tests. *Civil Engineering and Architecture*, 4(6), 201–212. https://doi.org/10.13189/cea.2016.040601

Truong, M. N., & Duong, T., 2020. An assessment on reliability of SPT data in determining the bearing capacity of pile installed into cohesive soil (a case study). *6th International Conference on Geotechnical and Geophysical Site Characterization (ISC2020)*. https://doi.org/10.53243/ISC2020-102

Zdravković, L., Potts, D. M., & Taborda, D. M. G., 2021. Integrating laboratory and field testing into advanced geotechnical design. G*eomechanics for Energy and the Environment*, 27. https://doi.org/10.1016/j.gete.2020.100216

Zhang, Z., Ye, G. B., & Xu, Y., 2018. Comparative analysis on performance of vertical drain improved clay deposit under vacuum or surcharge loading. *Geotextiles and Geomembranes*, 46(2), 146–154. https://doi.org/10.1016/j.geotexmem.2017.11.002

Guide for Authors - Geoscience Publications
Bulletin of the Marine Geology

Writing should be submitted according to the following restrictions:

1. Manuscript should be written in English and be submitted online via journal website http://ejournal.mgi.esdm.go.id. Online Submission will be free. The author must login in order to make submission.
2. Manuscript should contains at least 2.000 words and at least 8 pages of manuscript that including embedded figures and tables, without any appendix, and the file should be in Microsoft Office (.doc/.docx) format. It should be prepared in A4 paper (21cm x 29.7cm) using 2.5 cm for left and right margins and 2 cm for top and bottom margins, additionally the paragraph should be used 1 line spacing, 11 TNR.
3. Title, Abstract, and Keywords should be written in English
   - Abstract should be written in English and Bahasa Indonesia version
   - Title should be less than 15 words, title case, small caps, centered, bold, font type Times New Roman (TNR), font size 16, and single spaced.
   - Abstract contains neither pictures nor tables, justified, in 11 TNR, single spaced, and should not exceed 250 words.
   - Keywords contain four to six words/phrases separated with coma and should be justified, 10 TNR and single spaced.
   - Please provide all email address of all authors for our database concern, however, in the published version, only the email address of the first author will be appeared.
4. Manuscript body consists of: Introduction, Method, Result, Discussion, and Conclusion completed by Acknowledgment and References in capital and bold.
5. Heading should be made in four levels. Level five cannot be accepted.
   - Heading 1: title caps, left aligned, bold, 14 TNR, single spaced
   - Heading 2: title case, left aligned, bold, 11 TNR, single spaced
   - Heading 3: title case, left aligned, italic, 11 TNR, single spaced
   - Heading 4 is not recommended, however, it could still be accepted with the format of: sentence case, left indent 5 mm, hanging indent 5 mm, italic, 11 TNR, single spaced
   - Heading 5 cannot be accepted in the manuscript.
6. Figure and table can be either in black and white or in color, they should be clearly readable and in a proportional measure to the overall page. Caption should be numbered, in 9 TNR and single spaced. For lay outing purpose, please provide the respective captioned figure/table with extension .tif/.jpg/.jpeg within a particular folder apart from the manuscript. Please note the figure source/citation/reference if it is taken and/or modified from previous publication.
7. Mathematical equation should be clearly written, numbered orderly, and accompanied with any information needed.
8. Header and footer including page number must not be used. All hypertext links and section bookmarks will be removed from papers. If you need to refer to an Internet email address or URL in your paper, you must type out the address or URL fully in Regular font.
9. Citation and Reference. Following are the detail organization of the references guidelines:
   a. References are written in alphabetical order according to the family name of the first author.
   b. If there is more than one references made by similar author, References are arranged in order of time, and then in alphabetical order.
   c. All the references should be cited in the text. In the text, reference is cited with author family name and the year of publication. If it is written by 2 authors, the family name of both authors are noted, followed by the year of publication, if it is written by more than 2 authors, the reference is cited with the first author family name, followed by *et al.,* and the year of publication. For example: (Kennett, 1981); (Usman and Panuju, 2013); (Susilohadi *et al.*, 2009). Several references are written in alphabetical order, for example: (Kennett, 1981; Susilohadi *et al.,* 2009; and Usman and Panuju, 2013).
   d. References are consist of paper, proceeding, or book that are published, or unpublished report including internal report, dissertation, or thesis.
   e. References can be taken from website, by writing the hyperlink, and the time when it is accessed. Wikipedia, personal blog, or non scientific website is not allowed to be taken into account.

f. References should be ten references in minimum, at least two of them were published in the last five years.

g. Only the family name of the authors are written, followed by the abbreviation of their first name and middle name (if available). If the reference is written by more than one author, all authors should be written, abbreviation (e.g. dkk, *et al,* or drr) is not allowed..

h. All the information of the references must be noted, including publisher, journal volume, number (if available), and page number.

- For book, the book title should be written in italic, for example:

  Kennett, J.P., 1981. *Marine Geology.* Prentice Hall, 813p.

- For periodicals, the name of the journal should be written in italic, for example:

  Susilohadi, S., Gaedicke, C., and Djajadihardja, Y.S., 2009. Structures and sedimentary deposition in the Sunda Strait, Indonesia, *Tectonophysics,* 467 (1): 55-71.

- (Tectonophysics is the name of the journal, 467 is the volume, 1 is issued number, 55 – 71 is page number)

  Usman, E., and Panuju, 2013. Study of Gas Potency Based on Gravity Anomaly Modeling And Seismic Profile Analysis at Banggai-Sula Basin. *Bulletin of the Marine Geology,* 28 (2): 51-60.

- For edited symposia, special issues, etc. published in periodical:

  Kenneth, S. J., 2009. Marine biogeochemistry in 2025. In: D. Glickson (Editor), *Oceanography in 2025: Proceedings of a workshop.* The National Academic Press, Washington D. C.: 130 – 134.

- For websites:

  <http://palaeo-electronica.org/2003_1/benthic/issue1_03.htm> [Accessed on 30 November 2011].

- Unpublished references:

  Darlan, Y., Kamiludin, U., Kurnio, H., Rahardian, R., Hutagaol, J. P., Sianipar, A. H., and Sinaga, A. C., 2005. *Eksplorasi prospektif gas biogenik kelautan di Perairan Muara Kakap dan sekitarnya - Kalimantan Barat.* Pusat Penelitian dan Pengembangan Geologi Kelautan, Bandung, Badan Penelitian dan Pengembangan Energi dan Sumberdaya Mineral, Departemen Energi dan Sumberdaya Mineral. Internal report, 104p. Unpublished.

SERTIFIKAT

Direktorat Jenderal Penguatan Riset dan Pengembangan,
Kementerian Riset, Teknologi, dan Pendidikan Tinggi

RISTEKDIKTI

Kutipan dari Keputusan Direktur Jenderal Penguatan Riset dan Pengembangan,
Kementerian Riset, Teknologi, dan Pendidikan Tinggi Republik Indonesia
Nomor: 21/E/KPT/2018, Tanggal 9 Juli 2018
Tentang Hasil Akreditasi Jurnal Ilmiah Periode I Tahun 2018

Nama Jurnal Imiah

Bulletin of the Marine Geology

E-ISSN: 2527-8843
Penerbit: Puslitbang Geologi Kelautan, Kementerian ESDM

Ditetapkan sebagai Jurnal Ilmiah

TERAKREDITASI PERINGKAT 2

TERAKREDITASI

Akreditasi berlaku selama 5 (lima) tahun, yaitu
Volume 31 Nomor 1 Tahun 2016 sampai Volume 35 Nomor 2 Tahun 2020

Jakarta, 9 Juli 2018
Direktur Jenderal Penguatan Riset dan Pengembangan

Dr. Muhammad Dimyati
NIP. 195912171984021001

MARINE GEOLOGICAL INSTITUTE

GEOLOGICAL AGENCY
MINISTRY OF ENERGY AND MINERAL RESOURCES
Jalan Dr, Junjunan No. 236, Bandung-40174, Indonesia
http://www.mgi.esdm.go.id, E-mail: ejournal.p3gl@gmail.com

ISSN 1410 - 6175
9 771410 617003